Aqueous Stability and Transport of Catalytic Nanoparticles for Groundwater Remediation

by

Adam Lentz

A thesis
presented to the University of Waterloo
in fulfillment of the
thesis requirement for the degree of
Master of Science
in
Earth Sciences

Waterloo, Ontario, Canada, 2015

AUTHOR'S DECLARATION

This thesis consists of material all of which I authored or co-authored: see Statement of Contributions included in the thesis. This is a true copy of the thesis, including any required final revisions, as accepted by my examiners.

I understand that my thesis may be made electronically available to the public.

Statement of Contributions

Chapters 2 and 3 of this thesis will be submitted as journal articles. These articles are co-authored by myself, my co-supervisors, and Dr. Frank Gu and Tim Leshuk. The majority of the contributions (data collection, figure preparation, and writing) were completed by myself. Tim Leshuk synthesized the nanoparticles, wrote paragraphs describing nanoparticle synthesis, and collected nanoparticle characterization data. Other co-authors contributed with edits and made suggestions to improve the chapters. Chapter 4 is under preparation to be submitted as a journal article co-authored by those listed above and additionally Mark Rivers. Mark contributed with additions to the tomography methodology and image processing and made suggestions relating to image analysis.

Abstract

Nanoparticles (NP) are increasingly being used for *in situ* groundwater remediation because of their catalytic properties and the potential to inject them directly into the subsurface. Here, the aqueous stability and transport in porous media were evaluated for two types of NP: 1) catalytic and magnetically separable controlled superparamagnetic iron oxide NP aggregates (CSA) in 100, 240, and 340 nm diameter sizes and 2) palladium NP (Pd-NP) 5-50 nm in diameter. The Pd increases reaction rates, and the polymeric coatings (polyacrylamide on CSA and polyvinylpyrrolidone on Pd-NP) improve colloidal stability and transport. Investigations, under environmentally relevant conditions, into the longevity of Pd on the surface of CSA found that $<$ 5 % of the Pd was released from the CSA over 4 months. Thus, sufficient Pd remained on the CSA surface to maintain catalysis during field-scale applications. To evaluate the aggregation and settling of NP, suspension tests were conducted in environmentally relevant NaCl, $MgSO_4$, and $CaCO_3$ solutions. The addition of Pd onto the surface of CSA did not lead to detectably altered NP stability. Increased settling of CSA was observed with increases in CSA size, ionic strength (IS), and ion charge. The lowest stability was observed for the 340 nm diameter CSA NP, with greater stability observed for the 240 nm, and the greatest for the 100 nm size. The greatest aggregation was observed for solutions containing $CaCO_3$ (complete settling within 3 hr), followed by $MgSO_4$; minimal aggregation was observed for the NaCl solutions and ultrapure water suspensions (minimal settling over 1-4 days, dependent on NP size). Decreased stability of larger NP (340 nm vs. 100 nm) suggests different mechanisms of settling and stability, relative to 10-100 nm NP reported elsewhere in the literature. The Pd-NP remained suspended for over a week in all solutions tested. The small size and the non-magnetic nature of the Pd-NP, rather than their surface charge, may have affected the stability relative to the 100-340 nm CSA. Column transport studies evaluated the mobility of NP in Ottawa silica sand porous media with a 0.7 mm mean diameter. The breakthrough test protocol was 5 pore volumes (PV) of NP suspension followed by 5 PV of elution with ultrapure water. The protocol for experiments with low mobility NP included input of a total of 20 PV: 5 PV of NP suspension, 5 PV of elution with the same solution, 5 PV of ultrapure water at the same

flow rate, and 5 PV of ultrapure water input at a higher flow rate. Inverse modeling with the CXTFIT option of the STANMOD 1-D transport model was used to determine retardation of the NP and the % NP input concentration that eluted. There were strong linear correlations between fitted NP input concentration and the calculated % of NP eluted. Model results indicated conservative transport with ≈100 % elution, no retardation, and an attachment efficiency (α) = 0.0 for all NP transport experiments in ultrapure water. Minimal mobility (< 5 % elution, attachment efficiency $\alpha > 2.4$) of CSA was observed after 20 cumulative pore volumes in 1.3 and 5.1 mM ionic strength (IS) $CaCO_3$ solutions, except for the case of 100 nm CSA at 1.3 mM IS $CaCO_3$ (85 % elution, $\alpha = 0.03$). The Pd-NP were fully mobile in 1.3 mM IS $CaCO_3$ solution. Calculated attachment efficiencies were above the theoretical threshold of 1, indicating that non-colloidal filtration theory attachment mechanisms, such as ripening, aggregation, or straining, controlled NP transport. Modest detachment was observed following both replacement of the $CaCO_3$ input solution with ultrapure water and after increasing the flow rate. With a column test in 8.6 mM IS $CaCl_2$ solution, minimal elution of NP was observed following 10 PV; however, complete detachment occurred when ultrapure water was flushed through the column. Reversible attachment of NP was observed in $CaCl_2$ solutions, whereas irreversible attachment was observed in $CaCO_3$ solutions. Synchrotron-based microtomography, a non-destructive imaging technique, which provides 3-D images of NP distribution on the pore-scale, both spatially and temporally, was used to evaluate Pd-NP transport. Tomography was used to collect images both above and below the Pd absorption-edge. Images collected below the absorption edge were subtracted from above-edge images to obtain absorption-difference images. Segmented and difference images were then multiplied together. These processes allowed for the determination of profiles of porosity, aqueous phase greyscale value, and silica phase greyscale value for each slice. Profiles of porosity enabled images to be lined up based on characteristic patterns for each column. With little variation in silica greyscale values from one image to another, aqueous phase attenuation values increased in the presence of the Pd-NP and decreased after the NP were flushed. The resolution was insufficient to image individual NP, but did allow for quantification of Pd-NP in a non-ideal silica-grain porous media. This study indicated that CSA and Pd-NP transport

depends on the aqueous environment and NP size and stability. Pd NP could be viably transported through a $CaCO_3$-rich aquifer to catalyze remediation reactions. The CSA could potentially be transported in $CaCO_3$-free solutions in non-carbonate aquifers during *in situ* remediation applications. This study further validated the usefulness of tomography for transport studies of Pd-NP in silica grains.

Acknowledgements

I want to thank my co-supervisors, Dr. David Blowes and Dr. Carol Ptacek, for their guidance and education over my degree. They have taught me a lot and I appreciate their support and dedication, and, at times, patience. Thank you to my committee members, Frank Gu and Dave Rudolph, for your time and meaningful contributions.

Funding for my research was provided by the Ontario Ministry of Research and Innovation Ontario Research Fund-Research Excellence Grant awarded to D. Blowes and C. Ptacek, Natural Sciences and Engineering Research Council (NSERC) Discovery Grant and Canada Research Chair grant awarded to D. Blowes. Funding for myself came from an NSERC Alexander Graham Bell Canada Graduate Scholarship and an Ontario Graduate Scholarship, which made my life during my Master's less stressful. Parts of this research used resources of the Advanced Photon Source, a U.S. Department of Energy (DOE) Office of Science User Facility operated for the DOE Office of Science by Argonne National Laboratory under Contract No. DE-AC02-06CH11357.

The people of GRIME have provided a lot of help and friendship. Thanks to Joy Hu for sample analysis, and Laura Groza and Jeff Bain for answering an endless number of questions. Thanks to those who helped with my experiments: Jane Eagling, Emily Saurette, Ying Ying Liu, and Harish Veeramani for tomography; Priyanca Patel, Katherine Raymond, Kristen Wesenberg, and Adrienne Trac for column experiments. And many others who were friends along the way. I would like to thank Julia Jamieson-Hanes for help along the entire way. We shared a lot of experiences that really taught me as an academic and researcher.

Thank you to Jenna Pilon and my family: the support and experiences have meant a lot. And to the Waterloo Warriors: most enjoyable baseball of my career.

Dedication

To those who deserve it most, thank you for supporting me and being there for me:

Mom and Dad Jenna Pilon

Table of Contents

List of Figures

List of Tables

List of Abbreviations and Symbols

Abbreviation	Definition
‘	Duplicate batch
@	Coated with
1-D	One-dimensional
13-BM-D	Sector 13 bending magnet beamline end station
3-D	Three-dimensional
A	Absorbance
Ag-NP	Silver nanoparticles
AO	Aesthetic objective
APS	Advanced photon source, Argonne National Laboratory, IL USA
α	Attachment efficiency
C-ST	Continuous suspension test
C/C_0	Relative concentration
C1	Column 1 for tomography
C2	Column 2 for tomography
CCC	Critical coagulation concentration
CFT	Colloidal filtration theory
CMC	Carboxymethyl cellulose
CNT	Carbon nanotube
CSA	Controlled SPION aggregate
DLS	Dynamic light scattering
DLVO	Derjaguin-Landau-Verwey-Overbeek
E-ST	Episodic suspension test
GSV	Greyscale value
IS	Ionic strength
I1	Image one of five-image tomography column C2
I2	Image two of five-image tomography column C2
I3	Image three of five-image tomography column C2
I4	Image four of five-image tomography column C2
I5	Image five of five-image tomography column C2
IC	Ion chromatography
ICP-OES	Inductively coupled plasma optical emission spectrometer
K-edge	K-shell electron absorption edge

Abbreviation	Definition
L	Length
M	Mass
MSD	Multimodal size distribution
NP	Nanoparticle
nZVI	Nano zero-valent iron
PAA	Polyacrylic acid
PAM	Polyacrylamide
Pd-NP	Palladium nanoparticles
PV	Pore volume
PVP	Polyvinylpyrrolidone
R	Retardation
R^2	Correlation coefficient
SEM	Scanning electron microscope
SMT	Synchrotron-based microtomography
SPION	Superparamagnetic iron oxide nanoparticle
T	Time
TCE	Trichloroethylene
TEM	Transmission electron microscope
ZPC	Zero point charge
ZVI	Zero-valent iron

Chapter 1
Introduction

1.1 Background and Objectives

This investigation focuses on nanoparticle (NP) use for groundwater remediation. Specifically, the suspension and transport properties of superparamagnetic iron oxide nanoparticles (SPION), as controlled SPION aggregates (CSA), and palladium NP (Pd-NP) were investigated. Superparamagnetic is a behavior seen in Fe-based NP where the particles have no magnetism outside of a magnetic field but are attracted to a magnet when magnetic forces are present. These NP are potential remediation materials, as the NP can be vectors for catalysts, and the CSA are potentially recoverable because of their superparamagnetic quality.

Nanoparticles are increasingly being used as a reactant or as a reaction catalyst for groundwater remediation (Matlochová et al., 2013). Currently, primarily nano zero-valent iron (nZVI) and carbon nanotubes (CNT) are being used as remediation tools (Tratnyek and Johnson, 2006; Tang and Lo, 2013). Common contaminants remediated are metal solutes, such as hexavalent chromium (Ponder et al., 2000), and organic molecules, such as trichloroethylene (Wang and Zhang, 1997). Field observations of nZVI transport up to 3 m (He et al., 2010; Kocur et al., 2014; Wei et al., 2011) and up to 1 m (Johnson et al., 2013) from the injection zone have been reported. Concentrations of smaller nZVI (100 nm *versus* 475 nm) have been observed to decrease 7 times of the original NP concentration at the injection well (Wei et al., 2010), indicating greater mobility. High rates of degradation of trichloroethene (Quinn et al., 2005) and vinyl chloride (Wei et al., 2011) by nZVI were observed in laboratory batch studies using nZVI. However, the reactivity was not sustained over longer periods of time (He et al., 2010; Johnson et al., 2013) NP *in situ* applications include the injection of NP into the subsurface to be immobile and form an *in situ* reactive barrier (Tratnyek and Johnson, 2006; Matlochová et al., 2013). Another application may be for the injected NP to remain mobile and to transport through a zone of contamination and be removed (Tratnyek and Johnson, 2006). Field challenges to overcome include characterization of

NP mobility, which is greatly affected by site-specific flow velocities, pore structure, and aqueous NP stability and aggregation, and reaction pathways (O'Carroll et al., 2013b).

Beyond groundwater remediation, understanding NP behavior in subsurface environments is important due to vast worldwide industrial NP production. Approximately 10,000 t of NP are produced worldwide annually (Piccinno et al., 2012), mainly TiO_2, SiO_2, ZnO, and carbon nanotubes, and are mostly for use in consumer products (Benn et al., 2010). With such a large quantity in global distribution, NP are bound to end up in the environment, where their environmental fate becomes important.

As the study of nanomaterials is fairly new, toxicity of NP, especially long-term effects, is not fully understood. Yet, toxicity is important to consider, especially from a human drinking water perspective. At NP concentrations well below those used in remediation, nZVI (Grieger et al., 2010) and carbon nanomaterials (Oberdorster, 2004) have been found to be toxic. Polyacrylamide, a coating commonly used on NP, has been shown to depolymerize to neurotoxin acrylamide (Woodrow et al., 2008). In applications where potentially toxic NP are used for remediation purposes, NP properties and mobility must be well defined, and containment of NP may be required to prevent release to the environment.

After release to the environment, due to their high surface-to-mass ratio, NP can be contaminants themselves (Klaine et al., 2008; Lin et al., 2010) or vectors for contaminants by enhancing transport *via* a three-phase system. The three-phase system consists of a mobile aqueous phase, an immobile solid phase (aquifer material), and a mobile solid phase (colloid and NP) (Ryan and Elimelch, 1996; McGechan and Lewis, 2002). The NP solid phase mobility is affected by the stability of NP.

NP stability (used here as the ability for NP to stay suspended) and mobility, and consequently settling and immobility, are affected by NP size, surface coating, surface charge, solution chemistry, and porous media properties (Hotze et al., 2010). Laboratory experiments conducted to determine NP stability and mobility properties are completed following multiple approaches. Suspension tests monitor the time needed for settling to occur, an indicator of instability, as a function of aqueous environments (Sakulchaicharoen et al., 2010). Column tests assess mobility in porous media (He et al., 2009a; Petosa et al., 2010). Further characterization of transport studies conducted at a

finer scale, the pore-scale, can utilize emerging analytical tools, such as synchrotron-based microtomography (Wildenschild et al., 2005).

To describe the removal of particles from suspended liquids during transport in porous media, colloidal filtration theory (CFT) is often used (Yao et al., 1971; Tufenkji and Elimelech, 2004). Filtration mechanisms included in CFT are interception (electrostatic attraction between particles and grains in close proximity), sedimentation (due to gravitational forces), and diffusion (Brownian motion-based random movements). Other mechanisms of removal not included in CFT are straining and wedging (the removal of NP from solution by NP exceeding pore sizes), blocking (the prevention of further attachment of NP following initial attachment due to particle-particle repulsions), and ripening (the increase of attachment of colloids to surface grains due to particle-particle attraction following initial attachment, the opposite of blocking). Straining has a greater effect as NP size increases and pore size (collector size) decreases. Bradford et al. (2002) concluded that straining is important when the NP diameter is greater than 0.17 % of the mean collector diameter and Sakthivadivel (1969) claims straining to be a significant mechanism when the NP diameter is 5 % of the collector diameter. Magnetic forces and aggregation are also not considered in CFT.

Another approach to describe colloidal stability is the Derjaguin-Landau-Verwey-Overbeek (DLVO) theory, using potential energies to summarize the attractive van der Waals and repulsive double layer forces between collector grains and colloids. Other forces included are hydraulic and steric repulsive forces (non-DLVO) (Ryan and Elimelech, 1996). The double layer potential energy is influenced by solution ionic strength (IS), colloidal size, and particle and collector surface charges (Ryan and Elimelech, 1996). High IS and higher charged ions compress the double layer leading to stronger attractive forces and particle adhesion (Hemansson, 1999). Removal of particles from suspension into the primary potential energy minimum (deep) results in irreversible attachment, while the secondary potential energy minimum (shallower) results in reversible attachment. The secondary minimum is shallower for smaller particles and can be removed by decreasing IS resulting in expansion of the double layer and increased stability (Ryan and Elimelech, 1996). The characteristics of the primary and secondary minimum can help interpret mechanisms of attachment and filtration.

In this study, iron-based CSA and Pd-NP are evaluated for their potential application in *in situ* groundwater remediation. SPION have been studied for their potential use in medical applications (Chan and Gu, 2013; Gupta and Gupta, 2005; Yoffee et al., 2013) and as sorbents in waste-water treatment (Horák et al., 2007; Singh et al., 2011); however, their use for groundwater remediation has not been evaluated previously. Pd-NP have been proposed for use as catalysts for *ex situ* groundwater remediation (Chaplin et al., 2012) and water treatment (Omole et al., 2007).

The objectives of this investigation were to: 1) assess the aqueous stability and transport of iron-based CSA, with and without catalytic Pd-coatings, for potential use in *in situ* groundwater remediation applications, 2) characterize the effect of CSA size on aqueous stability and transport in porous media, and 3) assess the usefulness of using synchrotron-based microtomography to quantify catalytic Pd-NP transport experiments in natural silica-grain porous media.

To accomplish these objectives, laboratory experiments were conducted to assess the aqueous stability and mobility in porous media of CSA and Pd-NP. Suspension tests, monitored with a series of photographs or continuous absorbance readings of NP, were used to evaluate aqueous stability. Common groundwater chemistries were used to examine the effects of ions on NP stability and aggregation. Transport in porous media was investigated by conducting breakthrough experiments of the NP in a saturated column. A quantitative approach was used to assess mobility, as well as one-dimensional transport simulations. Using a synchrotron facility, microtomography was completed for palladium NP in small-scale columns. This method characterizes NP transport within porous media and enables spatial and temporal 3-D imaging of the NP distribution on the pore scale.

1.2 Thesis Structure

This thesis is structured as follows: Chapter 1 gives an introduction to the subject and overview of the thesis; Chapters 2 to 4 were written as stand-alone journal articles; and Chapter 5 provides a conclusion for the entire thesis and gives recommendations on

future research. Chapter 2 is the assessment of iron-based nanoparticles and examines the stability and mobility of CSA, with and without the catalytic capability, in various environmentally relevant conditions from multiple experimental setups. Chapter 3 follows the structure as Chapter 2 but explores the effect of NP size on the aqueous stability and mobility. Chapter 4 examines the transport of Pd-NP primarily through synchrotron-based microtomography, a non-destructive 3-D imaging technique. Because Chapters 2 to 4 were written as stand-alone journal articles, there is some unavoidable redundancy in information amongst the chapters.

Chapter 2
Aqueous Stability and Transport in Porous Media of Catalytic Superparamagnetic Iron Oxide Nanoparticles

To be submitted as journal publication by: Adam M. Lentz, Timothy Leshuk, David W. Blowes, Frank X. Gu, Carol J. Ptacek

2.1 Summary

Nanoparticles (NP) are increasingly being used for *in situ* remediation of groundwater. This study evaluated the transport of catalytic and magnetically separable superparamagnetic iron oxide NP, designed with Pd catalyst to increase hydrogenation reaction rates in subsurface environments and coated with polyacrylamide to improve transport and provide efficient collection following use. Suspension tests were used to evaluate the aggregation and settling of these NP, with and without the Pd catalyst, in ultrapure water and in monovalent and divalent salt solutions of varying solute concentrations. In the suspension tests, the most aggregation occurred in $CaCO_3$ solutions, followed by $MgSO_4$, with minimal aggregation observed for the NaCl solutions and ultrapure suspensions. Complete settling within 3 hr was observed at ionic strengths above 2 mM for $CaCO_3$, above 5 mM for $MgSO_4$, and above 50 mM for NaCl solutions. Reducing the thickness of the double layer and subsequent particle aggegration led to more rapid settling. Column transport studies were conducted using 15 cm long columns packed with silica sand (mean diameter 0.7 mm) to evaluate the mobility of the NP in porous media of different aqueous matrices. The results of the transport studies showed that the NP exhibited conservative transport in ultrapure water with similar breakthrough curves to Cl- and attachment efficiencies of 0.00. Simulation results suggest minimal retardation and a good fit between fitted NP input concentrations and calculated NP % elution. In solutions at 50 % and 10 % $CaCO_3$ saturations (5.1 and 1.3 mM ionic strength) minimal elution of NP was observed after 25 pore volumes of cumulative flow,

with attachment efficiency values over 3. Virtually no detachment (< 1%) of the NP was achieved by replacing the $CaCO_3$ input solution with ultrapure water and increasing the flow rate. In an experiment with an 8.6 mM ionic strength $CaCl_2$ input solution, minimal elution of NP was observed after 5 pore volumes of NP-input followed by 5 pore volumes of NP-free input, but after the $CaCl_2$ solution was replaced by ultrapure water complete detachment was observed. These results suggest that transport and recovery of the NP are viable in carbonate-free aquifers, but modification to the properties of the NP will be required for applications in $CaCO_3$ containing aquifers to achieve collection after injection.

2.2 Introduction

Groundwater containing contaminants such as Cr(VI), trichloroethylene (TCE), or nitrate, derived from industry, agriculture and mining often requires remediation to protect water resources. Conventional remediation methods, including pump-and-treat and natural attenuation, and passive in situ techniques, such as permeable reactive barriers with zero-valent iron (ZVI), have been used to treat groundwater contamination (Blowes et al., 2000).

The use of NP for groundwater remediation has been proposed (EPA, 2008; Grieger et al., 2010; Tang and Lo, 2013). The reactivity of NP is enhanced due to the high surface-to-mass ratio and injection of NP into the subsurface requires minimal land disturbance. Nanoparticles, such as single- and multi-walled carbon nanotubes (Matlochova et al., 2013), nano-ZVI (nZVI) (Tratnyek and Johnson, 2006), and TiO2 (Yao, 2014), have been shown to catalyze degradation or promote changes in oxidation states of organic and inorganic contaminants. Studies on nZVI used for remediation of organic and inorganic contaminants in groundwater include reports on reactivity (Mystrioti et al., 2014), column tests (Busch et al., 2014; He et al., 2009a), and field injections (Johnson et al., 2013; Bennett et al., 2010; Quinn et al., 2005), and commonly employ synthesis methods summarized by He and Zhao (2005).

Additional studies on NP transport in a wide range of porous media under different geochemical conditions are required to thoroughly understand the mechanisms limiting transport at laboratory and field scales. Although NP are smaller than typical pore dimensions, transport of bare nZVI and other Fe-based NP is often limited due to the magnetic attraction and van der Waals forces between particles and other particles and aquifer solids (Phenrat and Lowry, 2009) and the agglomeration of particles in solution (Raychoudhury et al., 2014; Sakulchaicharoen et al., 2010).

Laboratory studies have been conducted to provide information on the environmental fate and transport of NP in porous media. Studies on the mobility of nZVI (He et al., 2009a; Saleh et al., 2007), quantum dots (Quevedo and Tufenkji, 2009), single- and multi- walled carbon nanotubes (O'Carroll et al., 2013b; Wang et al., 2008a), TiO_2 (Choy et al., 2008; Fang et al., 2009), CeO_2 (Li, et al., 2011), Ag (Mitzel and Tufenkji,

2014; Sagee et al., 2012), and ZnO_2 (Jiang et al., 2013; Jones and Su, 2014) have been conducted using column tests. NP stability and properties depend on the porous media type, as in the case where Laumann et al. (2013) observed less transport in carbonate sand compared to quartz sand. Porous media grain size affects transport as more NP straining occurs in fine sands relative to coarse sands (Raychoudhury et al., 2014). The aqueous environment has a major effect, including the inverse relationship between stability and ion charge (Ryan and Elimelech, 1996) and ionic strength (IS) (Lin et al., 2010). Critical coagulation concentrations (CCC) are often cited (Chen and Elimelech, 2006) where at and above a threshold solute concentration of a particular ion, aggregation and settling occurs. Above the CCC, the rate of settling is constant. Along with breakthrough curves, NP mobility is quantifiable with attachment efficiency (α) determined using colloid filtration theory, CFT (Tufenkji and Elimelech, 2004). The α value defines the fraction (0-1) of collision of colloids and porous media that cause attachment and represents the affinity of colloids to attach to porous media. When $\alpha = 1$, the CCC is reached. Attachment mechanisms in CFT include interception, sedimentation, and diffusion. Non-CFT attachment mechanisms include ripening and straining. Straining becomes important when the NP diameter is > 0.17 % of the mean collector diameter (Bradford et al., 2002) or significant when the NP diameter is > 5 % of the collector diameter (Sakthivadivel, 1969).

In addition to column assessments, field injection studies have been conducted with nZVI coated with carboxymethyl cellulose (CMC) (Bennett et al., 2010), emulsified-ZVI (Quinn et al., 2005), or other materials (Kocur et al., 2015). NP concentrations over 1 g L-1 are needed to provide sufficient reactivity for groundwater remediation applications (Bennett et al., 2010; Quinn et al., 2005; Kocur et al., 2014). In these injections, significant NP material is often lost within a few meters of injection wells.

Nanoparticles, such as nZVI, can be used to carry catalysts by coating them with a noble metal, such as palladium (He and Zhao, 2005; Linley et al., 2014). Reactivity of nZVI and other NP increase with catalysts, decreasing the activation energy and, thus, increasing reaction rates for hydrogenation reactions. The addition of Pd on the surface of NP, such as nZVI (Pd doped nZVI, or, nZVI@Pd) promotes increased reaction rates,

such as observed for the rate of TCE hydrodechlorination (Lien and Zhang, 2007). Pd can be added to the surface of NP with a precipitation step during synthesis (Liu et al., 2014; Traynyek and Johnson, 2006; Zhang and Elliot, 2006). This addition of Pd can protect nZVI cores from corrosion (Yan et al., 2010). Hydrogen produced by nZVI corrosion will attach to the noble metal surface to catalyze reactions. The use of Pd NP catalysts alone have been described by Omole et al. (2007) for the reduction of Cr(VI) in the presence of an organic source.

Coating iron-based NP with polymers, whether with neutral or charged surfaces similar to aquifer grains, has been used to limit deposition and to increase electrostatic repulsion between NP. Common coatings include CMC (He et al., 2009a; Sakulchaicharoen et al., 2010), clays (Kim et al., 2013; Zhang et al., 2011), polyacrylamide (PAM) (Cirtiu et al., 2011), poly(acrylic acid) (PAA) (Petosa et al., 2013; Schrick et al., 2004), and xanthan and guar gum (Comba and Sethi, 2009; Vecchia et al., 2009; Tiraferri et al., 2008; Tiraferri and Sethi, 2009). Although surface coatings increase the aqueous stability and enhance the transport of nZVI and NP in porous media, these coatings may decrease reaction rates (Phenrat and Lowry, 2009) by inhibiting transport of contaminants to the nZVI surface. These two aspects must be balanced to provide optimum contaminant removal in systems requiring transport of NP. A further understanding of the surface properties of NP coatings and the ensuing mobilization of these particles will provide improvements to in situ implementation of NP-based groundwater treatment systems.

This paper focuses on the transport of superparamagnetic iron oxide nanoparticles (SPION) in porous media. These particles contain magnetite cores and are designed to be recoverable by magnetic separation from treated groundwater for potential reuse (Leshuk et al., 2013; Linley et al., 2014). Environmental applications of SPION (Horak et al., 2007; Tang and Lo, 2013) are limited to the removal of metals in water and separations (Liu et al., 2008; Singh et al., 2011), support for TiO_2 NP photodegradation of organic contaminants (Linley et al., 2014), sorption of Cr(VI) and heavy metals (Nassar, 2012; Pang et al., 2011; Zhou et al., 2011), and petroleum imaging (Xue et al., 2014; Yahya et al., 2014). However, SPION can potentially be used for *in situ* groundwater remediation. Addition of a catalyst to the surface of SPION is required to enhance the reactivity of the

particles. The superparamagnetic property of these NP allows for efficient separation from groundwater after injection of a CSA suspension for *in situ* treatment (Linley et al., 2014). Improved recovery of costly Pd incorporated into the NP and contaminants are accomplished with the magnetic separations.

In this study, controlled SPION aggregates (CSA) coated with PAM, with and without Pd catalyst, were investigated as a potential tool for groundwater remediation. Suspension, or settling, tests were conducted to assess aqueous stability and aggregation behaviour in different aqueous environments. Batch tests were performed to determine the stability of the Pd coating on the CSA. Column breakthrough tests were performed to evaluate the extent of transport of the NP in porous media. The objectives of this study were to characterize the influence of the chemical environment on CSA stability in solution and the mobility in porous media under typical geochemical conditions, including those representative of carbonate-bearing aquifers.

2.3 Materials and Methods

2.3.1 Chemicals

Salt solutions were prepared from high purity salts of NaCl (EMD, >99 %), $MgSO_4$ as $MgSO_4 \cdot 7H_2O$ (EMD, 98-102 %), $CaCO_3$ (EMD, >99 %), and $CaCl_2$ as $CaCl_2 \cdot 2H_2O$ (Sigma Aldrich, >99 %). High-purity acids included HCl (EMD, concentrated) and HNO_3 (EMD, Omnitrace). Materials for the CSA synthesis included $FeCl_3 \cdot 6H_2O$ (99 %, Sigma Aldrich), sodium citrate dihydrate (99 %, Fisher), polyacrylamide (PAM, M_W ~5-6 MDa, Polysciences), urea (99 %, Fisher), $PdCl_2$ (≥99 %, Sigma Aldrich), and ethanol (EtOH, ACS reagent grade). All chemicals were purchased and used without further purification. Ottawa silica sand conforming to ASTM-C778 20/30 sieve size (0.84 to 0.59 mm) was used as a packing material for the column tests.

2.3.2 NP Synthesis and Preparation

Synthesis of controlled SPION aggregates of iron oxide as Fe_3O_4, referred to as CSA-240, was completed following a hydrothermal process (Cheng et al., 2010; Leshuk et al., 2013). An anionic surface stabilizer, polyacrylamide (PAM) was used to coat CSA-240. Palladium was precipitated onto CSA-240 as a separate step (denoted by @Pd) to make CSA-240@Pd. A duplicate batch of CSA-240 and CSA-240-@Pd was synthesized at a later date, referred to as CSA-240' and CSA-240-@Pd'. The duplicate batches were conducted to provide NP of a similar size range for use in additional experiments.

$FeCl_3 \cdot 6H_2O$, sodium citrate dihydrate, and PAM were dissolved in 18.2 Ω cm^{-1} ultrapure water (Milli-Q, EMD Millipore) through stirring for 24 hr at room temperature. Urea was then added to the solution under vigorous stirring for 30 min, after which the final concentrations of reagents in solution were 50 mM $FeCl_3 \cdot 6H_2O$, 100 mM sodium citrate, 7.5 g L^{-1} PAM, and 0.225 M urea. This mixture was transferred to a 125 mL polytetrafluoroethylene-lined stainless steel pressure vessel (Parr) at a 66% fill fraction, which was then heated in an oven (Binder) at 2 °C min^{-1} to 200 °C, and held at this

temperature for 12 h, before removal from the oven and allowed to cool at room temperature.

Palladium deposition onto the Fe_3O_4 submicron spheres was accomplished similarly to Kong et al. (2011). The Fe_3O_4 particle powder was dispersed into a 2.5 mM solution of PdCl2 in EtOH by probe sonication (Branson, 100 W, 15 min, pulsed) to a concentration of 2 g L^{-1}. This dispersion was heated at 70 °C for 1 h under vigorous mechanical stirring.

Upon cooling, both products were recovered magnetically and washed thoroughly with deionized water and ethanol by magnetic decantation, and then dried under N_2 and in a vacuum desiccator at room temperature. After synthesis, the nanoparticles were stored dry in an anaerobic atmosphere until use. Solutions of CSA were prepared gravimetrically in ultrapure water and probe-sonicated prior to use to standardize the degree of particle aggregation.

2.3.3 Physical Characterization of Nanoparticles

The CSA were characterized via transmission electron microscope (TEM) imaging (Philips CM-10, 60 keV) to provide mean particle diameter, size distribution, and particle morphology. Samples for examination by TEM were prepared by drying a subsample of the NP suspension on a 400 mesh copper TEM grid with FormvarTM coating (Canemco). Zeta potential measurements of NP surface charge were made using Malvern Zetasizer Nano ZS90. The real and imaginary refractive indices of the material were inputted and averages from 10-100 scans, depending on the level of confidence obtained.

Dynamic light scattering (DLS; Brookhaven 90 Plus Particle Size Analyzer) of the NP suspensions provided measurements of the effective hydrodynamic size range, where effective size is defined as the size where a maximum in signal intensity occurs. Samples of low-concentration NP suspensions (0.5-4 mL) were placed into UV range polymethyl methacrylate cuvettes (VWR) for analysis. Triplicate runs of 5 minutes were

made at 90° at 659.0 nm wavelength, with a particle real refractive index of 2.160, and a particle imaginary refractive index of 1.201.

Concentrations of the NP in aqueous solutions were determined by measuring absorbance (A) with a UV-Visible spectrophotometer (HACH 2800 or HACH 2400) on suspensions contained in 10 and 25 mL glass cuvettes (HACH) or 1 mL polymethyl methacrylate cuvettes. Calibration curves with linear slopes were constructed through a series of dilutions. Although NP cause turbidity as opposed to A, the linearity of the A calibration curves was assessed using least-squares linear regression. R^2 values > 0.997 were observed for all NP types, wavelengths, and cuvettes. Less than 0.1 g L^{-1} NP was needed to provide sufficient transmittance through the sample, thus dilutions of higher NP concentration samples were prepared by volume with ultrapure water. Detection limits were approximately 0.5 mg L^{-1} (<0.1 % of NP concentrations typically used).

The NP concentrations were determined by inductively coupled plasma optical emission spectrometer (ICP-OES) analysis (iCAP 6500, Thermo Scientific) through measurement of the total Fe concentration of the suspensions. Samples were unfiltered and either acidified with 18 N HNO_3 to a pH < 2, or digested using a 1:1 dilution of a 1 mL sample with 18 N HNO_3. Digested samples were brought up to 10 mL volume by addition of ultrapure water. ICP-OES calibration standards were prepared from solutions containing the same matrix.

2.3.4 Suspension Tests

Two types of aqueous suspension tests, episodic (E-ST) and continuous (C-ST), were performed to evaluate the NP stability in ultrapure water and in different aqueous salt solutions. The NP concentrations used were 0.2 g L^{-1} for E-ST and 0.04 g L^{-1} for C-ST (unless manipulating NP concentration). The 0.2 g L^{-1} concentration was selected because it is representative of the magnitude of the NP concentrations used in many field applications (Bennett et al., 2010; Kocur et al., 2014) and conserves NP mass. The 0.04 g L^{-1} NP concentration was selected to provide A readings within the calibration range. The solutions for E-ST and C-ST were prepared through gravimetric dilution of a

concentrated NP solution and major ion stock solutions. Monovalent ions (NaCl), divalent ions ($MgSO_4$), and calcium carbonate, typical of groundwater composition, were used. Solutions were made to calculated ionic strength values and reported IS are from geochemical speciation calculations for measured cation concentrations for the solutions.

2.3.4.1 Episodic Suspension Tests (E-ST)

The E-ST were performed on the bench in sealed 20 mL glass vials with 15 mL of a suspended NP solution. The rate of aggregation and settling of the NP was monitored as a function of time using photography and direct measurement of the NP concentration. For the direct measurements, a pipette was inserted into the water column at a uniform height for each sampling event. Sampling intervals were chosen to optimize monitoring of the settling process. Sampling was terminated when no NP were visibly suspended. Samples were analyzed by DLS and ICP-OES. ICP-OES samples were 2 mL diluted up to 10 mL and were only taken at late intervals following photographic observation.

2.3.4.2 Continuous Suspension Tests (C-ST)

The C-ST were performed in a 25 mL cuvette monitored with continuous absorbance readings in a HACH 2800 spectrophotometer at a wavelength of 560 nm. Background A was determined on ultrapure water. The A of undisturbed samples was monitored continuously over the duration of the experiment. Upon termination of each experiment, the NP were resuspended and analyzed by ICP-OES for determination of total Fe and salt concentrations.

2.3.5 Durability of Pd coatings on the Pd-coated CSA

Batch tests were conducted to assess the binding of Pd on the NP. Aliquots of a stock NP suspension, NaCl and $CaCO_3$ solutions were dispensed into sealed 20 mL glass

bottles and thoroughly mixed. Eleven solutions (with replicates) were used: CSA-240' in ultrapure water, CSA-240@Pd' in ultrapure water, 10 mM IS NaCl, 1.3 mM IS $CaCO_3$ (duplicate, triplicate), and additional tests were conducted under the influence of a constant magnetic field, CSA-240@Pd' in ultrapure water in a magnetic field and CSA-240@Pd' in magnetic field duplicate. The IS of the $CaCO_3$ solutions was determined from geochemical speciation calculations using measured Ca concentrations on filtered and acidified samples and allowing the solution to attain equilibrium with atmospheric PCO_2. Tests were initiated by adding the NP to the solution, allowed the suspensions to settle between sampling events, and were resuspended after sampling. Samples were collected at the onset of the experiment (0 day), prior to resuspension at 1, 2, 6, 10, 18, 31, 80, and 120 days and following resuspension at 18, 80, and 120 days. Samples were digested and analyzed by ICP-OES.

2.3.6 Column Transport Experiments

Breakthrough column experiments were conducted to assess the NP mobility in porous media. Ottawa silica sand was washed with 10 % HCl, left in overnight, rinsed until the decant water was neutral in pH, and air dried before being dry packed into a Chromaflex column (15 cm length, 1 cm inner diameter, Kontes). The column was flushed with CO_2 prior to saturation to minimize entrapped gas. The column was then saturated with NP-free input solution prior to initiating the experiment. A high-precision peristaltic pump (Ismatec) with Pharmed® pump tubing (Cole Parmer) was used to control the flow rate. The column was oriented vertically and flow in the column was upward. Samples were collected using an automatic fraction collector (Retriever 500, Teledyne ISCO).

Various input solution compositions were used to evaluate the effect of water chemistry on NP transport. Experiments were conducted using ultrapure water, 1.3 mM IS $CaCO_3$ (10 % saturation), 5.1 mM IS $CaCO_3$ (50 % saturation), and 8.6 mM IS $CaCl_2$. Because the carbonate solution is basic, $CaCl_2$ was also used to isolate the effect of Ca on NP transport. The CSA-240 and CSA-240@Pd were used in all solution types, except

CSA-240@Pd' was used for 1.3 mM IS $CaCO_3$. Input solution pH was measured with an Orion ROSS pH combination electrode (Thermo Scientific) and SympHathy benchtop pH meter (VWR).

To assess the physical transport properties for the column packing, a conservative tracer test was performed using a 250 mg L^{-1} Cl^- (as NaCl) solution for 5 PV of flow followed by 5 PV of Cl-free input solution. Select samples were filtered with a 0.45 µm Supor® membrane filter and then analyzed by ion chromatography (IC) at the Department of Earth and Environmental Sciences, University of Waterloo.

The NP column experiments were conducted by introducing 5 pore volumes (PV) of 1 g L^{-1} NP solution, followed by 5 PV of NP-free solution prepared with the same matrix. To minimize particle aggregation prior to the initiation of the experiment, the salt solution was mixed with the NP solution through a T-joint at the same flow rate immediately before the input solution entered the column. For low mobility experiments ($CaCO_3$ and $CaCl_2$ solutions), a subsequent flushing consisting of 5 PV of ultrapure water followed by 5 additional PV of ultrapure water pumped at a higher flow rate.

The column was repacked between column tests for the cases where significant NP were retained within the porous media of the column. The porosity of the sand within the column ranged from 0.39-0.41 and the pore volume ranged from 4.6-4.8 mL. A flow rate of 6-10 mL hr^{-1} was selected for these experiments, corresponding to a linear groundwater velocity of 5-10 m day^{-1}. A higher flow rate (26 mL hr^{-1}, or 20 m day^{-1} linear groundwater velocity) was used to promote NP transport for the cases when minimal NP transport occurred at the lower velocity.

Column effluent samples of the NP breakthrough tests were analyzed for NP concentration via a spectrophotometer (HACH 2400) at 562 nm in disposable cuvettes immediately after collection. Dilutions were made as needed to obtain NP concentrations within the linear range of the calibration curve. NP concentrations that eluted from the column were reported relative to the NP input concentration versus time.

2.3.7 Reactive Solute Transport Model Simulations and Attachment Efficiency Equation

The column tracer test and NP breakthrough experiment results were simulated using the STANMOD CXTFIT 2.1 software package (Toride et al., 1999) under non-equilibrium and equilibrium conditions. The equilibrium model solves the advection-dispersion saturated homogeneous 1-D flow equation (Freeze and Cherry, 1979) as a function of time (T), distance (L), and mass (M):

$$\frac{\partial C}{\partial t} = D_l \frac{\partial^2 C}{\partial x^2} - v \frac{\partial C}{\partial x} - \frac{\rho}{\theta} \frac{\partial Q}{\partial t}$$

where C is aqueous concentration (M L^{-3}), t is time (T), D_l is the longitudinal dispersion coefficient (L^2 T^{-1}), x is position along the one dimension (L), v is average linear groundwater velocity (L T^{-1}), ρ is bulk density (M L^{-3}), θ is porosity (-), and Q is sorbed solute mass per mass of solid phase at equilibrium (M M^{-1}). The process of sorption (and attachment for NP) affects the velocity of a species ($v_{species}$) relative to water, expressed quantitatively by the retardation factor (R):

$$R = \frac{v}{v_{species}}$$

D represents the spread of solute or particles due to mechanical processes and diffusion, is a property of the fluid and solid, and is related to longitudinal dispersivity (a_l), a property based on the porous media, by:

$$D_l = a_l v + D^*$$

where D* is the coefficient of molecular diffusion (L^2 T^{-1}). In simulations run, optimized parameter fitting using non-linear least-squares is used to obtain transport coefficients from experimental data. Tracer test results were modelled to determine the dispersion coefficient and pore volume. The experimental data from each NP breakthrough curve and the dispersion and pore volume determined by the tracer test were used to estimate retardation, NP mass of the input, and nonequilibrium transport

parameters. Quantification of the mobility of the NP was estimated by calculating the attachment efficiency (Tufenkji and Elimelech, 2004):

$$\alpha = \frac{-2\ d_c}{3\ (1-\theta)\ L\ n_o} \ln\left(\frac{C}{C_0}\right)$$

defined as the fraction (numerically limited between 0-1) of collisions between collector and NP that lead to attachment, where dc is the collector grain diameter (L), θ is porosity, L is column length (L), η0 is the single-collector contact efficiency described within Tufenkji and Elimelech (2004), C is a representative NP concentration after NP elution (M L^{-3}), and C_0 is the NP input concentration (M L^{-3}). η0 was calculated using equation 17 from Tufenkji and Elimelech (2004). C used here was the average concentration eluting between 1.8-2.2 pore volumes. Alternatively, with the attachment efficiency equation rearranged, NP transport distance can be calculated assuming 1% of the relative NP is transported (Yao et al., 1971):

$$L_{1\%} = \frac{-\ 2\ d_c}{3\ (1-\theta) n_0\ \alpha} \ln(0.01)$$

2.4 Results and Discussion

2.4.1 Physical Characterization of Nanoparticles

The CSA particles consist of spherical aggregates of SPION (< 50 nm diameter) and appear uniform in size as observed in TEM images (Figure 2.1) of CSA-240 and CSA-240@Pd. Coarse growths beyond the circular aggregated rim suggest Pd accumulation on the surface of CSA-240@Pd (245 nm) versus no growths on CSA-240 (240 nm).

CSA have a surface charge of -48 $\pm$ 6 and CSA@Pd -45 $\pm$ 7. This is likely due to the carboxylic acid groups on the surface, as the surface charge on synthetic magnetite and hematite would be close to zero or slightly positive in similar solutions based on the zero point charge (ZPC) of magnetite of pH = 8 and hematite of pH = 6.5-9.1 (Lin et al., 2010) or mostly within pH = 6.5-8 (Kosmulski, 2004). Within this range these Fe-based NP will be relatively unstable based on surface charge in near-neutral pH solutions. As the pH increases or decreases, the magnitude of surface charge on the NP will increase, increasing particle-particle repulsive forces, and thus stability.

Measured with DLS (Figure A.1), particle size distributions of the fresh NP indicated an effective diameter and polydispersity of 275 nm and 0.059 for CSA-240 and 252 nm and 0.028 for CSA-240@Pd. The multimodal size distribution curves for CSA-240 had two peaks, at 60 nm with >95 % of the intensity and at 260-310 nm, resulting in a multimodal size distribution (MSD) mean of 90 nm. CSA-240@Pd had only one mode, 245-265 nm, with a MSD mean of 251 nm. CSA-240' and CSA-240@Pd' DLS measurements show larger diameter (~310 nm) but a narrow size distribution, which is consistent between with and without Pd. Based on an experiment to determine a standardized method to prepare NP for experimentation (Appendix A and Table A.1), probe sonication of CSA suspensions were completed before any experiment.

Appendix F shows the linear correlation between NP concentration and ICP-OES determined Fe concentration. Based on this high linear correlation, Fe concentration can be used as an indicator for NP concentration.

PAM, used to coat the NP, is non-ionic and used as a flocculent in water treatment (Yang et al., 2004). Unlike anionic coatings, such as polyacrylic acid, PAM is not sufficiently charged to provide electrostatic stabilization of the particles or to overcome electrostatic repulsion associated with negatively-charged silica-based soil particles. However, PAM should hydrolyze to PAA under the hydrothermal conditions used during the synthesis of the NP. Sodium citrate was also used during the NP coating step, increasing the anionic carboxylate density.

2.4.2 Suspension Tests

2.4.2.1 Episodic Suspension Tests (E-ST)

Settling of the suspensions was documented in E-ST as a function of time through a series of photographs for CSA-240 and CSA-240@Pd (Appendix D). The least settling was observed for suspensions in ultrapure water and 2 mM IS NaCl solutions, with at least half of the NP in samples remaining suspended after 46 hours and some still remaining in suspension after 100 hours (photographs not shown). The most rapid and extensive settling was observed in the $CaCO_3$ solutions. Comparing CSA-240 and CSA-240@Pd, more CSA-240@Pd remained suspended in all the salt solutions at 2 and 6.5 hr. CSA-240@Pd settled out from the salt solutions between 10-16 hours (not shown). These observations suggest that the extra synthesis step for the Pd coating altered the NP surface properties, and subsequently increased the NP stability in these solutions. The more rapid settling is due to higher particle-particle aggregations caused by a thinner double layer (Ryan and Elimelech, 1996).

Stability results from E-ST observed in this study are within the range observed in other studies. For example, nZVI@Pd uncoated and coated with CMC, PVP, and guar gum in non-ionic solutions showed settling of uncoated NP within 1 hr, whereas CMC and guar gum-coated NP remained fully suspended at 48 hr (Sakulchaicharoen et al., 2010). A dramatic decrease in the stability of metal oxide NP in Ca solution, despite the addition of stabilizing natural organic matter, was attributed to the effect of Ca^{2+} due to its positive charge (Zhang et al., 2009), similar to the stability observed in the present

study. Suspensions of 30 g L^{-1} nZVI in a high viscosity 6 g L^{-1} xanthan gum matrix remained stable for days in solutions with IS up to 12.5 mM of NaCl and $CaCl_2$ (Comba and Sethi, 2009). The higher NP stability observed by Comba and Sethi (2009) compared to the stability observed in this study is attributed to the higher polymer concentration and the rheological behaviour of the suspension, which does not apply at NP concentrations used here.

The results of E-ST samples (Figure 2.2) indicate that the total Fe concentrations are linearly correlated to the NP abundance (Appendix F). Therefore, the experimental results are expressed relative to the initial total Fe concentration. In the ultrapure water suspensions (Figure 2.2a), the total Fe concentration decreased to 7-36 % of the initial concentration after 100 hr, which is consistent with the photographic record at 46 hr. In NaCl and $MgSO_4$ solutions (Figure 2.2 b) total Fe concentrations decreased rapidly to values approaching the detection limit within 20 and 80 hr, respectively. The suspensions in the $CaCO_3$ solutions (Figure 2.2c) showed the most rapid settling (under 1.7 hours) of the NP. CSA suspensions in $CaCl_2$ were similar to $MgSO_4$ divalent solutions. These results are consistent with the photographic observations from E-ST experiments.

2.4.2.2 Continuous Suspension Tests (C-ST)

Absorbance curves from the C-ST experiments showed minimal settling in ultrapure water and 2 mM IS NaCl solutions over 50 hours (Figure 2.3 a and b). As the NaCl concentration increased to 5 and 10 mM IS, the NP stability dramatically decreased, suggesting a threshold solute concentration for stability. The NP were more unstable in the $MgSO_4$ (Figure 2.3 c) and $CaCO_3$ (Figure 2.3 d) solutions, with the lowest stability observed in the more concentrated $CaCO_3$ solutions. The times required for the relative absorbance (A/A_0) to decrease to 0.9 and 0.5 indicate that shorter suspension durations occurred in solutions with higher salt concentrations and in the presence of divalent ions (Table 2.1). Replicate samples of 1.3 mM IS CaCO3 in CSA-240

suspensions produced irreproducible results, from high to low stability, and thus have not been included.

Similar stabilities of CSA-240 and CSA-240@Pd were observed during the C-ST experiment, in contrast to the E-ST. Sakulchaicharoen et al. (2010) observed > 50 % settling of polymeric-coated NP, and very rapid settling of NP coated with polyvinylpyrrolidone, in C-ST of non-ionic solutions. Esfahani et al. (2014) observed that the stabilities of nZVI with PAA and PVP coatings were similar to the results observed in this study for CSA.

The NP concentrations were 0.2 g L^{-1} for E-ST experiments and 0.04 g L^{-1} for the C-ST experiments. A comparison of the E-ST and C-ST experiments indicate that although the methods and data types differ the factors affecting NP stability are similar. However, stability depends on the NP concentration (He et al., 2008), as suspensions with lower NP concentrations are more stable as fewer collisions between NP occur. Here, low NP suspension concentrations (C-ST relative to E-ST) were more stable in ultrapure solutions and in NaCl solutions (Figure 2.2 versus 2.3). The methods of observation between E-ST and C-ST are different but still allow for comparisons to be made between the results.

A comparison of the results of the E-ST and C-ST experiments conducted indicate that there appears to be a threshold salt concentration that causes significant declines in NP stability. This threshold is the critical coagulation concentration (Chen and Elimelech, 2006). Due to the limited electrolyte concentrations used, the CCC cannot be defined. However, this observable threshold was found at 4mM IS for NaCl for CSA-240 and CSA-240@Pd. For MgSO4 the threshold is below 2 mM IS; this lower value is probably due to the presence of divalent ions. For $CaCO_3$, the threshold is below 1.3 mM IS, a concentration below environmentally relevant concentrations. Thus, the presence of Ca and bicarbonate at typical environmental aqueous concentrations is expected to cause destabilization. At concentrations above these thresholds, immediate settling (defined as 90% decrease in A within 3 hours) usually results.

2.4.3 Durability of Pd coatings on the Pd-coated CSA

Batch tests conducted with CSA-240@Pd' were used to assess the persistence of the Pd-coating on the CSA surface (Appendix G). Sampling the aqueous phase (with NP settled) enabled determination of the mass of Fe and Pd in solution derived from physical or chemical breakdown of the CSA. Sampling the suspension prior to settling yields the NP concentrations and the Fe:Pd ratio. After adjusting for experimentally introduced changes, Na concentrations were 96-120 % for 11 sampling events of eight samples each over a 120 day period (data not shown). Concentrations of Ca decreased by 20-30 % in samples containing $CaCO_3$ and were undetected in solutions samples above the settled CSA, suggesting the loss of Ca mass and the potential partition to the NP phase due to interaction of Ca with the functional groups of the PAM coating. Pd was undetected in the solution above the settled samples at 18, 81 and 120 days in 10 mM IS NaCl solutions, $CaCO_3$ solutions, and after application of a magnetic field. These results indicate that at least 80-90 % of the Pd remained on the CSA. From 0 to 120 days, a 3 % decrease of the mean Pd/Fe ratio was observed (standard deviations < 5 %) for eight samples over time. This decreased Pd relative to Fe may indicate > 95 % of the Pd remained on the CSA particles. On the scale of months, the CSA are expected to retain sufficient Pd to catalyze contaminant removal reactions and could be potentially recycled for reuse.

2.4.4 Column Transport Experiments

The column breakthrough curves (Figure 2.4) show normalized concentrations of CSA-240 and CSA-240@Pd in ultrapure, 1.3 and 5.1 mM IS $CaCO_3$ solutions, compared to a Cl^- tracer test result.. The flow rates selected for these experiments were similar to groundwater velocities typically observed during pumping stages of remediation programs (5-10 m day^{-1}), as it is anticipated that these NP will be used in a pumping flow regime during field applications. This velocity range corresponds to volumetric flow rates of 6-13 mL hr^{-1} through the column (approximately 1.5-3 PV hr^{-1}). A higher flow

rate (26 mL hr^{-1}, or 20 m day^{-1} linear groundwater velocity) was used when minimal NP transport was observed. The pH of the input solutions was: 5.6 for solutions containing NaCl and $CaCl_2$, 6.4 for 1.3 mM IS $CaCO_3$, and 6.3 for 5.1 mM IS $CaCO_3$. Based on PHREEQCi simulations, the pH in $CaCO_3$ solutions would be higher, 7.9 and 8.5. Ionic strength values were lower in simulations based on calculated IS, suggesting precipitation of calcite occurred.

Column tests were conducted under a dynamic flow environment, while suspension tests were conducted in a static environment. Although results between the studies can be compared, differences may result from different mechanisms of instability or removal. For instance, in suspension tests NP settle (sedimentation) downward through stagnant water. However, the columns had moving water in an upward flow direction, thus sedimentation will likely lead to a different behaviour.

The breakthrough curves for the conservative tracer, Cl^- (black circles of Figure 2.4), and CSA-240 and CSA-240@Pd in ultrapure solution (red triangles of Figure 2.4) were very similar. Within calculation and analytical uncertainty, all NP were eluted from the column in ultrapure water matrices (Table 2.2). For solutions containing ions (data along x-axis of Figure 2.4 and 2.5), attenuation of the NP was observed, with a portion of the NP transported without retardation. A portion was completely attenuated, mostly retained within the first few cm of the column inlet. An average NP breakthrough concentration of 0.9 % of the input concentration of CSA-240 eluted from the 1.3 mM IS $CaCO_3$ column experiment, 0.5 % for CSA-240 in 5.1 mM IS $CaCO_3$, 0.4 % from CSA240@Pd in 1.3, and 0.2 % from the CSA-240@Pd in 5.1 IS mM $CaCO_3$ matrices (Figure 2.5). Cumulative percentages of CSA eluting from the column within the first 10 PV were under 0.8 % for CSA-240 and under 0.4% for CSA-240@Pd (Table 2.2). The effective diameter of NP eluted from the column in $CaCO_3$ experiment increased from 240 nm in the input solution to 568 nm and 620 nm after 2 and 4 PV, respectively. This change likely resulted from aggregation of NP and subsequent retention in the column as the NP attached to the sand grains.

A modified flushing sequence was implemented during the experiments conducted with $CaCO_3$ and $CaCl_2$ solutions, to observe the effects of dynamic conditions on NP elution (Figure 2.5 is extended data from Figure 2.4). A total of 20 PV of various

solutions (ultrapure water, 1.3 or 5.1 mM IS $CaCO_3$, and 8.6 mM IS $CaCl_2$) was pumped through the column at two flow rates (9 mL hr^{-1} and 25 mL hr^{-1}). A noticeable release of NP, up to twice the amount of the initial elution, occurred following the change from the $CaCO_3$ solution to ultrapure water, and equal to five times in ultrapure water following the increase in the column flow rate from 9 mL hr^{-1} to 25 mL hr^{-1}. With both 1.5 and 7.4 mM IS $CaCO_3$ solutions, strong immobilization and irreversible attachment occurred for the majority of the CSA, followed by a small percentage of CSA which detached following the change in solution composition. This detachment is attributed to the decreased IS and increased shear stress (Bergandahl and Grasso, 2003) and the associated release of previously attached NP and can be explained by DLVO theory.

Transport of the CSA-240 was minimal during the 8.6 mM IS $CaCl_2$ column test, with only 0.3 % of the NP eluted from the column after 10 PV (Figure 2.6). However, following the transition from the $CaCl_2$ solution to ultrapure water, ~100 % of the NP were observed to elute from the column. In comparison, in the $CaCO_3$ solutions, a maximum of 5 % of the NP was eluted over the flushing sequence (Table 2.2). Similar observations of NP transport in $CaCl_2$ solutions, have been attributed to particle detachment, likely due to decreased ionic strength (Bergendahl and Grasso, 2003; Li et al., 2010; Shen et al., 2012). An increase in transport between the $CaCl_2$ and $CaCO_3$ column tests may be caused by a lower pH.

Detachment occurs when modifications to the physicochemical conditions are caused by decreased ionic strength (Bergandahl and Grasso, 2003), altered flow regime (Ryan and Elimelech, 1996), or cation exchange reactions (Shen et al., 2012) and cause the secondary minimum to decrease in depth allowing for the detachment of NP. Li et al. (2011) observed attachment followed by detachment, with up to 0.7 relative concentration (C/C0) of CeO_2 NP eluting upon flushing with ultrapure water following a NaCl solution. Shen et al. (2012) saw release of polystyrene latex NP from a column after NaCl was flushed through from the column replacing $CaCl_2$. In contrast to the sustained immobilization observed with $CaCO_3$ solutions, the $CaCl_2$ input solution caused temporary retention and the NP were remobilized after IS decreased. Jaisi et al. (2008) observed detachment following the removal of K^+ from the input solution, but not after removal of Ca^{2+}. For KCl, NP attached in the secondary minimum, which can be

removed and result in detachment; while, with Ca ions, the NP attached in the primary minimum and thus remained attached (Hahn et al., 2004). The reversible attachment observed here is crucial for practical applications of NP for groundwater treatment. Water groundwater chemistry, which affects the mobility of NP, can be manipulated during the implementation of the remediation system by pumping customized input solutions resulting in the potential for development of controllable NP injection-and-release-and-collect treatment systems.

Results from this study indicate that increased concentrations of dissolved $CaCO_3$ resulted in decreased CSA transport. Other studies of NP transport found that calcite-bearing porous media limited NP transport (Laumann et al., 2013) with maximum NP elution from column tests below 20 % in carbonate sand compared to above 80 % for quartz sand. This decrease may be attributed to interactions between the Ca and the PAA or PAM coatings and a lower negative surface charge on calcite.

The modest NP transport observed in $CaCO_3$ solutions during this study is consistent with other studies on Fe-based NP. For example Alaskar et al. (2011) conducted column transport experiments with uncoated hematite (surface charge = +59 mV) with undetected elution and with PVP coated NP (-9.5 mV surface charge) with a maximum C/C_0 of 0.1 elution for a glass bead packed column. Despite the CSA having a large negative surface charge, this stability is overcome in $CaCO_3$ solutions. Ben-Moshe et al. (2010) observed minimal transport of magnetite NP in ultrapure solution through glass bead columns, with only 4 % of the particles recovered. Use of NaCl solutions of up to 100 mM resulted in even less transport. Tosco et al. (2012) observed full breakthrough of ferrihydrite NP in NaCl solutions < 5 mM IS yet observed about 0.5 NP breakthrough at 10 mM IS NaCl. No studies evaluating Fe-based transport in $CaCO_3$ environments were identified, however, Ca has consistently caused minimal transport with irreversible attachment (Wang et al., 2008b)

In the column tests CSA-240 showed a slightly higher stability compared to CSA-240@Pd, the opposite of trends observed during E-ST experiments. Both differences are small relative to the range of stabilities observed under varied experimental conditions, and may be caused by variations in NP preparation prior to experimentation despite efforts to maintain uniform preparation methods. Results for ultrapure water and $CaCO_3$

solutions in both suspension tests and column tests showed high stability with minimal aggregation for ultrapure water and low stability with high aggregation for $CaCO_3$ solutions. NaCl and $MgSO_4$ solutions were not used for column tests; however, similar behavior would be expected for NaCl and $MgSO_4$ compared to $CaCl_2$, only with incomplete attachment during NP introduction.

Full transport in ultrapure suspensions is informative, however is of limited use in natural environments. It is rare to have natural systems with such purity. Low solute concentration groundwaters are present in northern Canadian Shield regions of Canada (Yang et al., 1996) due to the low population density and local geology with total dissolved solids often < 50 mg L^{-1}, corresponding to ~4 mM IS of divalent ions. To simulate natural waters, solutions used in this study contained major ions common in the environment at environmentally relevant concentrations. In many groundwaters, concentrations of dissolved $CaCO_3$ are controlled by pH and equilibrium with respect to $CO_{2(g)}$ and solid calcite. In this study, the $CaCO_3$ input solutions represented water that was diluted at 10 % and 50 % (resulting in 1.3 and 5.1 mM IS $Ca(HCO_3)_2$ of a stock solution that was prepared by equilibrating $CaCO_3$ with air at atmospheric CO_2 pressure. Depending on pH and the pressure of CO_2, much higher concentrations of $CaCO_3$ can be observed in groundwater. The presence of NaCl in groundwater is common due to the high solubility of Cl-bearing mineral phases. Background Cl concentrations in groundwater are often < 10 mg L^{-1} but increase in urban and industrial centres and where road salt is applied. Concentrations up to 10 mM IS NaCl (230 mg L^{-1} Na and 355 mg L^{-1} Cl) were used in these experiments, around the higher limits established as an aesthetic objective in Canada (Health Canada, 2010). These concentrations are greater than commonly observed in groundwater systems for potable water supplies, but are not beyond concentrations observed in many natural systems. The presence of $MgSO_4$ in groundwater is also common. The maximum SO_4^{2-} concentration used in this study (240 mg L^{-1}) is not unusual and is less than half the aesthetic objective for sulfate in Canada. Contaminated waters will often have higher total dissolved solids than natural waters and both will contain more complex matrices relative to the pure systems evaluated in this laboratory-based study. Design of a field system could include a stage where attachment

is promoted until treatment, followed by detachment through a series of injections with differing flow rates and ionic compositions.

2.4.5 Reactive Solute Transport Model Simulations and Attachment Efficiency Equation of Column Results

The non-equilibrium reactive solute transport model, STANMOD CXTFIT 2.1, was used to simulate the results of the column experiments. The simulations of deterministic non-equilibrium conditions under a two-region physical model (not shown) approached equilibrium conditions ($R^2 > 0.986$ in ultrapure water column tests with fitted parameters 95 % confidence interval being < 2.5 % normalized), and thus, only equilibrium simulations are described further (Figures 2.4 and 2.5). Models shown in Figure 2.5 are only through the first 10 PV (flushing sequences i and ii). The poor fit in low-transport column tests (especially Figure 2.5b) is likely caused by low NP concentration, or absorbance, relative to the background.

The dispersion coefficient determined from the chloride tracer test (4 cm^2 hr^{-1}, or a dispersivity of 0.1 cm) was applied for the simulations of the NP transport. The pore volume was adjusted until retardation of the conservative tracer was 1.00. Retardation coefficients of 0.91 and 0.93 were determined for column tests of NP transport in ultrapure water suspensions (Table 2.2).Transport of CSA-240@Pd in 5.1 mM IS $CaCO_3$ resulted in greater retardation (R=1.40), possibly due to low sampling frequency. The remaining $CaCO_3$ column tests had R= 0.75 for CSA-240 in 1.3 mM IS $CaCO_3$, and 0.60-0.56 for CSA-240@Pd in $CaCO_3$ solution. Due to the fact that elution of the NP occurred simultaneous to the Cl and R is defined to be ≥ 1, fitted R values (Table 2.2) are inconsistent with the observed transport, breakthrough curve models, and the retardation definition. For the cases with higher total dissolved solids, the fraction of NP eluted from the column was similar to the NP concentrations estimated by the simulations (Table 2.2).

The physicochemical mechanisms controlling transport of nanoparticles in porous media differ from those controlling dissolved species. Transport of NP is restricted to

wider pores, often resulting in more rapid travel times and lower dispersion, due to exclusion of NP from more tortuous paths, leading to less extensive attachment (Stimson, 2008). Decreases in the extent of dispersion and at early breakthrough times relative to conservative tracers were not observed in these experiments. The coarse sand used in the experiments relative to the NP size (240 nm) may have limited these effects.

Attachment efficiency has been used extensively to describe colloid and NP transport in porous media (Tufenjki and Elimelech, 2004; Petosa et al., 2010). The α values calculated for the column test results ranged from 0.0 from ultrapure suspension column tests to 3.8 for CSA-240@Pd in 1.3 mM IS $CaCO_3$ (Table 2.2). Although attachment efficiency is defined as a fraction limited between 0-1 (Tufenkji and Elimelech, 2004), experimental values can be > 1. In this study, values > 1 will be used as an indication of minimal transport. As α is defined from CFT, non-CFT mechanisms are likely at play resulting in high removal of NP. These mechanisms include ripening and straining.

The significance of straining with regard to NP size and collector size has been discussed (Bradford et al., 2002; Sakthivadivel et al., 1969). With a median grain size of 0.7 mm used in this study and the largest NP diameter used (340 nm), straining is not expected to be an important mechanism and CFT theory may still apply. However, these particles do aggregate into larger particles, especially in the presence of $CaCO_3$. Aggregation of three or more particles would increase the NP size sufficient to cause significant straining. The inclusion of straining into CFT models would likely produce better fits.

Transport distances, where 1 % of the NP were transported, were quantified (Table 2.2) from column studies. Transport distances indicated transport for long distances in ultrapure water (34 m or >500 m), but short distances in $CaCO_3$ solution (5.9 m or <0.25 m).

Comparison of these values to published values for similar studies (Table 2.3) indicate that α values for experiments conducted using solutions containing high concentrations of dissolved constituents, especially divalent cations, are higher than values obtained from experiments conducted using ultrapure water. Table 2.2 shows the attachment efficiency of other iron-based column test studies where different flow rates,

NP coatings, and porous media are investigated. Attachment efficiency values for $CaCO_3$, not encountered in previous studies, and $CaCl_2$ experiments exceeded 3.0 in this study. These observations show the limited extent of CSA-240 and CSA-2404@Pd transport in $CaCO_3$ solutions, relative to observations from other column studies.

The recovery of Pd-coated CSA is desirable due to the high cost of Pd. In typical aquifer systems containing $CaCO_3$, recovery of these NP is likely to be limited using common solutions due to the high rates of aggregation. To improve transport, NP properties (charge, size, suspension concentration), porous media charge, solution properties (pH, IS, organic matter, and humic acid), and flow rate need to be considered and/or manipulated to obtain optimum transport. Beyond using polyelectrolyte coatings, polyelectrolytes can be injected in solution with the NP. Laumann et al. (2014) injected NP with unbound polyelectrolytes and promoted a 100 % increase in elution of NP in a column containing sand by adding 0.5 g L^{-1} lignin sulfonate. Optimizing the coating can also increase mobility. Because Ca is a common ion in the environment and because the CSA coating can complex with Ca, a coating that is inert to Ca is an important property.

2.5 Conclusions

Superparamagnetic iron oxide nanoparticles coated with PAM and Pd to enhance hydrogenation reactions were evaluated for stability and mobility in porous media. The particles were designed to be recovered by application of a magnetic field, to allow potential reuse of the particles. The particles showed a range in stability in different electrolyte solutions which ranged from highest to lowest, in ultrapure, NaCl, $MgSO_4$, $CaCl_2$, and $CaCO_3$ solutions. Higher ionic strength, ionic charges, and NP concentrations led to decreased stability. Particularly strong aggregation was observed in the solutions containing relatively low concentrations of $CaCO_3$.

The transport of CSA-240 and CSA-240@Pd in column transport studies differed minimally, suggesting the addition of Pd resulted in minimal modifications to the size and surface properties of the NP. Near-conservative behaviour of both CSA-240 and CSA-240@Pd was observed in column experiments with ultrapure water suspensions as an input matrix, but almost complete, irreversible attenuation of NP (> 95 %) was observed in $CaCO_3$ solutions. In a separate experiment, attachment of CSA was observed in solutions containing $CaCl_2$, followed by full detachment in ultrapure water. These differences between transport in $CaCO_3$ *versus* in $CaCl_2$ solutions suggest that not only does ionic strength, ion charge, and flow rate matter, but also pH. The variation in pH likely affected not only the surface charge of the porous media, but also the surface charge and stability of the organic coating applied to the NP. Attachment efficiencies close to zero were calculated for transport experiments with ultrapure water, whereas values > 3 were obtained for $CaCO_3$ solutions. Colloidal filtration theory seems insuficent in modelling CSA transport. Straining is a likely mechanism that needs to be considered in models. These results suggest that there is potential to inject and recover CSA-240@Pd in groundwater systems containing limited concentrations of dissolved monovalent ions, but additional modifications will be required to use these particles in carbonate-bearing aquifers, particularly under high pH conditions. Consideration of the groundwater composition where injection is to occur is critical to the success of this approach.

2.6 Figures

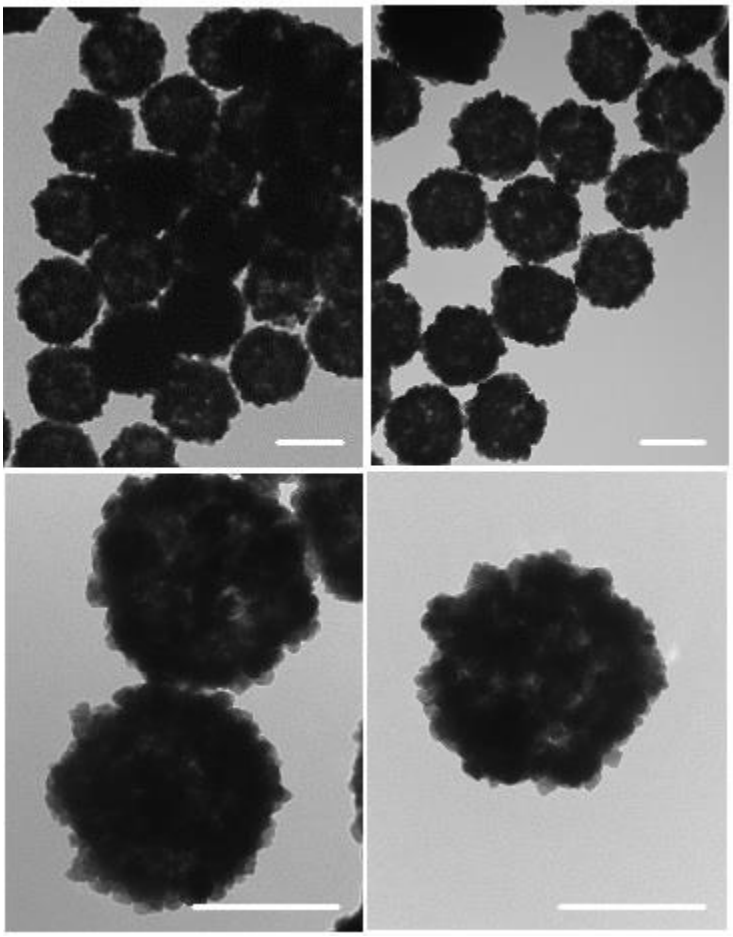

Figure 2.1. TEM images of CSA-240 (left) and CSA-240@Pd (right). The scale bar is 200 nm.

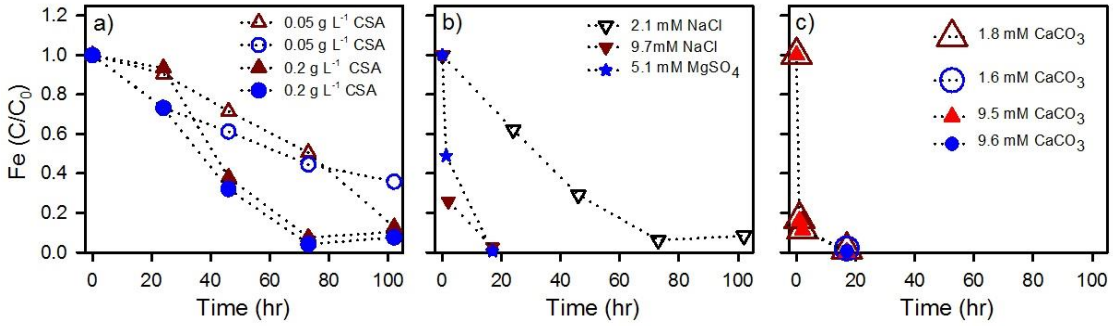

Figure 2.2. Results of temporal sampling of the E-ST experiments conducted in different aqueous solutions. Relative concentrations of Fe (C/C_0) in CSA-240 (triangles and star) and CSA-240@Pd (circles). Subplots represents suspensions containing a) 0.05 and 0.2 g L^{-1} CSA-240 and CSA-240@Pd in ultrapure water, b) 0.05 g L^{-1} CSA-240 with variable ionic strengths of NaCl and $MgSO_4$, and c) 0.05 g L^{-1} CSA-240 and CSA-240@Pd with variable ionic strengths of $CaCO_3$. Hollow symbols represent low concentrations and solid are higher concentrations.

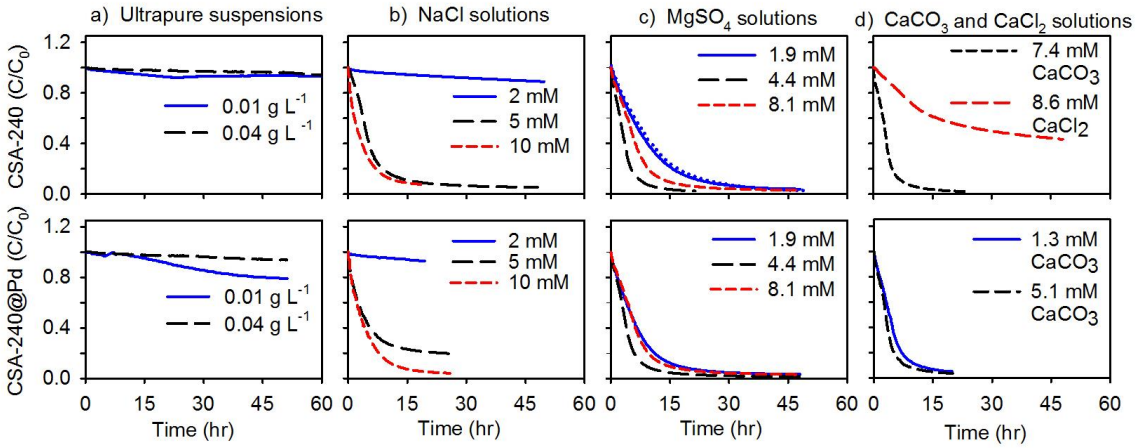

Figure 2.3. Continuous suspension test results for various salt environments and CSA concentrations. All are at 0.04 g/L CSA (unless stated) and have been normalized (C/C_0) to an absorbance of 1 at 0 hr. Top set corresponds to CSA-240 and the bottom to CSA-240@Pd. The columns represent ionic strengts of a) ultrapure suspensions, and b) NaCl, c) $MgSO_4$, and d) $CaCO_3$ solutions.

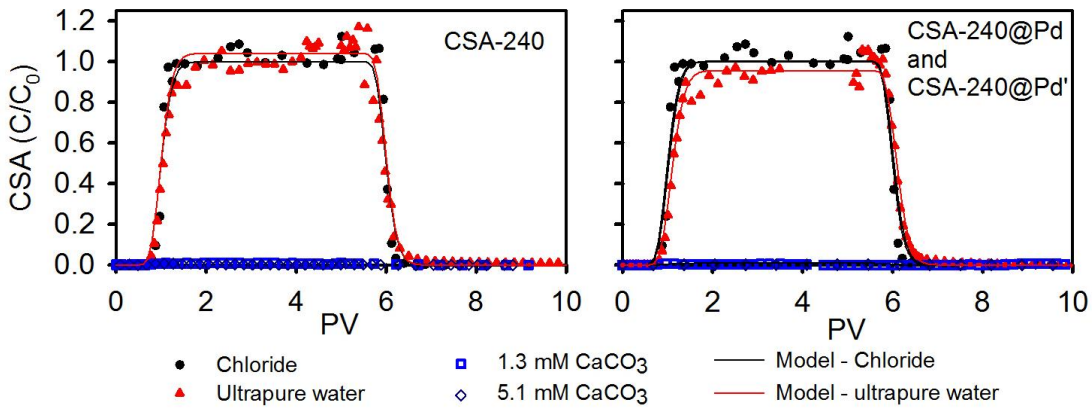

Figure 2.4. Relative concentrations (C/C_0) of Cl (filled black circles), and CSA-240 and CSA-240@Pd in ultrapure water (filled red triangles), 1.5 mM IS $CaCO_3$ (hollow blue squares) solution, and 7.4 mM IS $CaCO_3$ (hollow dark-blue diamonds) solution, and model simulations (lines) as a function of pore volumes. Note: Low mobility of CSA-240 and CSA-240@Pd in $CaCO_3$ solutions (blue symbols along x-axis); CSA-240@Pd' was used in 1.3 mM IS $CaCO_3$. See Figure 2.5 for expanded scales.

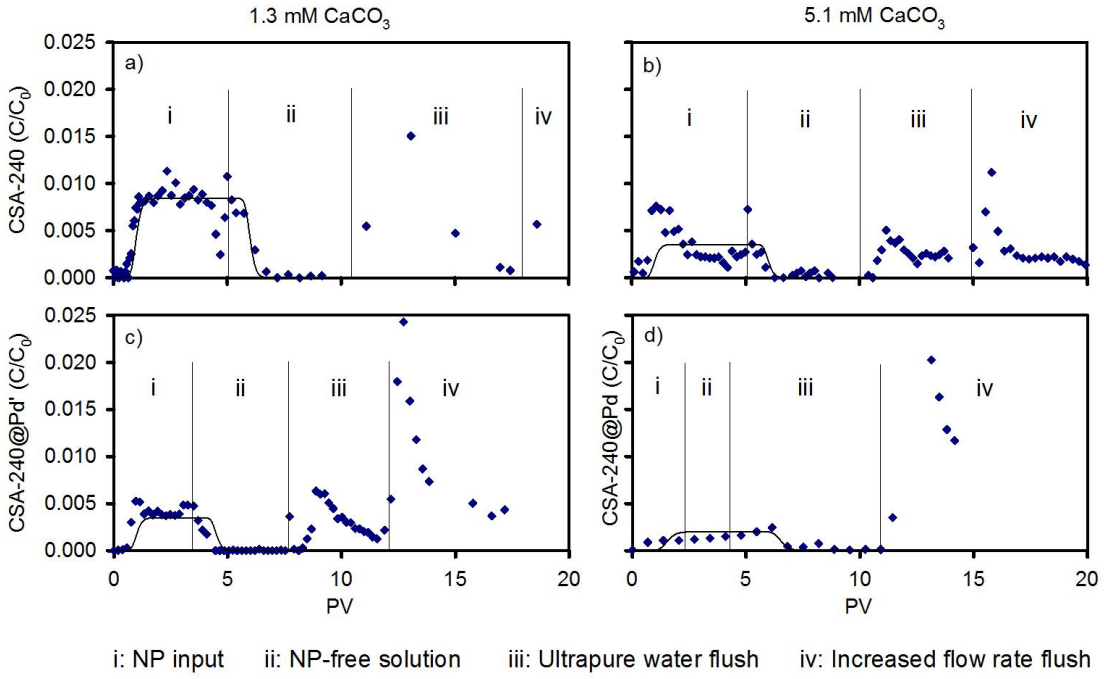

Figure 2.5. Relative concentrations (C/C_0) of a) CSA-240 in 1.3 mM IS $CaCO_3$ solution, b) CSA-240 in 5.1 mM IS $CaCO_3$ solution, c) CSA-240@Pd' in 1.3 mM IS $CaCO_3$ solution, and d) CSA240-@Pd in 5.1 mM IS $CaCO_3$ solutions as a function of pore volumes. Complete column flush sequences are i) CSA input, ii) CSA-free $CaCO_3$-containing solutions, iii) ultrapure input solution, and iv) ultrapure solution at a higher flow rate. Note: The y-axis has a maximum value of 2.5 % of the NP input concentration, and model simulations only extend to 10 PV.

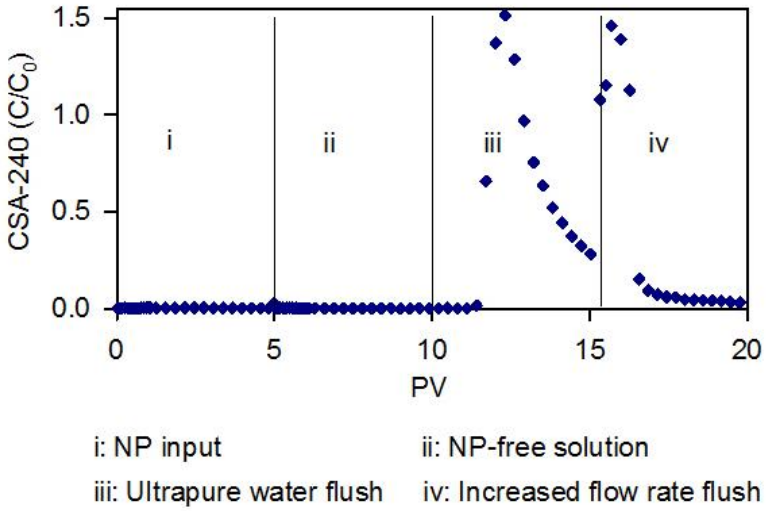

Figure 2.6. Relative concentration (C/C_0) of CSA-240 as a function of pore volumes in 8.6 mM IS $CaCl_2$ solution showing complete column flush sequence of i) CSA input, ii) CSA-free $CaCO_3$-containing solutions, iii) ultrapure input solution, and iv) ultrapure solution at a higher flow rate. Note: The y-axis has a maximum value of 150 % of the input concentration.

2.7 Tables

Table 2.1. Quantification of stability using time (hour) until 10 % and 50 % absorbance loss during continuous suspension test.

		Time (hr) till Relative Absorbance Reached Thresholds			
		CSA-240		**C-240@Pd**	
Solution Composition	**Concentration**	**0.9**	**0.5**	**0.9**	**0.5**
Ultrapure suspensions (CSA g L^{-1})	0.01	>> 70	>>70	22	>50
	0.04	>70	>>70	>50	>>50
NaCl (mM IS)	2.0	43	>>50	10	>45
	10.0	0.25	2.4	0.45	3.0
$MgSO_4$ (mM IS)	1.9	1.2	7.6	0.6	5.2
	4.4	0.35	3.0	0.6	3.4
$CaCO_3$ (mM IS)	1.3	0.45	4.0	0.6	3.9
	5.1	0.40	3.0	0.4	3.0

Table 2.2. Transport parameters determined from column breakthrough curve data, using non-linear least squares fit (STANMOD), and the attachment efficiency equation.

Column				Fitted R from		
NP	**Salt Solution**	**% CSA Eluted**	**Fitted C/C_0**	**Mass Estimate Simulation**	**Attachment Efficiency**	**Transport Distance (m)**
CSA-240	Ultrapure	107	1.00	0.91	0.00	>500
	1.3 mM IS $CaCO_3$	0.3	0.008	0.75	>2	0.15
	5.1 mM IS $CaCO_3$	0.3	0.004	0.60	>3	0.13
	8.6 mM IS $CaCl_2$	0.3[a], 100[b]	0.002	0.63	>3[a], < 0.0[b]	0.11
CSA-240@Pd	Ultrapure	97	0.99	0.93	0.05	7.3
	1.3 mM IS $CaCO_3$	0.4	0.003	0.56	>3	0.13
	5.1 mM IS $CaCO_3$	0.8	0.002	1.40[c]	3	0.10
Chloride		107	1.10	1.00	0.00	>500

[a] values obtained during transport in 8.6 mM IS $CaCl_2$ (up to 10 PV; stages i and ii).

[b] values obtained during transport in ultrapure water solution, after $CaCl_2$ (10-20 PV; stages iii and iv).

[c] R is > 1, likely due to low sample resolution.

Table 2.3. Calculated attachment efficiencies compared to data reported in previous studies.

Nanoparticles and Conditions	**Mobility (max. C/C_0 eluted)**	**Attachment Efficiency Value[a]**	**Source**
		This Study[b]	
CSA-240 in ultrapure water	~ 1.0	0.00	
CSA-240@Pd in ultrapure water	~ 1.0	0.05	
CSA-240 in $CaCO_3$	< 0.01	>2	
CSA-240@Pd in $CaCO_3$	< 0.005	>3	
CSA-240 in $CaCl_2$	< 0.01[c], 1.4[d]	> 3.[c], < 0[d]	
Cl tracer	~ 1.0	0.00	
		Previous Studies	
Hematite nano-rice	~ 0	Insufficient data	
500X100 nm			Alaskar et al. (2011)
PVP – hematite	0.095	Insufficient data	
PVP-nAG, natural soil	< 10	0.03-0.15	Cornelis et al. (2013)
PAA-nZVI, quartz sand	~ 0.7	0.2	
PAA-nZVI, carbonate sand	~ 0.2	1.2	Laumann et al. (2013)
PAA-nZVI, Ottawa sand	~ 0.6	0.36	
nZVI, Chargin soil	0.2	0.05	Schrick et al. (2004)
PAA-nZVI, Chargin soil	0.6	0.14	
CMC-nZVI, sand $\vec{v}$=0.018 cm s^{-1}	0.8	0.0019	
CMC-nZVI, sand $\vec{v} = 0.035$ cm s^{-1}	0.9	0.0023	He et al. (2009a)
CMC-nZVI, sand $\vec{v} = 0.071$ cm s^{-1}	1.0	0.0003	
Bare nZVI, Ottawa sand	< 0.1	0.43	Jiemvarangkul et al. (2011)
PVA-nZVI	> 0.95	0.0005	
PAA - nZnO, $NaNO_3$ < 1000 mM IS	1.0	< 0.13	Petosa et al. (2012)

Nanoparticles and Conditions	**Mobility (max. C/C_0 eluted)**	**Attachment Efficiency Value[a]**	**Source**
PAA - nZnO, 10 mM IS $CaCl_2$	~ 0.1	1.4	
Ferrihydrite (Fe_2O_3), 0.2 mm quartz sand, NaCl < 5 mM	1.0	~ 0.01	Tosco et al. (2012)
Fe_2O_3 , 0.2 mm quartz sand, 10 mM IS NaCl	0.55	~ 0.1	
Fe_2O_3, 0.07 mm diam. Quartz, 30 ppm PAA6K	~ 0.4	0.06	Xiang et al. (2013)
Fe_2O_3, 0.07 mm diam. Quartz, 500 ppm PAA6K	1.00	0	

[a] Values are either reported in studies or calculated from experimental conditions outlined.

[b] The CSA used in this study are coated with polyacrylamide.

[c] Values obtained during transport in 8.6 mM IS $CaCl_2$ (stages i and ii).

[d] Values obtained during transport in ultrapure water solution, after $CaCl_2$ (stages iii and iv).

Chapter 3
Influence of Size of Catalytic Superparamagnetic Iron Oxide Nanoparticles on Stability and Transport in Porous Media

To be submitted as journal publication by: Adam M. Lentz, Timothy Leshuk, David W. Blowes, Frank X. Gu, Carol J. Ptacek

3.1 Summary

Nanoparticles (NP) are used as catalysts for groundwater remediation because of their properties and that they can be injected into the subsurface. Catalytic and magnetically separable superparamagnetic iron oxide NP (SPION), of different sizes, were evaluated to assess the stability of aqueous suspensions and to evaluate the potential constraints on transport in porous media. Controlled SPION aggregates (CSA) can be coated with polyacrylamide to enhance transport, magnetically separated following use, and can be coated with Pd to enhance hydrogenation reaction rates via catalysis. Suspension tests under environmentally relevant ionic strengths of NaCl, $MgSO_4$, and $CaCO_3$ were evaluated using two methods: visual observations, and with continuous absorbance readings. In ultrapure water suspensions, CSA settled steadily over days, with the 340 nm diameter CSA showing the least stability and the 100 nm NP the greatest. Divalent ions and higher solute concentrations caused more settling than monovalent ions or lower solute concentrations. Complete settling was observed in $CaCO_3$ solutions at concentrations above 1.3 mM ionic strength (IS) and in $MgSO_4$ solutions with concentrations above 2 mM IS for 340 nm NP within 3 hr. Complete settling was not observed in 2 mM IS $MgSO_4$ solutions for 100 nm NP within 20 hr. Complete settling was observed in NaCl above 10 mM IS for 340 nm NP within 2 hr, yet not observed in 90 mM IS NaCl solutions for 100 nm NP after 40 hr. Transport through porous media was evaluated using a 15 cm long column packed with 0.07 mm mean diameter silica sand. Ultrapure water and $CaCO_3$ solutions were used to assess the effect

of the aqueous matrix on NP transport. All three NP sizes exhibited conservative transport in ultrapure water with similar breakthrough curves to Cl^-. In $CaCO_3$ solutions at 50 % and 10 % $CaCO_3$-saturation (5.1 and 1.3 mM IS) < 5 % elution of CSA was observed after 20 total pore volumes, including following decreased ionic strength and increased flow rate. Minimal detachment was observed following modifications to solute concentration and flow rate. Attachment efficiency values over 2 were observed, in all cases except for the smallest 100 nm NP where 85 % of the NP was eluted in 1.3 mM IS $CaCO_3$ solution. These results suggest that transport decreases as the size of CSA increases from 100 nm to 340 nm and as IS of the solution increases. Transport and recovery of the NP are also dependent on the groundwater velocity and aqueous solutes, especially dissolved $CaCO_3$. Transport is potentially viable in carbonate-free aquifers, but modifications to the NP properties are required for application to $CaCO_3$-bearing aquifers.

3.2 Introduction

Groundwater contamination by dissolved metals and halogenated hydrocarbons (*e.g.*, Cr(VI), trichloroethylene, etc.) is widespread and requires remediation. Conventional remediation techniques focused on pump-and-treat and excavation of source zones. More recent techniques include reactive injections and *in situ* permeable reactive barriers, such as zero-valent iron (e.g. Blowes et al., 2000). Most recently, nanoparticles (NP) have been proposed as a groundwater remediation tool due to their highly reactive surface-to-mass ratio and injectable size (EPA, 2008). Nano zero-valent iron (nZVI) has received the most attention as a viable NP for remediation (Tratnyek and Johnson, 2006; Yan et al., 2013). Palladium or other catalysts can be incorporated into nZVI to create bimetallic NP with increased reactivity (He and Zhao, 2005; Zhang and Elliot, 2006).

Transport studies, primarily using column experiments, have been conducted using nZVI (He et al., 2009a), and many other types of NP (Petosa et al., 2010). NP can be transported, attach (and not be transported), or detach (and resume transport). Attachment can be partly explained using colloidal filtration theory, CFT (Yao et al., 1971), including mechanisms of attachment due to diffusion, sedimentation, and interception. Attachment efficiencies (Tufenkji and Elimelech, 2004) developed from CFT have been used to quantify NP transport in column experiments (Petosa et al., 2010). Blocking and ripening, wedging, and straining are potential removal mechanisms not included in CFT. Detachment processes occur and are currently explainable with DLVO theory but not included within colloidal transport models (Bergandahl and Grasso, 2003). Breakthrough curves of NP column experiments can be simulated using one-dimensional models, such as the STANMOD CXTFIT 2.1 software package (Toride et al., 1999), based on the advection-dispersion equation in saturated homogeneous porous media (Freeze and Cherry, 1979).

Field applications of NP require knowledge of NP mobility in the subsurface. Iron-based NP have been shown to have minimal transport (Phenrat and Lowry, 2009); however, with the addition of polymer coatings, such as polyacrylamide (PAM) (Cirtiu et al., 2011), polyacrylic acid (PAA) (Petosa et al., 2013), and carboxymethyl cellulose

(Sakulchaicharoen et al., 2010), the NP have much higher mobility because of electrostatic repulsive forces between the NP and between the NP and porous media grains (Phenrat and Lowry, 2009). Field studies focused on nZVI with carboxymethyl cellulose coatings or emulsified nZVI (Kocur et al., 2014; Quinn et al., 2005) and have achieved only a few meters of transport.

Surface properties and the size of the NP, collector grain properties (size and charge) and aqueous geochemistry all influence NP transport. Limited research has been completed evaluating NP size. Colloids in suspension that are smaller will have higher aggregation rates due to higher frequency of collisions. Despite this higher rate, O'Carroll et al. (2013a) observed that smaller carbon nanotubes (CNT) were less mobile than larger ones. Hotze et al. (2010) and He et al. (2008) report smaller NP are more stable, and thus need higher solution cation charges to cause instability. Once NP aggregate they may behave more like colloids, which show different behavior (Stimson, 2008), because colloids are significantly larger and are excluded from certain pore spaces.

Superparamagnetic iron oxide nanoparticles (SPION) are the focus of attention in the medical fields (Gupta and Gupta, 2005; Rosen et al., 2012; Chan and Gu, 2013). These materials have also been studied in applications to petroleum imaging (Xue et al., 2014) and wastewater treatment (Nassar, 2012; Tang and Lo, 2013) due to their high sorption capacity. Minimal work has been done on injecting SPION *in situ* and using them as a remediation tool. Chapter 2 evaluated the stability and mobility of SPION, in the form of controlled SPION aggregates (CSA), in porous media but did not evaluate the size effect of the CSA. Transport was found to be highly dependent on aqueous $CaCO_3$ content. CSA are beneficial because they can be separated from solution using a magnetic field and catalysts can be incorporated onto the CSA surface to increase reactivity.

In the current study, CSA of multiple sizes were assessed for aqueous stability and mobility in porous media, especially in ultrapure water and $CaCO_3$-containing aquifers. Aqueous stability was assessed by completing suspension tests and observing a series of photographs as they settle and by continuous absorbance (A) readings to give a settling curve. Aqueous solutions varied by solute types and solute concentrations.

Mobility in porous media was assessed using a sand-packed glass column and injecting NP suspensions followed by NP-free inputs to monitor the breakthrough of NP.

3.3 Materials and Methods

The materials and methods used in this study were similar to those described in Chapter 2.

3.3.1 Nanoparticle Preparation and Characterization

Synthesis of controlled SPION aggregates was conducted at the University of Waterloo using the technique described in Chapter 2 which is similar to procedures described by Cheng et al. (2010) and Leshuk et al. (2013). Starting with $FeCl_3 \cdot H_2O$, the SPION were precipitated during a hydrothermal process in the presence of PAM in solution, which formed a surface coating. The size of the CSA was controlled by varying the concentration of the precipitating agent in the synthesis reaction. The CSA naming convention was based on the TEM-determined NP diameter.

After synthesis, the NP were characterized using transmission electron microscope images (TEM; Philips CM-10, 60 keV) and dynamic light scattering measurements (DLS; Brookhaven 90 Plus Particle Size Analyzer) to determine NP size. Zeta potential measurements (Malvern Zetasizer Nano ZS90) were conducted to determine surface charge using replication from 10-100 scans and the real and imaginary refractive indices. CSA concentrations were determined using samples within the linear range of constructed absorbance calibration curves. NP suspensions are turbid and scatter light as opposed to absorb light. A linear absorbance calibration curve was developed to provide measurements of NP concentrations from detection to 0.1 g L^{-1}.

3.3.2 Experimental Procedures

The CSA were probe sonicated prior to use. Suspension tests examined stability and degree of aggregation of the three different-sized NP in various concentrations of NaCl, MgSO4, and CaCO3 solutions. Episodic suspension tests (E-ST) were 15 mL of

suspensions prepared gravimetrically in glass bottles photographed over time. Continuous suspension tests (C-ST) were 25 mL suspensions left undisturbed in a 25 mL glass cuvette within a spectrophotometer and continuous absorbance readings were taken using a wavelength of 560 nm. Absorbance (A) is a measure of how much of an incident beam of light is absorbed by a sample.

Column experiments assessed mobility of NP through porous media by obtaining CSA BTC. Columns 15 cm long with 1 cm inner diameter (4.7 mL PV; Chromaflex column, Kontes) packed with 0.07 mm mean diameter Ottawa sand were used. The Ottawa sand was acid cleaned, rinsed to neutral pH, and dried at room temperature prior to packing. Flow through the column was achieved with a peristaltic pump (Ismatec) and Pharmed® pump tubing (Cole Parmer) in an upward direction. Input solutions were ultrapure water, 1.3 mM IS CaCO3, or 5.1 mM IS CaCO3 solutions. $CaCO_3$ solutions were prepared gravimetrically, with $CO_{2(g)}$ flux, and equilibration with the atmosphere. Samples were collected at the effluent end with an automatic fraction collector (Retriever 500, Teledyne ISCO). After many PV of background electrolyte solution, 5 PV of NP input was followed by 5 PV of NP-free input. NP input suspensions were maintained with agitation throughout the injection. Samples were analyzed via spectrophotometric methods (HACH 2800) for absorbance at a 562 nm wavelength to determine the relative NP concentration. In less-mobile column tests, a longer flushing sequence was completed with 5 PV of 4 stages: NP input, NP-free input, ultrapure water at the same flow rate, and ultrapure water input at a higher flow rate. Input solution pH was measured with an Orion ROSS pH combination electrode (Thermo Scientific) and SympHathy benchtop pH meter (VWR). pH values also were calculated with PHREEQCi assuming the solution was at equilibrium with atmospheric $CO_{2(g)}$.

Physical transport was assessed using a conservative tracer test was performed using a 250 mg L^{-1} Cl- (as NaCl) solution for 5 PV of flow followed by 5 PV of Cl-free input solution. Select samples were filtered with a 0.45 µm Supor® membrane filter and then analyzed by ion chromatography (IC) at the Department of Earth and Environmental Sciences, University of Waterloo. Calculations to further the BTC analysis were made, as well as computing attachment efficiency values and completing 1-D simulations.

3.4 Results and Discussion

3.4.1 Physical Characterization of Nanoparticles

Three separate batches of spherical CSA coated with PAM were synthesized. The CSA diameters, determined from TEM images, were 100, 240, and 340 nm (Figure 3.1). These particle sizes are incorporated into the names assigned to the three batches of CSAs: CSA-100, CSA-240, and CSA-340. Examination of the TEM images indicates that the CSA within each batch were spherical and uniform in size. As the size increases between batches, the surface apparently becomes smoother, resulting in a decreased surface area-to-volume ratio.

The DLS measurements (Figure A.2) indicated that CSA-100 had an effective diameter (defined as the maximum intensity peak obtained from a lognormal size distribution) of 211 nm, with the majority of the particles around 110 nm diameter (single particles) and a few between 430-500 nm (aggregated particles), with a polydispersity of 0.27. CSA-240 had an effective diameter of 275 nm with two modes of particles centered at 60 nm and 285 nm, with a polydispersity of 0.059. CSA-340 had an effective diameter of 425 nm with all detected NP centered on this diameter, with a polydispersity of 0.017. DLS measurements in various solutions show increased aggregation over time, in the presence of salt, and at lower positions in a suspension of NP (Appendix C).

Differences in particle size between the TEM and DLS techniques are attributed to variations in the extent of aggregation and to differences in measurement conditions (dry and wet). TEM measurements are conducted under a vacuum and in dry conditions, whereas the DLS measurements are conducted on a suspension.

CSA-240 and Pd-coated CSA-240 (CSA-240@Pd) have an average surface charge of -47.9 ± 6.2 mV and -45.3 ± 7.2 mV, respectively, within a range of -40 to -52 mV. The surface charge is likely derived from carboxylic acid groups developed during the synthesis process. Measurements presented in Chapter 2 indicated that the Pd-coating did not affect the surface charge and did not significantly alter the stability and transport of the CSA. However, Pd catalyzes reduction reactions and is required for reactivity

studies or for environmental remediation applications. The CSA can be separated from solution when exposed to a magnetic field.

3.4.2 Suspension Tests

3.4.2.1 Episodic Suspension Test (E-ST)

Photographs from episodic suspension tests (E-ST) show the stability of CSA-100 and CSA-340 at different suspension concentrations (Appendix D). Critical coagulation concentrations (CCC) are often cited (Chen and Elimelech, 2006). Beyond the critical coagulation concentration, quicker settling is not expected. Approximate critical coagulation concentration values (Chen and Elimelech, 2006), determined from preliminary experiments, were used as the maximum solute concentrations.

CSA-100 suspensions at > 0.2 g L^{-1} in ultrapure water remained relatively stable, with initial gravitational settling occurring slowly (initial settling between 48-72 hr) and incomplete settling after 25 days (Figure A.5). For CSA-100 at concentrations < 0.05 g L^{-1} NP in ultrapure water there was no visible settling, probably due to lower collision and aggregation rates (He et al., 2008). CSA-340 showed more rapid gravitational settling for all three NP concentrations, with almost complete settling after 48 hr (Figure A.5). With an initial NP concentration of 0.2 g L^{-1} of CSA-100 and CSA-340 residual NP remained in the supernatant following gravity settling. The remaining suspended NP were likely the smallest diameter NP.

The stability of the NP was significantly lower in monovalent NaCl solutions than in ultrapure water. Stability decreased with increasing NaCl concentration. With CSA-100 in 90 mM IS NaCl (Figure A.6), complete NP settling was observed within 3 hr. At a NaCl concentration of 40 mM IS, settling was incomplete past 3 weeks. For CSA-240, complete settling occurred between 2-6 hr in 10 mM IS NaCl, but only modest gravity settling occurred after 2 days in 2 mM IS. Complete settling of CSA-340 occurred rapidly at NaCl concentrations of 2 and $\geq$ 5 mM IS. The larger CSA settled more rapidly, also at low concentrations of NaCl.

DLS data were collected spatially and over time. Comparison of settling rates in suspensions of 0.2 g L^{-1} CSA-100 in ultrapure water and 0.2 g L^{-1} CSA-100 in 60 mM IS NaCl, show increases in settling rate associated with increases in effective particle diameter 1) over time, 2) near the base of the sample, and 3) with increased solute concentrations (Appendix C). Increased solute concentrations caused a wider distribution of particle sizes. Greater dispersivity has been observed to cause instability of NP suspensions (Hotze et al., 2010).

The NP were much less stable in divalent $MgSO_4$ suspensions (Figure A.7) than NaCl solutions. Rapid and complete settling was observed for CSA-100 in 8.1 mM IS $MgSO_4$ solutions. Settling was 50 % more rapidly in 16 mM IS $MgSO_4$ compared to 10 mM IS. No additional increases in the settling rate were observed in the 30 and 40 mM IS $MgSO_4$ solutions (photographs not shown). Settling rates of CSA-100 in 1.9 mM IS $MgSO_4$ were similar to those observed in ultrapure water and in low concentration NaCl solutions, with minimal settling after 200 hr. However, CSA-340 settled completely in the 1.9 mM IS $MgSO_4$ solution in under 3 hr.

Except for the smallest NP, CSA-100, in 1.3 mM IS $CaCO_3$, complete NP settling occurred in under 3 hr in all $CaCO_3$ containing solutions (Figure A.8), This rapid settling suggests that Ca ions and/or the increased pH from the carbonate-buffered solution cause destabilization of the NP suspension and aggregation of PAM-coated CSA. Increased aggregation is likely caused by the compression of the double layer, and thus higher aggregation due to particle-prticle collisions. Although the initial negative surface charge indicates that the NP suspensions should remain stable, variations in water chemistry resulted in potential changes in surface charge, and aggregation and settling occurred.

Comparing the settling rates for CSA-100 and CSA-340 to CSA-240, as reported in Chapter 2, indicate that the stability of NP within suspensions is size dependent. The stability of CSA-240 suspension was intermediate between the stability of 100 and 340 nm CSA, with smaller sizes being more stable. In ultrapure and NaCl solutions, CSA-100 remained suspended approximately 10x longer than CSA-240 and CSA-240@Pd, and longer compared to CSA-340. Phenrat and Lowry (2009) observed that aggregation of magnetic particles, leading to instability, is dependent on particle radii to the power of six. Thus, based on TEM-determined diameters, CSA-100 should be approximately 190x

and 1,540x more stable than CSA-240 and CSA-340, respectively. Results from E-ST indicate complete settling in ultrapure water would take ~1000, 100, and 20 hr for CSA-100, CSA-240, and CSA-340 suspensions, respectively. Based on these times, CSA-100 is expected to be 5 times and 50 times more stable than CSA-240 and CSA-340, respectively. These results are inconsistent with the settling relationship outlined by Phenrat and Lowry (2009).

Immediate settling was observed at 90 mM IS NaCl for CSA-100 and under 2 mM IS for CSA-340. In $MgSO_4$ solutions, immediate settling was observed in solutions containing 8.1 mM IS for CSA-100 and under 2 mM IS for CSA-340. In $CaCO_3$ solutions, immediate NP settling was observed under all conditions except CSA-100 NP in 1.3 mM IS. The immediate settling solute concentration decreased for higher-charged ions, specificallyfor $CaCO_3$. The largest NP, CSA-340, settled more extensively than CSA-240 and CSA-100 under similar or less concentrated salt levels This observation demonstrates the dependence of NP stability on ion type and ionic concentration (Lin et al., 2010).

3.4.2.2 Continuous Suspension Test (C-ST)

Strongly correlated linear calibration curves of absorbance *versus* NP concentration were obtained (Appendix E). NP remained stable in C-ST in ultrapure water (Figure 3.2a), with more extensive, gradual settling observed for larger NP sizes. In suspension tests using CSA-100 more rapid settling was observed in solutions containing higher concentrations of NaCl than were required for destabilization of CSA-240 and CSA-340. Long-term stability was observed in suspensions containing low NaCl concentrations (Figure 3.2b), with the settling rate dependent on CSA size: 40 mM IS NaCl with CSA-100, 5 mM IS NaCl in CSA-240, and 2 mM IS NaCl with CSA-340. For $MgSO_4$ solutions, long-term stability was observed only for CSA-100 up to 4.4 mM IS (Figure 3.2c). More rapid settling was observed in solutions containing $MgSO_4$ and $CaCO_3$. After $CaCO_3$ tests (Figure 3.2d), flakes of NP were observed at the bases of vials, which also indicates aggregation. Duplicate tests conducted on CSA-240

suspensions in 1.3 mM IS $CaCO_3$ solutions produced varied results, and were not included due to this lack of reproducibility.

The settling times for relative absorbance (A/A_0) to decrease to 0.9 and 0.5 were compared to provide quantitative measurements of suspension stability (Table 3.1). For the time period of the measurements, $A/A_0 = 0.9$ was not reached in ultrapure solutions. However, for CSA-100 0.5 A/A_0 was observed after 2 days. In NaCl solutions, 0.5 A/A_0 of CSA-100 at 60 mM IS was observed at 16 hr. Only 2 hr were required for 0.5 A/A_0 settling of CSA-240 at 10 mM IS and CSA-340 at 7 mM IS NaCl. For CSA-100, in 4.4 mM IS $MgSO_4$, 0.5 A/A_0 was not observed within one day. Settling of CSA-240 and CSA-340 to 0.5 A/A_0 was observed within 3 hrs. In solutions containing $CaCO_3$, settlings times were 0.2 to 1.5 hr for 10 % A loss and 2.4 to 4.0 hr for 0.5 A/A_0.

Comparing the C-ST suspensions with low concentrations of salts to suspensions in ultrapure water (Figure 3.3), increased relative absorbance early within the experiment occurred in low salt concentration solutions. This effect was observed with CSA-100 in 40 mM IS NaCl, and 1.9 and 4.4 mM IS $MgSO_4$ suspensions (although not with CSA-240 and CSA-240@Pd in Chapter 2). Early in the E-ST of CSA-100 in 1.9 mM IS $MgSO_4$, a darkening of the solution was observed. The increase in A could be due to: 1) increased particle size altering the scattering of light; 2) a gradual settling and accumulation of NP at the base of the cuvette in line with the light path; or, 3) the occurrence of Rayleigh scattering due to the wavelength of light being used and the particle size, resulting in less forward scattered light as particles aggregate over time. After A initially increased, A decreased slowly over time with settling.

Comparisons of C-ST and E-ST experiments indicate that similar results were observed using different experimental methods. Other studies evaluated the effect of surface coatings (Sakulchaicharoen et al., 2010), highly concentrated and viscous suspensions (Comba and Sethi, 2009), and the effect of Ca on suspension stability (Zhang et al, 2009). The NP size relationship to stability (Phenrat and Lowry, 2009) could not be compared to C-ST with high stability suspensions. The relationship did not hold for the three CSA batches with solutes present as the CCC was expected to be surpassed.

Suspension tests conducted were in static conditions. Compared to dynamic and flowing conditions in column tests and mobility through aquifers, NP will remain

suspended longer in dynamic systems under flow. Higher settling is likely to have occurred in E-ST and C-ST compared to flowing systems.

3.4.3 Column Experiments

Column tests including injection of 5 PV of NP suspension followed by 5 PV of NP-free input solution were completed (Figure 3.4). A Cl tracer test was conducted separately. The breakthrough of conservative tracer was monitored, and inverse modeling using the solute-transport model STANMOD (Toride et al., 1999) was used to determine solute transport parameters for the column experiments, and results were directly used for the NP tests. The pH of ultrapure water and NaCl solutions was 5.6, whereas an initial pH values for the $CaCO_3$ solutions were 6.4 for the 1.3 mM IS $CaCO_3$ solution, 6.3 for the 5.1 mM IS $CaCO_3$ solution, and 6.5 for 11.7 mM IS $CaCO_3$ solution. Calculated pH values for $CaCO_3$ solutions using PHREEQCi were higher (7.9 and 8.5) than measured values and ionic strengths were lower (1.3, 5.1, and 11.7 *versus* 1.5, 7.4, and 13.5) due to pH equilibrium and complexation.

Groundwater velocities of 5-10 m day^{-1}, typical of remediation projects that include groundwater pumping, were used for these experiments because the NP here are anticipated to be used in a groundwater injection system. This velocity range translates to a 6-13 mL hr^{-1} (1.5-3 PV hr^{-1}) volumetric flow rate through the column. A higher flow rate of 26 mL hr^{-1}, approximately 20 m day^{-1} (linear groundwater velocity) was used in some instances following experiments with minimal NP recovery.

Regardless of CSA size, CSA transport in ultrapure water resembled the breakthrough curves observed in the chloride tracer experiment, with full breakthrough observed (Figure A.13). Calculations based on effluent samples and the experimental parameters enabled determination of the percent of CSA to elute from the column (Table 3.2). Elution of chloride from the tracer test and of the injected NP was calculated at 1007 % and 100-107 %, respectively. However, in $CaCO_3$ solutions the extent of NP transport was dependent on the $CaCO_3$ concentration, with 85 % of the input NP concentration of CSA-100 eluted from the column at 1.3 mM IS $CaCO_3$, whereas

minimal transport, < 5 %, was observed at higher concentrations of $CaCO_3$ (Figure A.12). This observation demonstrates the importance of ionic strength and CSA size relating to transport.

A modified flush sequence of 20 total PV was completed for low transport cases, where < 5 % of the NP were eluted after the initial 10 PV, with four total stages: i) NP-introduction, ii) NP-free solution, iii) ultrapure water, and iv) ultrapure water at an increased flow rate (Figure 3.5). Decreasing the ionic strength and an altered flow regime can lead to detachment (Bergandahl and Grasso, 2003; Ryan and Elimelech, 1996). An increased flow rate would increase the force on NP to flow with the water and thus lead to decreased attachment or detachment. After decreasing IS and increasing the flow rate, an increase in the release of NP was observed for about 1 PV. Less than 1 % of the CSA introduced into the column was released for suspensions of CSA-100 in 11.7 mM IS $CaCO_3$, CSA-240 in 1.3 and 5.1 mM IS $CaCO_3$, and CSA-340 in 5.1 mM IS $CaCO_3$. Approximately 3 % of the CSA-340 suspended in the in 1.3 mM IS $CaCO_3$ solution was released. Relative to the release observed in a similar $CaCl_2$ test presented in Chapter 2, minimal detachment was observed in the column experiments conducted with the $CaCO_3$-containing solutions. For each NP size, the NP mobility decreased with increased $CaCO_3$ concentration (Table 3.1).

Several previous studies evaluated the effect of size on transport of NP in porous media. O'Carroll et al. (2013a) observed trends for transport of 10 to 40 nm diameter CNT that are the opposite of those observed here for 100-340 nm CSA in the current experiments. O'Carroll et al. suggest that the enhanced transport of larger CNT is due to fewer Brownian motion-caused collisions and the presence of fewer collector grain-retention sites. The 100-350 nm NP used in the current experiments seem to be affected by different retention mechanisms. Sun et al. (2015) observed the increase in size from aggregation of graphene oxide along the column length. For Fe-based NP, He et al. (2008) report that smaller NP are more stable and need a higher cation charge to cause instability. Aggregation of hematite NP (12-65 nm) increased with decreased NP size, increased NP suspension concentration, and increased ionic strength. Although aggregation increased with decreased size, this correlation is inconsistent with column breakthrough studies. Schrick et al. (2004) observed less extensive transport of 30-100

nm nZVI than for 400-500 nm nZVI optimized for transport and, thus, minimizing attachment. Zhuang et al. (2005) found decreased attachment of 20 nm to 100 nm latex microspheres in quartz porous media and increased attachment of 100 nm to 420 nm), indicating multiple mechanisms of retention occurred. Some transport studies indicate greater transport at larger NP sizes, which is contrary to the results observed in the current study. This difference may be due to complexities of mechanisms controlling attachment and detachment of the NP. The variations in transport behavior demonstrate the importance of precisely replicating conditions, such as NP size and type, NP concentration, and the aqueous geochemical environment, anticipated for field applications in laboratory investigations.

Although ultrapure water was used to initiate extensive transport of NP, ultrapure water may not be realistically applicable for widespread application, despite documented cases (Yang et al., 1996). However, the composition and concentrations of salts used for the stability tests and column experiments are consistent with aqueous environmental concentrations. Calcite, $CaCO_3$, is a common rock and component of groundwater. Ca and carbonate/bicarbonate have no drinking water limits (Health Canada, 2010). Halite, or NaCl, is a common soluble mineral. Chloride has an aesthetic objective (AO) less than 250 mg L^{-1} and Na, < 200 mg L^{-1} AO. Chloride often has a background level of 10 mg L^{-1} or less, but it is more concentrated in urban and industrial areas. $MgSO_4$ was used as it makes up common divalent natural species. Mg has no drinking water limit, but SO_4 has an AO < 500 mg L^{-1}. The concentrations of these solutes used in the experiments are within the AO limits.

From suspension tests and column experiments, smaller CSA are more stable and mobile. Smaller NP may yield fewer collector grain collisions, overcome gravitational forces more easily, and travel through smaller pore spaces. Thus altering the porous media grain size, and thus the pore sizes, will cause transport to behave differently than in this study, with less transport expected in finer porous media (Sun et al., 2015). Further complications arise with heterogeneous materials. These materials are a reality in field settings. Heterogeneities likely results in lower porosity, lead to smaller pores, and cause NP to be transported *via* more tortuous paths, all leading to more chances for NP to aggregate, strain, or attach, and not transport.

The porous medium material is also a factor. Quartz was used in this study. Quartz sand has a pH zero point of charge of around pH = 3. At higher pH, the surface charge of quartz would be negative and negatively charged NP would not easily attach to the surface. However, clays, carbonate sands, and iron oxide-coated mediums would be encountered, each with different surface charges affecting NP behaviour. Aggregation, and thus limited transport, was found to increase with pH (Lin et al., 2010).The selection of NP properties and surface charge is thus dependent on the specific aquifer material and application.

3.4.4 Reactive Solute Transport Model Simulations and Attachment Efficiency Equation of Column Results

Equilibrium solute transport models were fitted to experimental column data using 1-D CXTFIT 2.1 model with the STANMOD option (Figures 3.4 and 3.5) to yield fitted parameters of retardation (R) and relative NP input concentrations (C/C_0) (Table 3.2). The dispersion coefficient during the column experiment was determined to be 4 $cm^2\ hr^{-1}$ (dispersivity of 0.1 cm) by a chloride tracer test. The coefficient was used in the CSA transport simulations. Retardation of NP in ultrapure water in the column tests was observed at 0.87-0.97 and in $CaCO_3$ solution was observed at 0.92-0.50, decreasing with increasing $CaCO_3$ concentration.

The fitted input C/C_0 for ultrapure water column experiments was between 100-107 % and was much lower for column tests using $CaCO_3$ (Table 3.2). This correlated very well with the percent-eluted calculations (Table 3.2; R^2 =0.997 in a 1:1 linear relationship). During the 10 PV flushing sequence, following the 10 PV simulated sequence, a release of approximately equal magnitude of CSA was eluted from the column. Although CSA were immobilized in certain matrices, some CSA were always mobile in the aqueous phase.

Attachment efficiency (α) values were determined (Table 3.2) using the colloidal filtration theory (CFT) (Tufenkji and Elimelech, 2004; Yao et al., 1971) and values from relevant studies referenced in Chapter 2. Values of $\alpha = 0.00$ were obtained for ultrapure

water transport tests. In high and low $CaCO_3$ concentration environments, α was 0.03 and 1.15 for CSA-100, 2.5 and 3.1 for CSA-240, and 2.6 and 4.0 for CSA-340, respectively. Attachment efficiency values > 1 are not realistic based on the definition. Thus, values over 1 will be used as an indication of minimal transport. Values of α were found to increase with NP size. Interception is likely the mechanism included in CFT due to the relatively large size of the particles and the occurrence of aggregation (Yao et al., 1971). As attachment efficiency is theoretically limited from 0 to 1 based on CFT, mechanisms resulting in NP immobilization not accounted for in CFT, include straining, wedging, and/or ripening, all may have contributed to reduced NP transport.

The straining limit is expected to be insignificantbased on the TEM determined NP diameter and collector size (Bradford et al., 2002; Sakthivadivel et al., 1969). However, aggregation of NP used in this study occurred and thus straining may be a significant mechanism of attachment.

Transport distances for 1 % of the NP ca be quantified (Table 3.2) from column studies prior to introduction into the environment, where environmental fate becomes important. Transport distances showed considerable transport in ultrapure water (34 m or >500 m) but minimal in $CaCO_3$ solution (5.9 m or <0.25 m).

O'Carroll et al. (2013a) found that carbon nanotubes in 10 mM IS had less attachment for larger NP than smaller NP, with $\alpha = 0.09$ and 0.21 for 20-40 nm and 10-15 nm diameter CNT, respectively. The values of α were about four times less for 0.1 mM IS. Increased attachment with decreased size is opposite to that observed here with CSA in the 100-400 nm range. However, the particles are composed of different materials and in a different magnitude of size.

Results from this study found significant differences between the transport in ultrapure water and in $CaCO_3$ solutions. The most rapid settling occurred in $CaCO_3$ solutions. With minimal NP transport observed in $CaCO_3$ solutions (except for 100 nm or smaller CSA), recovery of NP following a subsurface injection of NP into $CaCO_3$-containing systems would not be viable. Rather, a zone of immobilized CSA may remain adjacent to the injection site. When the Pd catalyst is applied to the NP, limited increased reactivity will occur spatially only where the NP are present, and the expensive Pd will be lost.

Most column tests in the literature have included NaCl or $CaCl_2$ (Li et al., 2011: Shen et al., 2012). $CaCl_2$ caused full attachment and removal of NP from the elution followed by full detachment upon changing ionic strength and flow rates (Jaisi et al., 2008; Chapter 2 in this document). As $CaCO_3$ is a common groundwater component, significant transport in aquifer systems is unlikely with the CSA used here. Smaller CSA sizes could be utilized to achieve transport at low solute levels. However, after the concentration of total dissolved solids increases, the CSA will have to be modified to allow transport. Potential modifications are to use smaller sizes and to alter the surface properties.

Transport is different from reactivity. The CSA do not provide a reactive media, unlike nZVI. Field injections have shown the degradation of nZVI reactivity with time (He et al., 2010; Johnson et al., 2013). However, naturally occurring H_2 could provide long-term reaction media and the CSA@Pd could provide catalysis. Additionally, the remediation system could provide the reactant by making the organic coating on the CSA reactive (Bennett et al., 2010) or co-injecting nZVI. The use of CSA with catalytic properites would result in long-term increased reactivity over nZVI injections.

NP suspension concentration has not been thoroughly discussed in Chapter 2 and in this chapter. NP concentrations needed for field applications are reported around 10 g L^{-1}, higher than those used in this study, and likely cause lower stability at these higher NP concentrations (He et al., 2008). Esfahani et al. (2014) found lower normalized NP concentration breakthrough with higher NP input concentrations due to ripening, similar to results by Hosseini and Tosco (2013) at high NP concentrations. Thus, higher NP concentrations may yield even less transport.

3.5 Conclusions

CSA of different sizes (100, 240, and 340 nm *via* TEM images) coated with PAM were tested to evaluate their mobility in porous media and the potential for use of these NP in groundwater remediation. DLS measurements indicated that significant aggregation occurred, even in ultrapure water. The magnetically recoverable properties of the CSA allow for efficient recovery from groundwater. Addition of Pd catalysis would be needed for improved reactivity.

The effect of NP size and simplified aqueous environments were evaluated using suspension tests and column experiments. Suspension tests showed greater stability of smaller NP, at lower salt concentrations, and with monovalent *versus* divalent salts. Column experiments showed conservative behaviour of NP in non-ionic solutions but significant attachment and unrecoverable NP in $CaCO_3$ solutions. Less than 5 % of the CSA eluted from the column in $CaCO_3$ solutions, except for the smallest NP size at the lowest $CaCO_3$ concentration tested, where 80 % of the CSA eluted.

Simulations of column experiments yielded minimal retardation and fit the NP input concentrations with close agreement to calculated percent-eluted values. Discrepancies between observed and expected transport was observed for low transport cases because of higher variability in the data. Attachment efficiencies were calculated for the first 10 PV. For the ultrapure water test, α was 0. Attachment efficiency increased with CSA size from α of 0.03-1.2 for 100nm CSA and α of 2.6-4.0 for 340 nm CSA and increased with $CaCO_3$ concentration. Transport distances for tests done in $CaCO_3$ solutions are similar to transport observed in CMC coated nZVI field studies. Full transport and recovery is viable with CSA in environments similar to ultrapure water. Transport was not observed in $CaCO_3$-rich water. Therefore modifications are required to improve transport in $CaCO_3$-rich aquifers.

Testing more complex solution chemistry and field-realistic porous media heterogeneity may yield additional insights. For field applications, the controllable synthesis of the NP size is important, as higher stability and transport were achieved with 100 nm *versus* 240 nm CSA. Depending on the specific geochemistry of the water and

the remediation design, smaller NP (appropriate for flow-through and recovery) or larger NP (to form an *in situ* barrier) may be more appropriate.

3.6 Figures

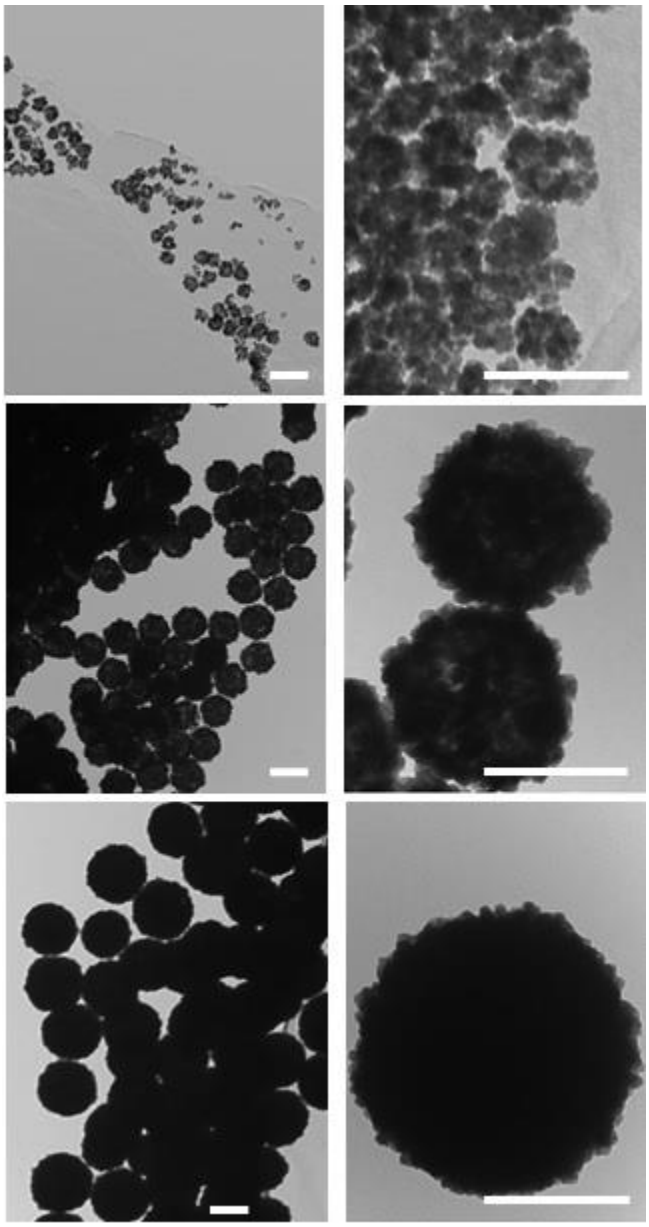

Figure 3.1. TEM images of CSA-100 (100 nm diameter), CSA-240 (240 nm diameter), and CSA-340 (340 nm diameter) from top to bottom, respectively. All scale bars are 200 nm.

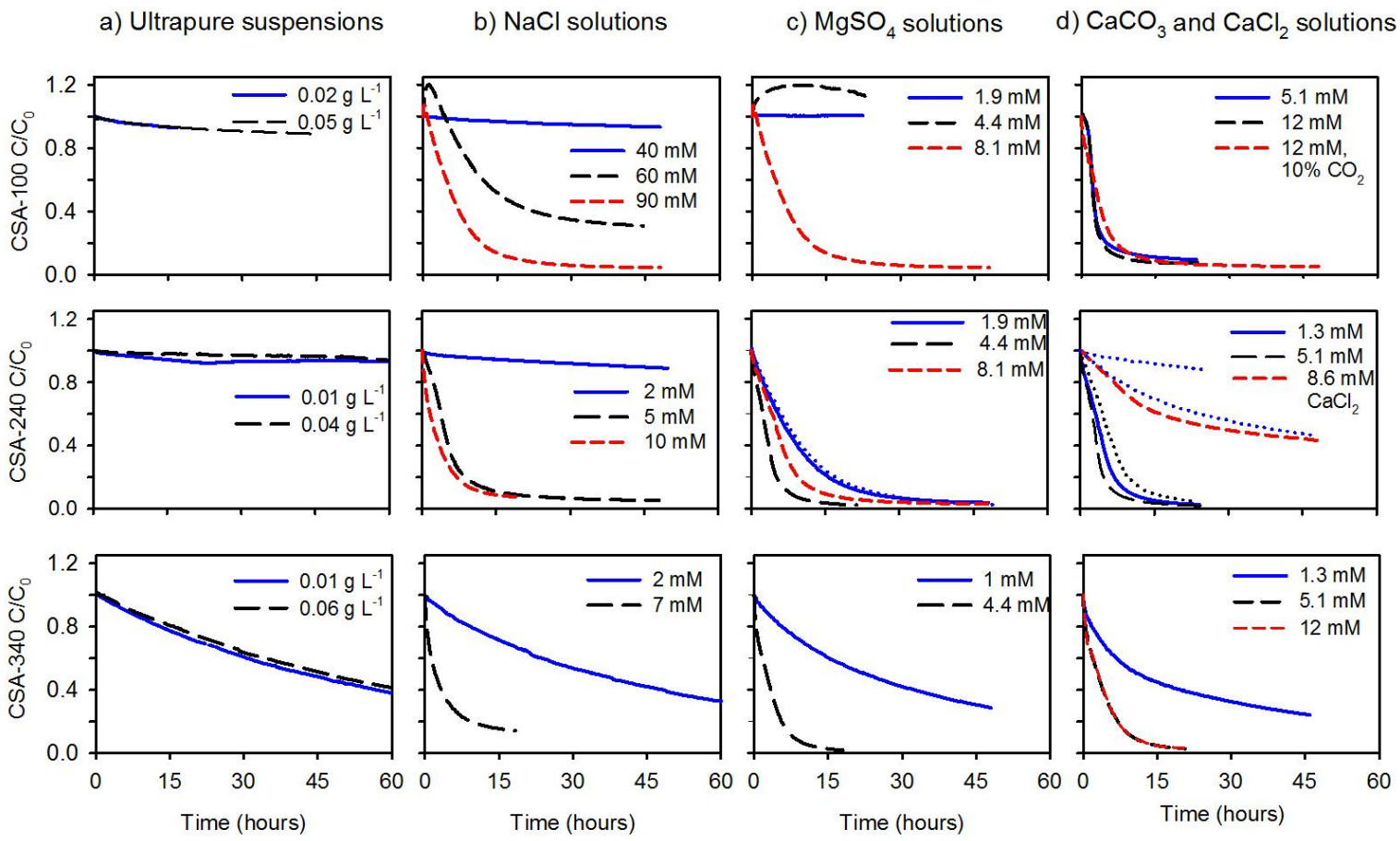

Figure 3.2. Continuous suspension test results in various salt solutions, CSA concentrations, and CSA sizes. The top set corresponds to CSA-100, middle to CSA-240, and bottom to CSA-340. CSA concentrations are 0.04 g L^{-1} (except for in ultrapure cases) and are normalized to a relative concentration of 1 at 0 hr. Left to right, environments are ionic strength of a) ultrapure suspensions, and b) NaCl, c) $MgSO_4$, and d) $CaCO_3$ or $CaCl_2$ solutions. Note: Duplicates (dotted lines) are not in legend; CSA-240 data is as seen in Chapter 2.

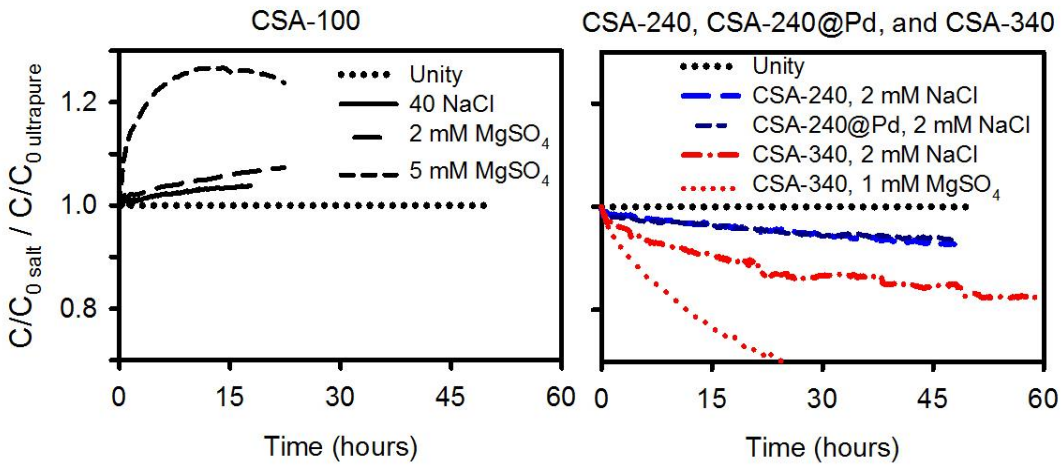

Figure 3.3. Curves of salt-containing C-ST relative to ultrapure C-ST suspensions over time. The relative absorbance over time of salt-containing C-ST was divided by the relative A for ultrapure suspensions. Note: size dependency, as CSA-100 rise above the unity and the other CSA drop below the unity line.

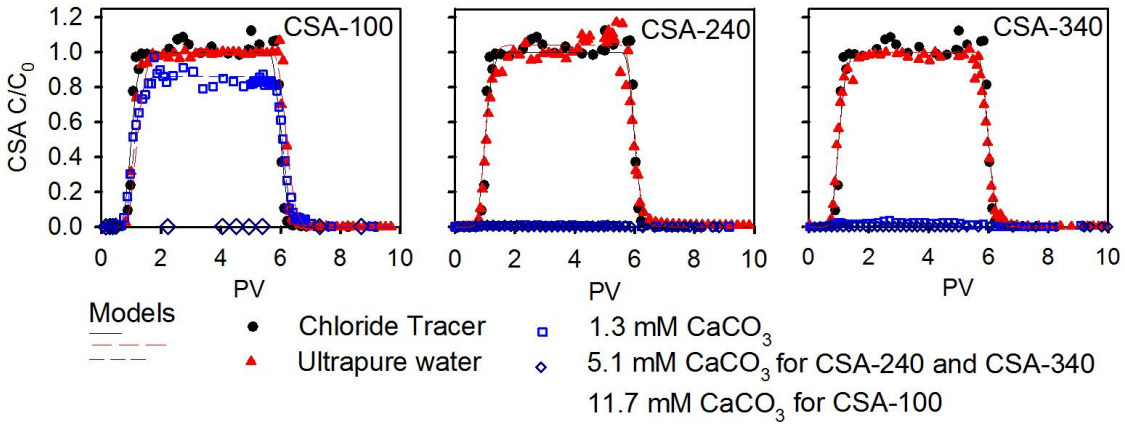

Figure 3.4. Column breakthrough curves of chloride (black circles), CSA in ultrapure water (filled triangles), 1.3 mM IS $CaCO_3$ (hollow blue squares) solution, CSA-240 and CSA-340 in 5.1 mM IS $CaCO_3$ (hollow dark-blue diamonds), and CSA-100 in 11.7 mM IS $CaCO_3$ (hollow dark-blue diamonds) solution, and model simulations (lines) as a function of pore volumes. Note: low mobility of CSA in $CaCO_3$ solutions (blue hollow symbols along the x-axis). See Figure 3-5 for expanded scales.

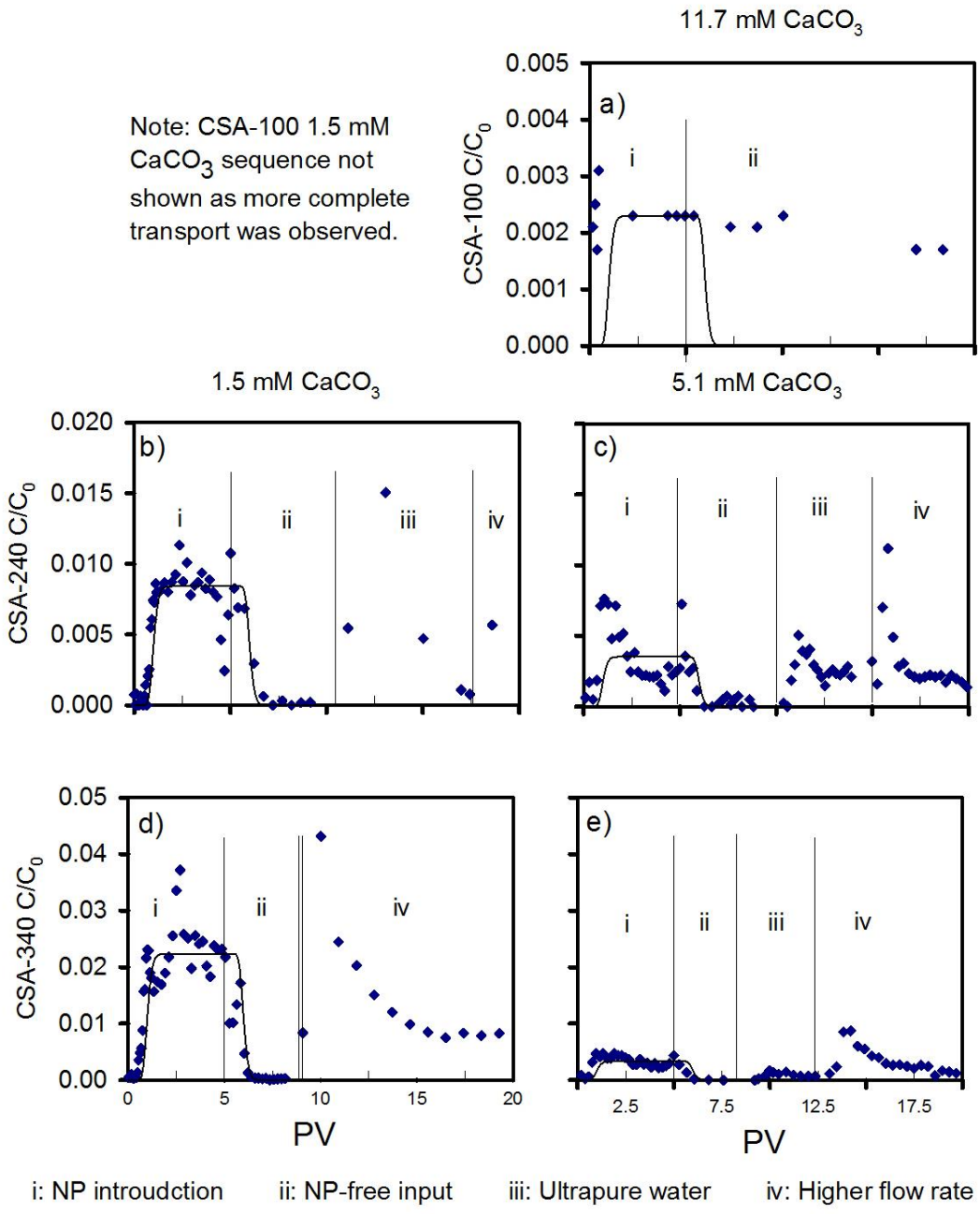

Figure 3.5. Relative concentrations of $CaCO_3$-containing breakthrough curves for a) CSA-100 in 11.7 mM IS, b) CSA-240 in 1.3 mM IS, c) CSA-240 in 5.1 mM IS, and d) CSA-340 in 1.3 mM IS, and e) CSA-340 in 11.7 mM IS in $CaCO_3$ solutions showing the entire column flush sequence of: i) CSA input, ii) CSA-free $CaCO_3$-containing solutions, iii) ultrapure input solution, and iv) ultrapure solution at a higher flow rate. Solid lines are model simulations fitting retardation and input concentration up to 10 PV. Note: The y-axis varying maximum values of 0.5, 2, and 5 % from top to bottom, respectively. Note: In a and d, the full sequence was not completed.

3.7 Tables

Table 3.1. Quantification of stability using time (hour) until 10 % and 50 % absorbance loss during continuous suspension test.

		Time (hr) to Reach Reported Relative Absorbance					
		CSA-100		**CSA-240**		**CSA-340**	
Solution Composition	**Solute Concentration**	**0.9**	**0.5**	**0.9**	**0.5**	**0.9**	**0.5**
Ultrapure (NP g L^{-1})	0.01-0.02	> 20	>> 70	>> 70	>>70	6.3	42.8
	0.04-0.05	36	>> 48	>70	>>70	7.5	47
NaCl (mM IS)	2.0	--	--	43	>>50	3.9	34.7
	7 (CSA-340) - 10.0 (CSA-240)	--	--	0.25	2.4	0.17	2.16
	40	> 48	>> 48	--	--	--	--
	60	5.8	15.9	--	--	--	--
$MgSO_4$ (mM IS)	1 (CSA-340) - 1.9 (CSA-240)	>> 25	>>25	1.2	7.6	2.3	22.7
	4.4	>> 25	>>25	0.35	3.0	<0.1	2.8
	8.1	2.9	4.8	--	--	--	--
$CaCO_3$ (mM IS)	1.3	--	--	0.45	4.0	--	--
	5.1	1.4	2.4	0.40	3.0	0.18	3.1
	11.7	1.5	2.4	--	--	0.18	3.1

Table 3.2. Transport parameters determined from column breakthrough curve data, using non-linear least squares fit (STANMOD), and from the attachment efficiency equation.

Column		% CSA Eluted (10 PV)	% CSA Eluted (all PV[a])	Fitted C/C_0	Fitted R from Mass Estimate Simulation	Attachment Efficiency	Transport Distance (m)
NP	**Salt Solution**						
	Ultrapure water	100	--	1.05	0.97	0.00	34
CSA-100	1.3 mM IS $CaCO_3$	89	--	0.85	0.92	0.03	5.9
	11.7 mM IS $CaCO_3$	< 0.1	< 0.1	0.002	0.50	1.15	0.15
	Ultrapure water	107	--	1.03	0.91	0.00	>500
CSA-240	1.3 mM IS $CaCO_3$	0.3	1.2	0.008	0.75	>2	0.15
	5.1 mM IS $CaCO_3$	0.3	0.6	0.004	0.60	>3	0.13
	Ultrapure water	100	--	0.97	0.87	0.01	34
CSA-340	1.3 mM IS $CaCO_3$	2.1	5.1	0.02	0.70	>2	0.18
	5.1 mM IS $CaCO_3$	0.2	0.5	0.002	0.58	>4	0.11
Chloride		107	--	1.11	1.10	0.00	

[a] Tests with > 80 % NP elution were not taken past 10 PV, and thus have the same elution value as for 10 PV.

Chapter 4
Transport of Palladium Nanoparticles: Laboratory and Synchrotron-based Microtomography Experiments

To be submitted as journal publication by: Adam M. Lentz, Mark Rivers, Timothy Leshuk, David W. Blowes, Frank X. Gu, Carol J. Ptacek

4.1 Summary

Nanoparticles (NP) are being used on an increasing basis for in situ groundwater remediation. Palladium NP (Pd-NP) can be used as a catalyst for remediation systems using naturally occurring H_2. The pore-scale transport of Pd-NP through silica grains was investigated using synchrotron-based microtomography. Suspension test experiments and conventional column transport studies were conducted to obtain data on the NP properties to accompany the tomography data. Pd-NP suspension tests yielded stable suspensions of over a week in ultrapure water, 1 M IS NaCl solution, and a $CaCO_3$ solution at near saturation conditions. Column tests yielded complete breakthrough of Pd-NP in ultrapure water and 1.3 mM IS $CaCO_3$ solution. In the microtomography studies, images obtained for one column experiment provided quantitative information on the transport of 4 g L^{-1} Pd-NP in aqueous solution relative to background aqueous concentrations. In another column experiment, five sequential tomographic images along the breakthrough curve yielded an increase in Pd content followed by a decrease throughout the column, consistent with expected results. The resolution of the images was not sufficiently high to observe individual NP or NP aggregates. Palladium concentration gradients were not observed along the column during NP introduction or flushing. The presence of silica grains increased the difficulty of processing images of Pd-NP transport in the column.

4.2 Introduction

The transport of nanoparticles (NP) in porous media has received great attention, in terms of transport in porous media relating to environmental fate (Petosa et al., 2010) and in situ remediation in porous aquifers (Tratnyek and Johnson, 2006). Nano zero-valent iron (nZVI) has received the most attention for in situ remediation (Bennett et al., 2010; Tratnyek and Johnson, 2006; Tosco et al., 2014); and has the potential to enhance reaction catalysis with the addition of metals such as Ni and Pd (He et al., 2009b). Palladium alone can also be used as a catalyst for reduction reactions in the presence of dissolved H_2 (Lowry and Reinhard, 1999). Nanoparticles used in consumer products can be vectors for contaminants and can pose concerns regarding their environmental fate (Klaine et al., 2008).

The transport of NP in porous media has been described at the macroscale using column test breakthrough curves (Petosa et al., 2010), interpretations with quantitative relationships (Tufenkji and Elimelech, 2004), and field-scale injections (Bennett et al., 2010; Kocur et al., 2014). These studies provide macro-scale measurements of NP elution at specified distances in laboratory studies or downgradient occurrences from injection wells in field studies. Microtomography, an imaging technique, allows for the direct determination of 3-D elemental concentration gradients and pore-scale quantification. This micro-scale imaging technique can provide information on pore-scale transport.

Synchrotron-based microtomography (SMT) is a powerful, non-destructive technique used to image 3-D volumes of samples with a monochromatic X-ray source (Wildenschild et al., 2005). Most other imaging techniques (computed tomography using medical X-ray instruments and scanning electron microscopes, SEM) obtain only two-dimensional images or are destructive, and require sample preparation. Magnetic resonance is used in column transport studies (Ramanan et al., 2012) but has poorer resolution and imaging time compared to synchrotron tomography. SMT provides images showing the micro-scale interrelation of pores and NP distribution. Collection of real-time in situ images of a column with flowing water can be acquired using sequential images in one experiment.

Tomography provides images by measuring X-ray attenuation through a sample, transforming the transmitted X-rays to visible light using a phosphor and then capturing the image with a camera. SMT distinguishes between elements based on X-ray absorbance (loss of intensity) values. Each phase, or component, within images can have a distinct elemental composition, resulting in image phase contrast.

SMT imaging of column experiments has shown transport of silver NP (Ag-NP) (Molnar et al., 2014). In the current study, the transport of Pd nanoparticles (Pd-NP) through porous media was studied. Pd K-shell electrons have a binding energy of 22.4 keV (K-edge). Provided sufficient transmission occurs through the sample, Pd can be detected at energies > 22.4 keV. Difference tomography, that is, using images obtained from the difference between the above- and below-absorption edge images, can be used to obtain the 3-D distribution of elements from two images above and below the elemental K-edge.

At the Advanced Photon Source (APS), Argonne, IL, the GeoSoilEnviro Center for Advanced Radiation Sources (GSECARS) SMT at beamline 13-BM-D has the capability to penetrate environmental samples under 1 cm diameter and to detect various phases in porous media samples (quartz, water, iron, and palladium). Previous studies completed at 13-BM-D in porous media include variably saturated studies (Wildenschild et al., 2005; Willson et al., 2012), investigations of biofilm distributions within pore networks (Iltis et al., 2011), non-aqueous phase liquid distributions (Culligan et al., 2006), and the fully-saturated Ag-NP transport study (Molnar et al., 2014).

In the current study, tomography mobility experiments were completed to evaluate the transport of Pd-NP within a saturated column containing silica sand, the first report dealing with these materials. In situ column breakthrough curves of Pd-NP in columns packed with silica grains were completed using SMT at beamline 13-BM-D to image the micro-scale pores and the NP and to assess the mobility of the NP relative to flowing water. To complement the micro-scale data, macro-scale suspension tests and column transport experiments were also completed. This chapter outlines the methods, the image processing completed, and the results of the tomography breakthrough curves.

4.3 Materials and Methods

4.3.1 Palladium Nanoparticle Preparation and Characterization

Synthesis of Pd-NP followed a previously published protocol (Teranishi and Miyake, 1998). Three solutions were mixed: 60 mL of 2 mM H_2PdCl_4, 100 mL of deionized water, and 40 mL of ethanol. Polyvinylpyrrolidone (PVP) was then dissolved (0.133 g) in the solution (PVP:Pd molar ratio of 10, based on the PVP monomeric unit) and refluxed for 3 hr to precipitate Pd-NP.

The NP were characterized with transmission electron microscopy (TEM), dynamic light scattering (DLS) measurements, and zeta potential measurements. TEM images were obtained from a Philips CM-10 TEM at 60 keV. TEM samples were prepared from drying a freshly probe-sonicated NP suspension subsample on a 400-mesh copper TEM grid with FormvarTM coating (Canemco). DLS measurements were made on low volumes of suspended samples (< 2 mL) in UV-range polymethyl methacrylate cuvettes (VWR) in a NanoBrook 90Plus Particle Size Analyzer (Brookhaven). Five-minute triplicate runs were made at 90 ° and a wavelength of 659.0 nm. Zeta potential measurements (Zetasizer Nano ZS90, Malvern) were made to obtain the average surface charge over a range of scans. A real refractive index of 2.160 and an imaginary refractive index of 1.201 (which deals with the attenuation) were used for both DLS and zeta potential measurements.

4.3.2 Laboratory Experiments

The Pd-NP suspension tests and column experiments were conducted using the approach previously described in Chapter 2. Aqueous solutions used are typical of environmentally relevant groundwaters. Continuous suspension tests (C-ST) were used to quantify the stability and settling of NP, and were carried out in a spectrophotometer using NP solutions in aqueous solutions containing NaCl and $CaCO_3$. Absorbance (A) was monitored continuously for indications of settling and related to NP concentration with a linear calibration curve. Column tests were conducted to determine the mobility

of the NP in a column 15 cm by 1 cm interior diameter, packed with 0.07 mm mean diameter air-dried Ottawa sand. The column tests consisted of 5 pore volumes (PV) of a 1 g L^{-1} NP suspension as the input solution, followed by 5 PV of an NP-free solution. Samples were collected via a fraction collector and analyzed using absorbance measurements. Correlation equations to calculate α, or attachment efficiencies (Tufenkji and Elimelech, 2004), and transport distances (Yao et al., 1971) were utilized to quantify the extent of NP attachment to collector grains. Column tests were interpreted using the STANMOD CXTFIT 2.1 software package to quantify retardation and mass of NP elution.

4.3.3 Tomography Experiments

Synchrotron-based microtomography was used to investigate the pore-scale transport of Pd-NP in porous media. In situ column breakthrough curves were monitored using SMT at the APS beamline 13-BM-D, following procedures similar to those reported by Molnar et al. (2014). The Pd-NP were synthesized, stored in aqueous solution, concentrated using a hot plate between 80-110 °C and then used at the APS.

Custom borosilicate glass columns crafted at the University of Waterloo Chemistry and Chemical Engineering glass blowing shop, with dimensions 3.6 mm interior diameter, 5.1 mm outside diameter, and 6 cm long, were used in the experimental work. The glass columns were pinched at the bottom to prevent loss of the porous media. The columns were held in the beam by a custom-made clamp (University of Waterloo Science Machine Shop) fastened onto the tomography stage (VP-25X Precision Compact Linear Stages, Newport). The porous media consisted of air-dried Ottawa sand that was acid cleaned with HCl overnight and rinsed with 18.2 Ω cm^{-1} ultrapure water (Milli-Q, EMD Millipore). The column was dry packed with the washed sand, sealed with glass wool at the bottom and top, flushed with $CO_{2(g)}$ and then saturated with ultrapure water. Saturated columns were prepared in advance of arrival at the beamline and placed into the sample holder.

The input solution was pumped through the columns at approximately 1 mL hr^{-1} (10 m day^{-1}). The NP concentration used was 4 g L^{-1}. Two separate column tests were run. The first column test (C1) was wet packed with a Pd-NP suspension and imaged prior to flow (0 PV) and subsequently, following NP elution, at 3 PV of flow. The second column test (C2) was imaged at specific intervals (I) of the NP breakthrough: I1) initially ultrapure water saturated before any NP introduction (0 PV), I2) with NP introduction advancing partially up the column (0.5 PV), I3) when the NP suspension had fully-saturated the column (1 PV), I4) after NP were eluted out of the bottom half of the column (1.5 PV), and I5) following complete NP-flushing from the column with ultrapure water (3 PV). Flow was suspended during image acquisition. Flow rate calculations and visual observations were used to determine when the NP within the column were at the desired position to suspend the flow and take the next image. Between each image, approximately 15 min was needed while the column was replaced for the next column or advanced for another image at the next interval. Effluent samples were collected while water was pumped through the column. The sample mass and A, with dilution if necessary, was measured.

4.3.4 Tomography Data Acquisition and Processing

At APS tomography imaging (Figure 4.1) was completed above and below the Pd K-edge energy (22.45 and 22.25 keV) at 0.25-1 hr imaging times. A Nikon CoolSNAP macro camera was used, with a field of view of 3.88 mm horizontal and 2.90 mm vertical, and with 1392x1392 pixels of resolution 2.79 μm. The tomography data was collected from 900 projections evenly spaced over a 180 ° rotation of the sample.

Preprocessing and reconstruction of the projections was completed with software developed specifically for application at GSECARS (Rivers, 2014), using IDL 8.2 (Exelis Visual Information Systems). Preprocessing with reconstruction corrects for dark current and the flat field, and converts two-dimensional projections into a 3-D image using filtered back projection algorithms. Each voxel (a 3-D pixel; dimensions of a pixel) contains an X-ray mass-linear attenuation value. Visualization and further processing

was completed using ImageJ and using vol_tools (Rivers and Gualda, 2009). One of those tools, vol_diff_shift software best aligns separate reconstructed images taken above and below the Pd K-edge. Vol_diff_shift also computes 16-bit difference volumes (D_I) from the reconstructed image above the Pd K-edge (I $i_{22.45}$) minus the reconstructed image below the Pd K-edge (I $i_{22.25}$):

$$D_{I\,i} = I\,i_{22.45} - I\,i_{22.25}$$

Using ImageJ, the above-K-edge reconstructed image and difference volume were then cropped to eliminate the column walls and air beyond the column. Initially, discrete measurements of representative greyscale values (GSV) of silica and the aqueous phase from select slices (approximately evenly spaced along the column) were used to obtain average pixel values for a slice. However, a more rigorous analysis was needed to obtain values for all pixels and each slice.

Further analysis was completed by segmenting the reconstructed image to create an 8-bit segmented volume ($S_{I\,i}$). The segmented volume allowed for determination of the porosity of each slice by analyzing the area of the silica grains. The product of each 8-bit segmented volume, one for the silica and one for the aqueous phase, and the 16-bit difference volume produced two 32-bit volumes, one for the silica and one for the aqueous phase ($P_{I\,i}$):

$$P_{I\,i} = S_{I\,i} \times D_{I\,i}$$

Automated programming allowed for the average GSV of each slice to be calculated. The slice average GSV was determined for both silica and aqueous phases. Weighting by the area of each phase (θ for the aqueous phase and 1-θ for the silica phase) for each slice was required to obtain the weighted phase average ($WP_{aq.}$ and $WP_{sil.}$):

$$WP_{I\,i_{aq.}} = {P_{Ii_{aq.}}}/{\theta} \qquad WP_{I\,i_{sil.}} = {P_{Ii_{sil.}}}/{(1 - \theta)}$$

4.4 Results and Discussion

4.4.1 Characterization of Nanoparticles

TEM images of Pd-NP show a bimodal distribution of NP sizes: free-NP (mean size of 28 nm) and aggregates of NP (mean size of 90 nm, representing three to four NP in diameter) (Figure 4.2). Compared to the CSA in Chapters 2 and 3, the Pd-NP are much more dispersed in size. The aggregates likely formed during synthesis from the monomer free-NP. Aggregates might also have broken up during sonication in preparation for TEM sample preparation.

An effective mean diameter of 109 nm with a polydispersivity of 0.31 was determined from triplicate DLS measurements (Table A.2). The lognormal size distribution was centered on 28 nm, while the multimodal size distribution had one peak from 89-93 nm.

From zeta potential measurements, the surface charge was -10.5 $\pm$ 4.7 mV, a magnitude range that is not typically sufficient to cause electrostatic stability. Instead, the high observed stability is likely related to steric repulsion due to the addition of PVP and the small NP size. Pd-NP suspensions remained unchanged between synthesis and experimental use based on visual and DLS observations, suggesting relatively constant size distribution over time.

4.4.2 Laboratory Experimental Results

4.4.2.1 Continuous Suspension Tests (C-ST)

C-ST results (Figure 4.3) after a month in either NaCl (0.01 M IS to 1 M IS) or $CaCO_3$ solutions up to saturation indicated the suspensions remained stable, consistent with visual observations. Over 5 days, an increase in A occurred rather than the expected decrease in A due to settling. Increased A may indicate either particle size change or an accumulation of NP near the bottom of the cuvette at the height of the light source. Unlike in C-ST from Chapters 2 and 3, times till relative absorbance decreased to 0.9

were past the week timeframe of the test. Minor settling may have occurred but not to a sufficient degree to observe visually.

4.4.2.2 Column Experimental Results

A breakthrough curve (Figure 4.4) for a conservative chloride tracer test was conducted to determine column transport characteristics and to compare the NP transport to the conservative tracer. For Pd-NP transport tests, based on sample mass and A measurements, mass balance calculations for the NP were made, which compared the mass of NP eluted to the input mass. The mass balance calculations for the Pd-NP indicated nearly complete elution (99.8 and 99.9 %) of the input mass of NP for experiments with ultrapure water and 1.3 mM IS $CaCO_3$ solution, respectively (tracer was 107 %). Full elution of NP suggests minimal aggregation and attachment of Pd-NP, even in the presence of Ca ions. Full transport in $CaCO_3$ solutions is different from the results of other column tests with CSA using similar columns and input solutions (Chapters 2 and 3). In addition, even though the zeta potential measurements indicated near-zero surface charge, which suggests poor stability, conservative transport of Pd-NP was observed. The main suggested reason for higher stability of Pd-NP relative to CSA is due to the smaller NP size and he absence of aggregation.

STANMOD CXTFIT simulations (Toride et al., 1999) were used to estimate relative NP initial concentrations and retardation coefficients from the data. A retardation coefficient of 1.10 was determined from the Cl tracer test. Retardation coefficients of 1.03-1.05 were determined for Pd-NP column tests, more similar to the conservative value of 1.00 than for the Cl tracer test. The initial NP relative concentration was estimated at 1.02-1.04 (Cl tracer test of 1.07). The 10 % deviation of retardation coefficient from ideality for the Cl tracer test could be due to poor sampling resolution, due to the high volume of solution required for sample analysis and the corresponding small PV of the column relative to sample volume, required to optimize transport calculations.

Calculated attachment efficiencies of 0.00 indicate that attachment did not occur for non-tomography breakthrough curves of Pd-NP in ultrapure water and 1.3 mM IS $CaCO_3$ solutions. Based on these results, nearly conservative transport of PVP-coated Pd-NP in $CaCO_3$ environments was attained, yet not for CSA.

Transport distances indicated similar trends as attachment efficiency, with high transport. Column tests indicated transport 34 m in ultrapure water and >1000 m in 1.3 mM IS $CaCO_3$ solution. The transport was full in both cases, and differences in transport presented are likely due to experimental error. Considerable care will be needed to contain or recover the NP were a specific remediation project.

4.4.3 Tomography Results

Tomography provides a quantification tool for small scale column studies. Breakthrough curves similar to those generated in larger scale columns (section 4.4.2.2) were obtained with tomography. However, additional information about the pore structure and NP dependency with position along the column can be obtained. Under conditions leading to attachment, the region of interaction between NP and collector could also be identified and retention mechanisms could be potentially resolved. Tomography imaging additionally can provide information on the porous media: grain size, roughness, and roundness. These properties may affect particle transport and can be incorporated into certain transport models.

An ultrapure water input solution was used for tomography column studies to minimize the effect of electrolytes on NP transport. The mobility of NP was evaluated under these conditions prior to the onset of the tomography experiments to ensure mobility could be achieved. A NP suspension of 4 g L^{-1} was used to provide a NP concentration sufficient for detection. The flow rate through the columns (approximately 1 mL hr^{-1}), representing a mean velocity of 10 m day^{-1}, is typical of groundwater flow under conditions representative of pumping for remediation. Slower groundwater velocities, representative of natural-gradient field conditions, could not

easily be achieved due to the small inner diameter of the column and the peristaltic pump used.

The tomography columns were sampled for relative NP input concentration breakthrough but the sample volume was too small to quantify. 1-D models were not completed for the same reason.

The projections obtained at the beamline were preprocessed and reconstructed using GSECARS tomography-specific software. The reconstructed images (Figure 4.5a) were cropped and segmented using ImageJ software to eliminate the column materials and the air outside the column to obtain a representative volume down the middle of the column and to partition the phases (Figure 4.5b). The aqueous segmented volume ($S_{I\,i_{aq.}}$) and the silica segmented volume (Figure 4.5b, top and bottom, respectively) illustarte an intermediate step in quantifying tomography data. From the difference between the above and below Pd K-edge energy images (Figure 4.5c), values for the average X-ray attenuation of select slices were determined for both the aqueous and silica phases (Figure 4.6). The attenuation value for each aqueous voxel was obtained by computing the product (Figure 4.5d) of the cropped aqueous segmentation (Figure 4.5b) and the cropped difference volume (Figure 4.5c). The silica phase attenuation values were obtained using the same approach (Figure 4.5d).

A porosity profile curve was obtained using the *analyzing particles* feature in ImageJ from the cropped segmented volumes (Figure 4.8a). Phase-specific GSV profiles curves were determined using an automated program to obtain each slice average GSV for the aqueous (Figures 4.7b and 4.8b) and silica phases (Figures 4.7d and 4.8d), separately for all slices (continuous). The blank-corrected aqueous phase GSV (Ii – I1) relative to the aqueous phase GSV of the input concentations (assumed to be I3 - I1) was obtained from the ratio of the two differences (Figure 4.8c) using:

$$\left(D_{I\,i_{aq.}} - D_{I\,1_{aq.}}\right) \Big/ \left(D_{I\,3_{aq.}} - D_{I\,1_{aq.}}\right)$$

Porosity for each slice varied between 0.20-0.55 (Figure 4.8a). This range, or heterogeneity, arises from the scale of the column being below the representative elementary volume, some slices have more or less void space. For C1, the porosities do

not entirely match due to unintended movements of the column between images, resulting in an approximately 60 slice (0.17 mm) shift. Also, some maxima and minima values of porosities observed in the 0 PV image were not resolved in the 3 PV image. In C2, slight shifts caused the column in I3 to be shifted by 11 slices and the column in I4 and I5 to be offset by 40 slices (0.03 and 0.12 mm), respectively, due to adjustments between images. These profiles were realigned to account for the shifts. Porosity provides a good indicator of alignment from image to image and was used to make alignment corrections.

For C1, the aqueous phase attenuation dropped dramatically between the 0 PV and the 3 PV images after flushing the NP-saturated solution from the column (Figures 4.6a and 4.7b). Silica phase GSV showed limited differences from image to image (Figure 4.7c). A linear correlation ($R^2 = 0.2$) between aqueous GSV and porosity can be seen visually (Figure 4.7a and b, but not in Figure 4.8a and b). Linear correlation of the hand-calculated slice average GSV of the aqueous phase to the computed complete slice showed a $R^2 = 0.91$ without outliers with a y-intercept = 0. The silica phase showed weaker linear correlation ($R^2 = 0.28$) of the hand-calculated slice average GSV to the computed complete slice average GSV.

For C2, the aqueous phase of the initial image before NP introduction (I1) showed the least attenuation (Figure 4.6 b and 4.8b). As the Pd-NP front was introduced partially through the column (I2), a slight increase of attenuation was observed. Upon full NP breakthrough in I3, the greatest attenuation was observed. The attenuation then decreased with partial elution and full elution (I4 and I5, respectively). Aqueous attenuation (Figure 4.8b) showed a slice-dependent variability along the column that was consistent between images. The silica phase images were consistent from image to image (Figure 4.8c). Because I5 after the NP flush had higher attenuation than I1, Pd-NP may have been retained within the column, though not visually evident.

Comparing the attenuation in I5 following NP elution relative to I1 before NP introduction to the attenuation of the NP saturated image relative to the initial image (I3/I1), an estimate of Pd-NP retained within the column can be made (Table 4.1). Based on the ratio I4/I1 and I3/I1, a 30 % increase in attenuation occurred between I1 and I5. The same ratio but determined between I5/I1 and I3/I3 had a 21 % increase. The

increased attenuation of I5 relative to I1 may indicate that 20 % of the NP were retained within the column, despite the lack of visual evidence of retention.

Comparisons were made between each image as whole (Table 4.1). Porosity and silica GSV showed consistent values among all images. Aqueous phase GSV of NP-saturated images increased with absolute certainty above that of the NP-free aqueous phase, despite the lack of observed NP during the partial introduction and flush (I2 and I4) images.

Linear correlations of the discrete versus continuous slice attenuation values for the aqueous phase (Figure 4.9a) are much stronger than for the silica phase (Figure 4.9b). For aqueous phase, which is where the NP reside, discrete measurements of select slices and select regions are appropriate to provide representative quantification.

Imaging limitations can occur due to unavoidable image artifacts (i.e., undesirable changes to a digital image), diffusion of NP due to NP concentration gradients during imaging time, and variant attenuation values at the top and bottom relative to the centre of the sample due to variable X-ray intensity. The total number of voxels is also important as it relates to the confidence interval (Molnar et al., 2014). In this study, attenuation values of the top and bottom slices were observed to deviate from the trend of the remaining slices. Based on the uninterpreted top and bottom slices, the top and bottom 1 % of slices (20 slices total) could be removed to statistically improve the data interpretation.

Improvements in image contrast could improve image processing. A heavier element in the aqueous phase would provide this contrast. Iodide is typically used for phase contrast (Wildenschild et al., 2002). However, iodide may drown out the signal produced by the Pd-NP and lower Pd-NP detection.

4.5 Conclusions

In this study, pore-scale transport of Pd-NP through silica grains was studied using synchrotron-based microtomography. Tomography, a non-destructive 3-D micro-scale imaging tool, provided sequential images and pore-scale quantification of NP transport as a function of time.

Tomography studies to evaluate micro-scale transport within narrow diameter columns were accompanied with suspension tests to assess aqueous stability and conventional column transport tests. Laboratory continuous suspension tests conducted using a spectrophotometer showed minimal decreases in A, or settling of Pd-NP. For groundwater remediation applications, these NP could remain suspended and likely unchanged for time periods needed for short-term remediation applications. Column tests showed unretarded transport of NP in ultrapure and $CaCO_3$ matrices. Calculated attachment efficiencies were 0.00, representing minimal attachment, for both conventional column experiments. These experiments highlight that the Pd-NP appear to be mobile at ionic strengths representative of those observed under environmental conditions.

Three-dimensional SMT data were obtained for one column at two snapshots in time. In a second column, five 3-D images were captured as the NP front progressed through the column. Using beamline-specific software and ImageJ, the raw images were processed, providing determinations of porosity, and aqueous and silica greyscale values.

The results of column tests showed a significant dependence of attenuation and pixel value on Pd-NP concentration. Consistent porosity trends were observed along the column, which served as a good indicator that images were aligned from one to another. Silica phase average pixel values remained constant among the five images. Aqueous phase pixel values increased with NP introduction and decreased upon removing NP from the column. Segmentation and differentiating phase boundaries proved difficult with silica grains as the phase boundaries were less defined and the geometry more heterogeneous.

The experiments showed that synchrotron-based microtomography studies of NP transport using silica grain as a porous medium are feasible, and that the use of Pd as the

NP material is viable. The high mobility observed suggests that near-complete transport and recovery may be obtained following injection and recovery operations, even in $CaCO_3$ systems. Together with the high mobility and the potential catalysis properties for groundwater remediation reactions of the Pd-NP used here, these NP seem a viable material for transport (but not cost) for *in situ* remediation projects.

This chapter demonstrates the potential application of using synchrotron-based microtomography to quantify catalytic Pd-NP transport experiments in silica grain porous media and satisfies the third overall objective of this thesis. Further, Pd can be detected in environmentally relevant samples. With full transport and recovery of the Pd-NP achieved and the catalytic properties of Pd, application of Pd-NP for *in situ* groundwater remediation might be feasible.

4.6 Figures

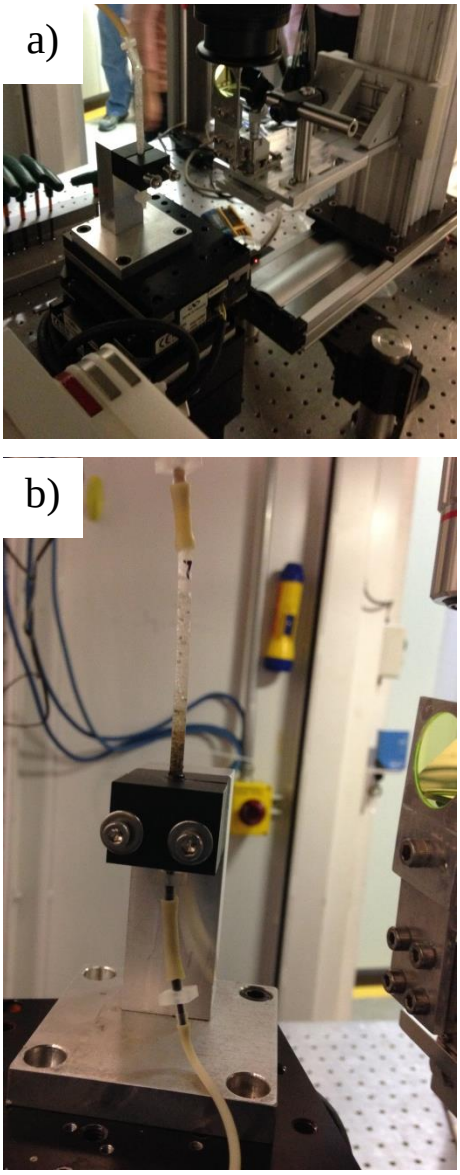

Figure 4.1. Experimental setup in the beamline 13-BM-D at the APS synchrotron facility hutch with a) a column setup within the X-ray beam path and b) NP being introduced into the column from the bottom.

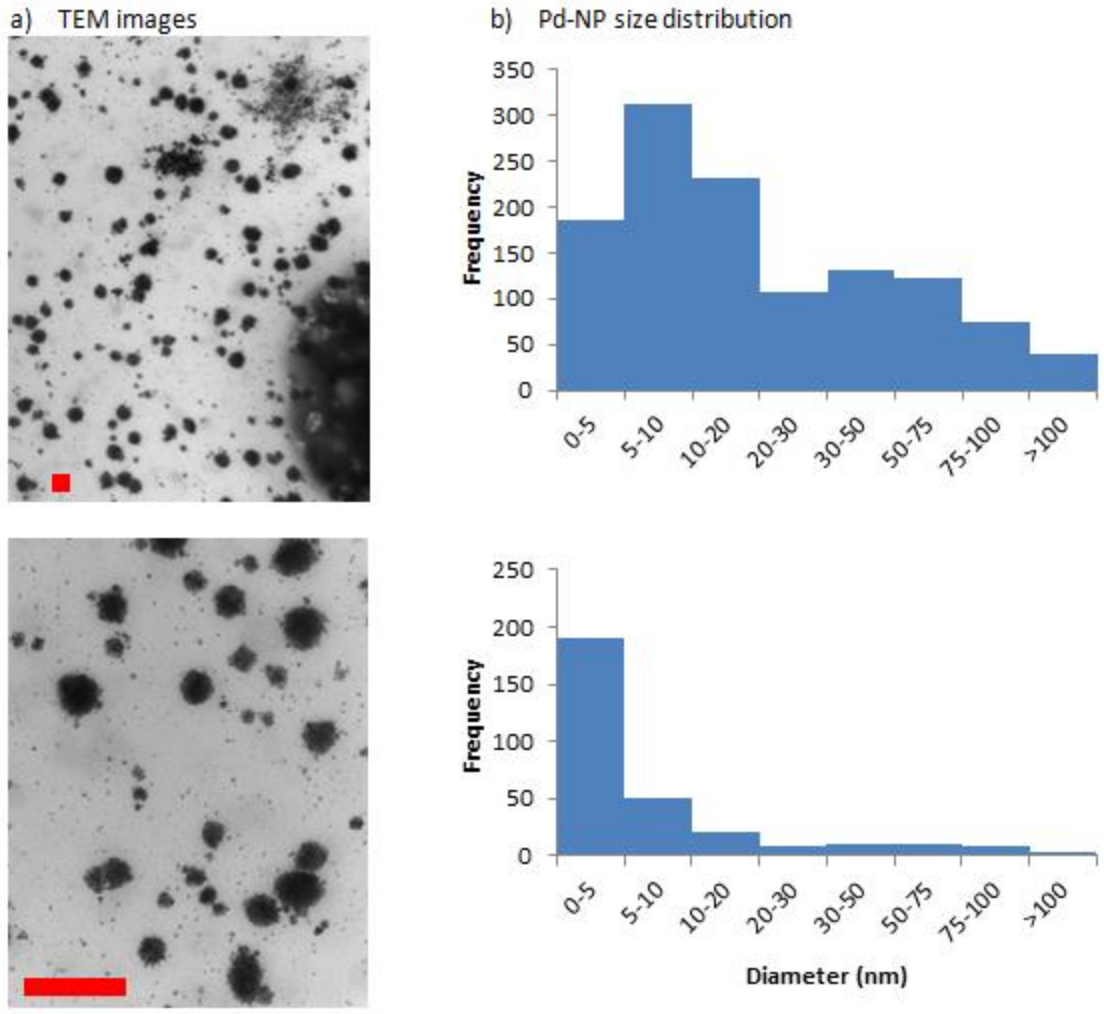

Figure 4.2. a) TEM images of Pd-NP showing a bimodal distribution of NP sizes. The TEM scale bar (lower left) is 250 nm in each image. (The bottom image is 5.5 times more magnified.) b) NP size distribution analysis obtained from TEM images.

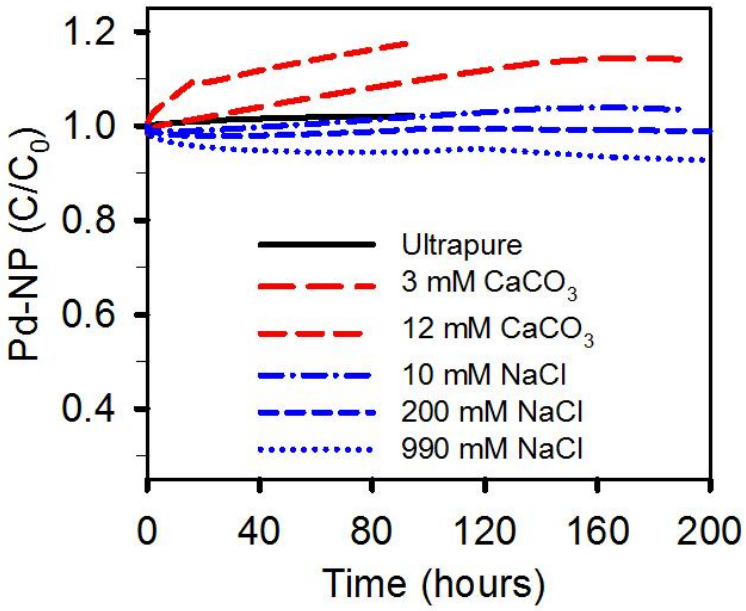

Figure 4.3. Continuous suspension test curves for 0.04 g L^{-1} Pd-NP suspensions (normalized to a relative absorbance of 1 at 0 hr) in different IS electrolyte solutions.

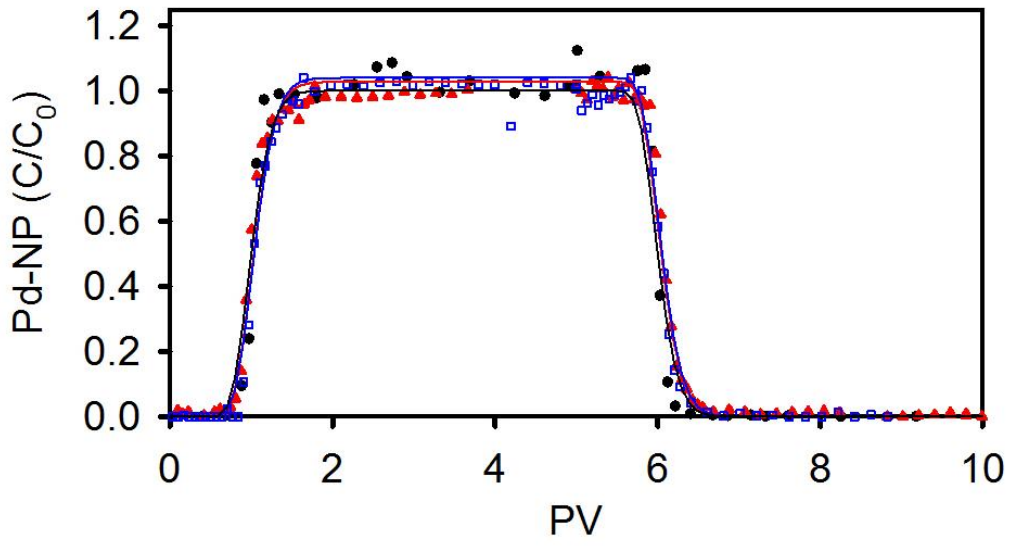

Figure 4.4. Breakthrough curves obtained from laboratory column tests showing relative concentrations of chloride (black circles), Pd-NP in ultrapure water (red triangles) and 1.3 mM IS $CaCO_3$ solution (hollow blue squares), and simulations (lines) as a function of number of pore volumes (PV).

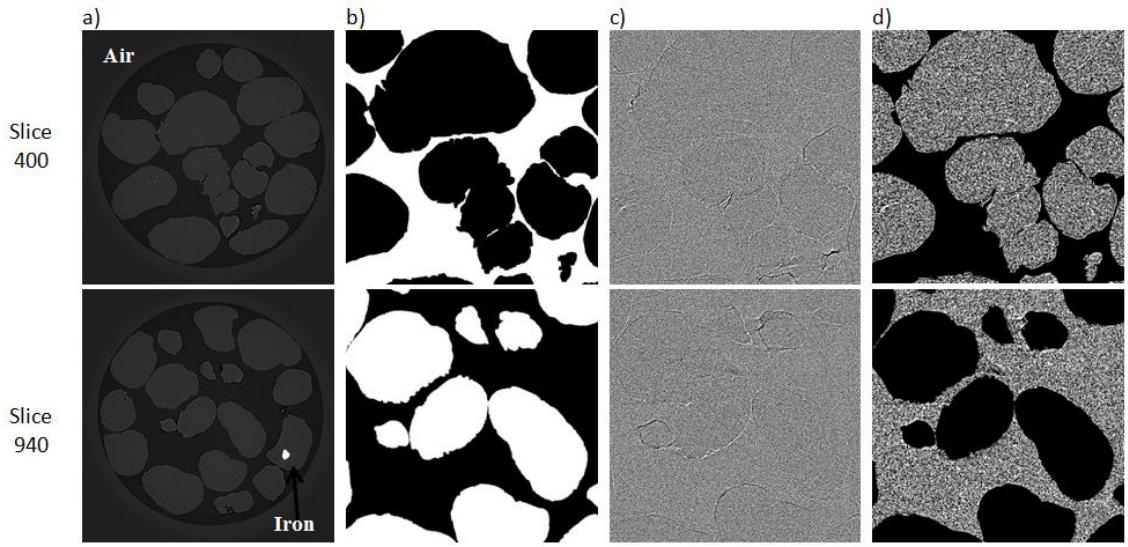

Figure 4.5. Stages of processing reconstructed image data to yield quantitative data for representative slice 400 from silica phase (top row) and slice 940 from aqueous phase (bottom row) from C2: a) reconstructed image, b) cropped aqueous segmentation volume, c) cropped difference volume, and d) product of b and c.

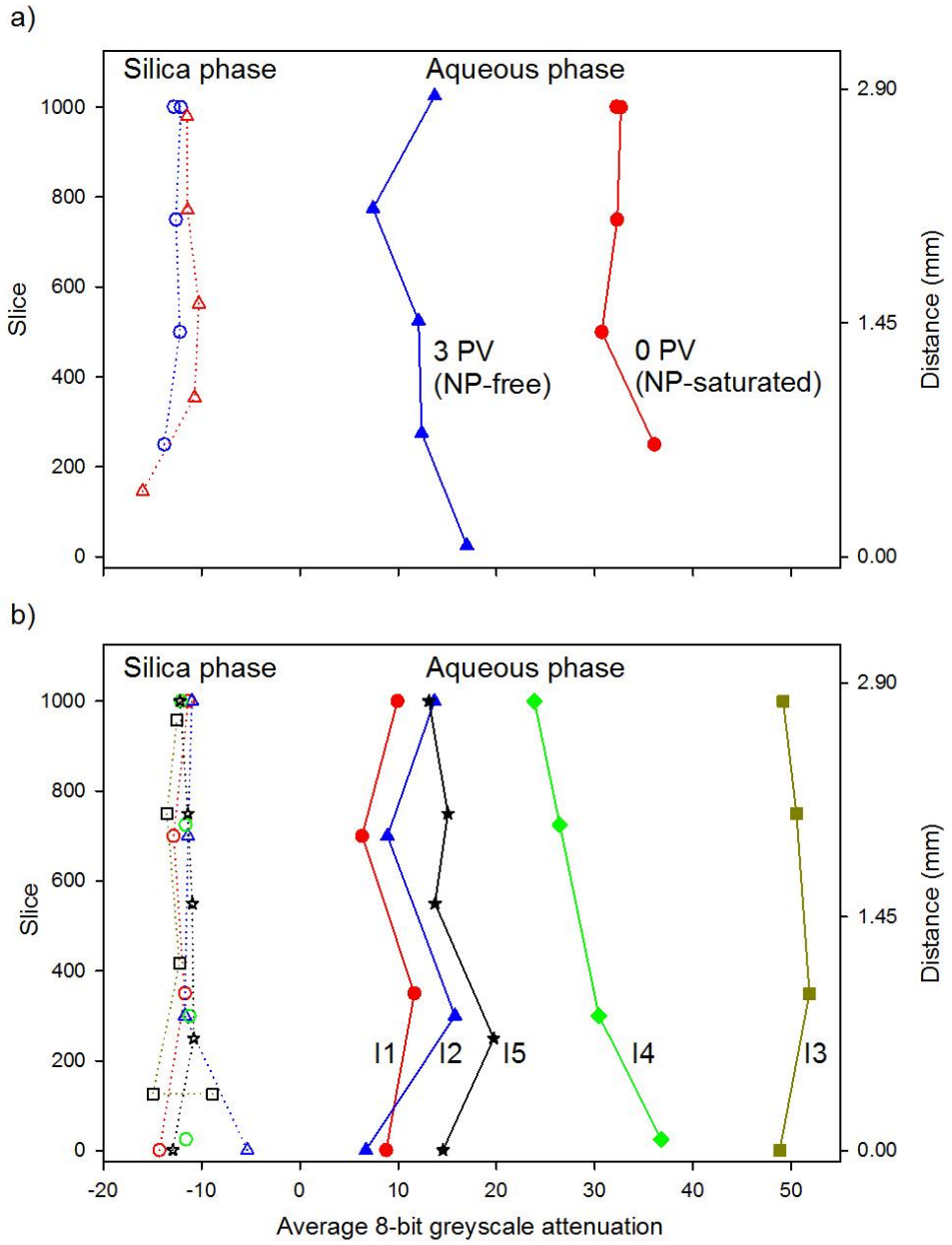

Figure 4.6. Column profiles (2.9 mm length) with average X-ray attenuation, as a function of slice (and distance) from tomography experiments on Pd-NP in ultrapure water using discrete analysis of the above-below difference images for a) Column 1 and b) Column 2.

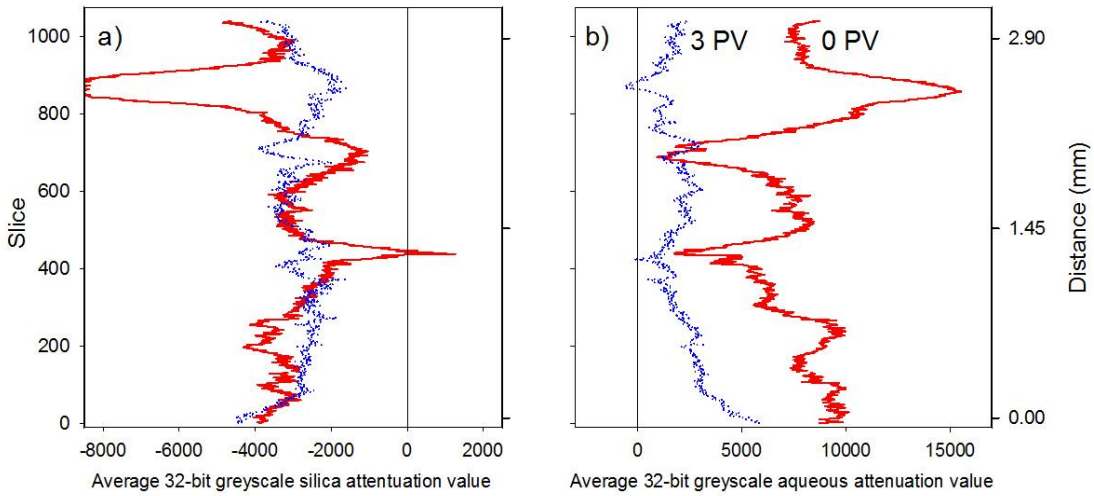

Figure 4.7. Column 1 profiles from Pd-NP suspension saturated (solid red line) and NP-free water saturated (dotted blue line) images for: a) silica GSV and b) aqueous GSV. Narrow-black lines are added at x-values = 0. Outliers have been removed.

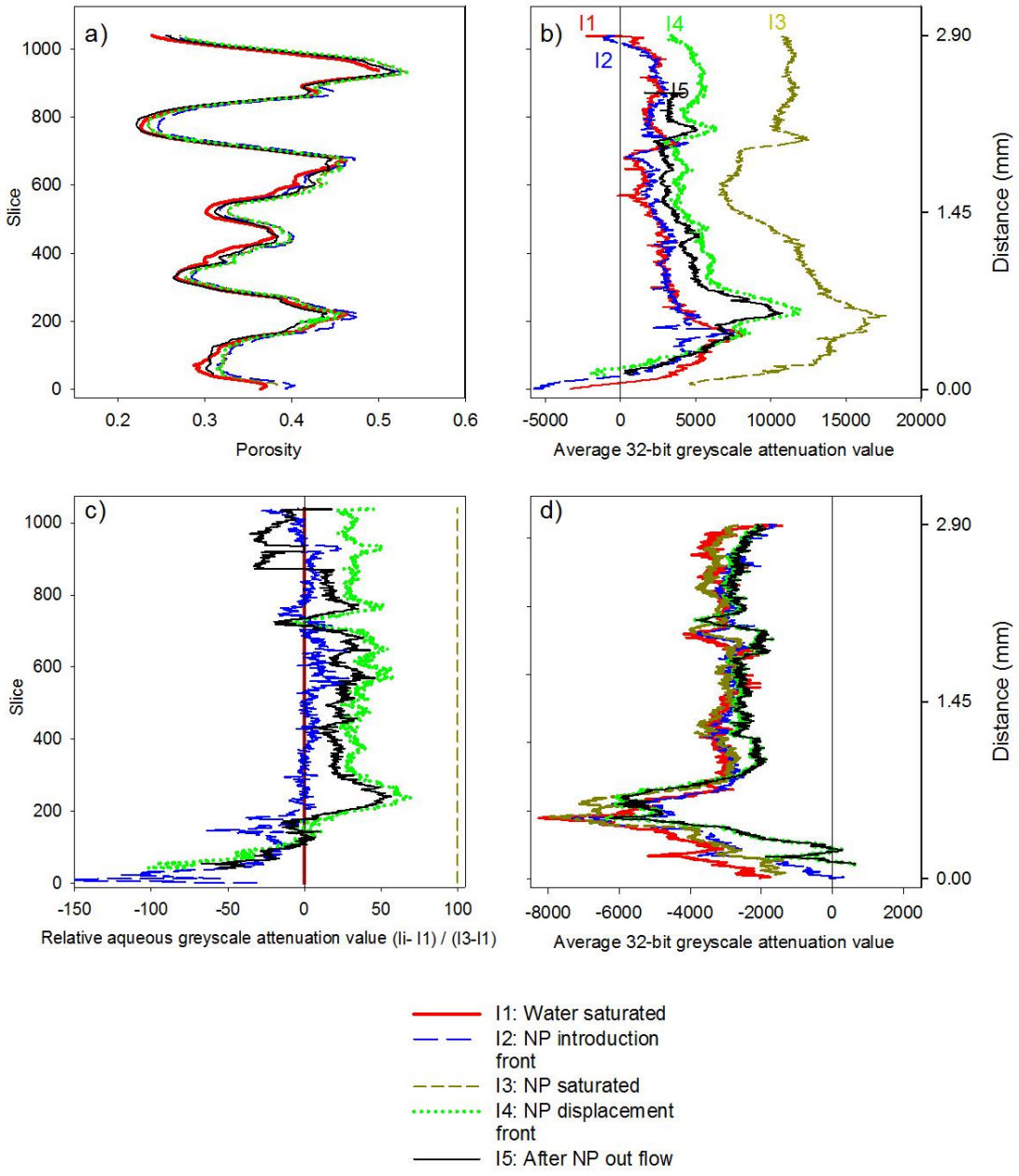

Figure 4.8. Column 2 profiles of Pd-NP transport in the five sequential images for: a) porosity, b) aqueous GSV, c) aqueous GSV relative to the difference between I3 and I1 and blank corrected using I1, and d) silica GSV. Narrow-black lines are added at x-values = 0. Outliers have been removed.

a)

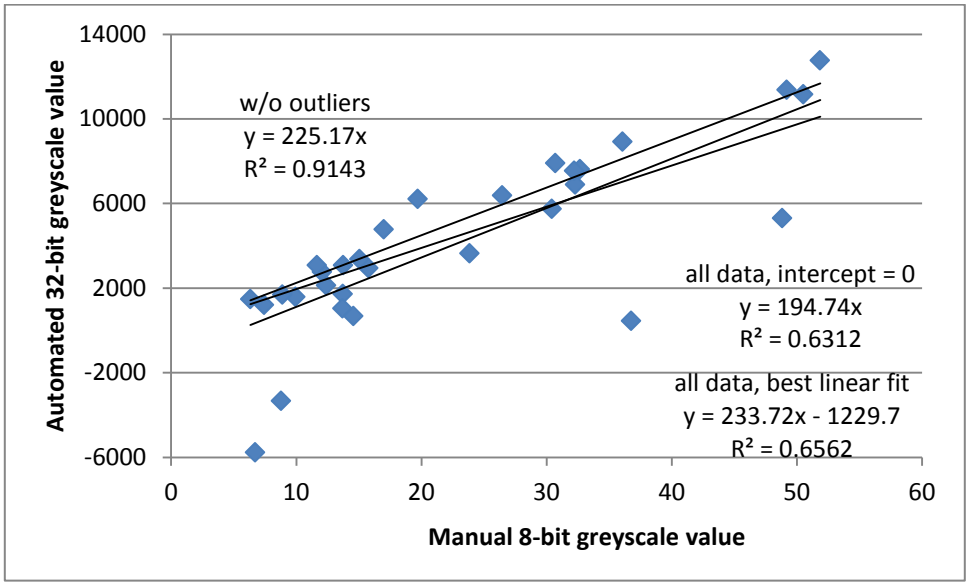

b)

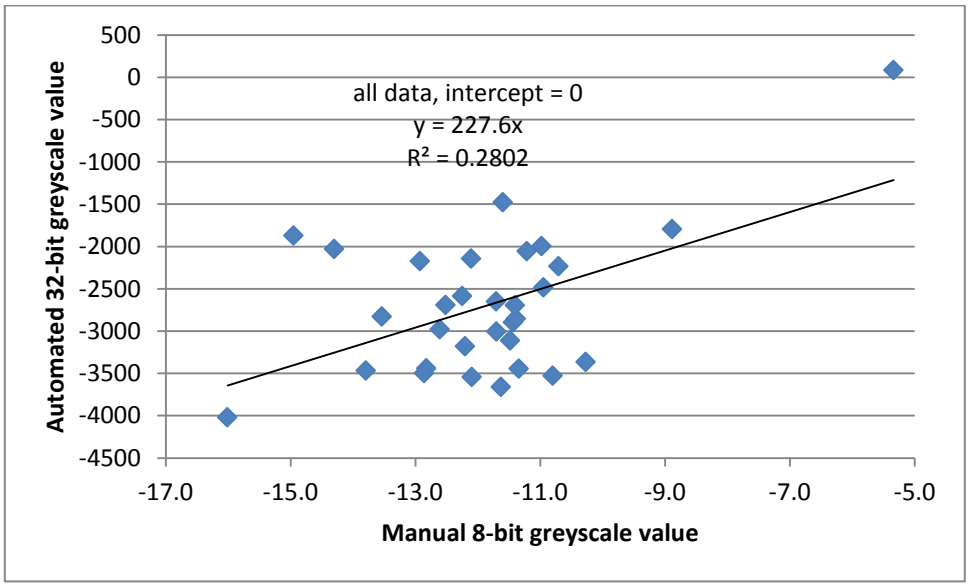

Figure 4.9. Comparing a) aqueous and b) silica phase greyscale values determined from two columns and 7 images of discretized values to the continuously determined values of all voxels determined for the same slices.

4.7 Tables

Table 4.1. Average parameters determined from tomographic difference images for all voxels expressed as arithmetic averages ($\bar{x}$) and standard deviations (σ).

		Porosity		**Aqueous Phase**		**Silica Phase**		**Aqueous Phase blank corrected**	**Aqueous Phase blank corrected relative to maximum**
		$\bar{x}$	σ	$\bar{x}$	σ	$\bar{x}$	σ	$(\boldsymbol{I_i - I1})$	$((\boldsymbol{I_i - I1})/(\boldsymbol{I3 - I1}))$
C1	**Initial – NP saturated**	0.369	0.065	7684	2667	-3389	1687	No blank	
	3 PV after NP flushed	0.376	0.058	2034	1022	-2823	501		
C2	**I1: Initial**	0.351	0.067	2758	1722	-3430	986	0.00	0.00
	I2: NP introduction	0.372	0.068	2473	1729	-2998	975	-284	-0.03
	I3: NP saturated	0.369	0.070	11110	2607	-3247	1033	8352	1.00
	I4: Partial NP flush	0.370	0.071	5256	2192	-2711	1160	2499	0.30
	I5: After NP flush	0.355	0.071	4526	2009	-3183	1096	1769	0.21

Chapter 5
Conclusions

This thesis presented results from experiments with superparamagnetic iron oxide nanoparticles (SPION) and palladium nanoparticles (Pd-NP) to evaluate aqueous stability and transport through porous media. The emerging use of NP as a remediation tool has focused on nano zero-valent iron (nZVI) and carbon nanotubes. Although research on SPION has thus far concentrated on medical applications and wastewater treatment applications, SPION may also be useful for groundwater remediation due to their ability to carry catalysts and their recoverability. Here, the effects of NP size and Pd on stability and transport of controlled SPION aggregates (CSA) were evaluated. Additionally, Pd-NP were imaged with synchrotron-based microtomography during transport through a column.

Experiments included batch suspension tests to determine the stability of Pd on the CSA surface under various environmental conditions. Suspension tests were monitored over time with photographs or continuous absorbance readings within common geochemical environments. Transport of NP through saturated porous media was investigated with column breakthrough experiments. Column tests were complemented by calculations of attachment efficiency to assess degree of attachment and with one-dimensional transport simulations to quantify CSA transport relative to a conservative tracer. A synchrotron facility was used for microtomography of Pd-NP transport in porous media using small-scale columns to obtain non-destructive 3-D spatial and temporal images of the NP. The objective of the tomography study was to determine the usefulness of the technique for evaluating transport of Pd-based NP within silica sand grains.

The CSA were designed to separate from solution following extraction of treated water when under the influence of a magnetic field. The benefit of magnetic recoverability allows for the reuse of the CSA after recovery from a contamination zone. The polymer coating used could affect the toxicity of the NP. As a potential neurotoxin, polyacrylamide (the coating for CSA used) may not be appropriate for field applications

as full recovery of the NP in not realistic. As CSA are not a reactive material, an electron donor may be required as a reaction source, allowing Pd on the CSA to catalyze the reaction. This reactive source could be the NP coating if it is an electron donor. Without a reactive coating, adding a reactive media with an nZVI co-injection or using naturally occurring dissolved H_2 would be required. The addition of CSA@Pd can provide long-term catalysis to naturally occurring reactions.

Results from aqueous suspension tests showed consistent trends. NP in ultrapure water are the most stable, followed by in NaCl and then $MgSO_4$ solution, and the least stability and most aggregation in $CaCO_3$ solution. The addition of Pd onto the surface of the CSA did not significantly alter the stability. The Pd-NP remained completely suspended in all environments tested over a week, while the CSA remained suspended a maximum of one week. The Pd-NP were 5-50 nm in diameter compared to 100, 240, and 340 nm for the three CSA sizes, suggesting size is significant regarding aqueous stability, even though based on surface charge, CSA (-46 mV) is expected to have higher stability than the Pd-NP (-10 mV). Among the CSA, more rapid settling was observed with increased size, solute concentration, and ion charge. Decreased stability of larger NP (300 nm vs. 100 nm) contradicts results published on NP in the 10-100 nm range, suggesting different mechanisms of settling and suspension.

Column experiments conducted using Ottawa silica sand showed that NP transport was conservative in ultrapure water, matching very closely to the chloride tracer test results and yielding attachment efficiencies (α) ~ 0.0. In contrast, less than 5 % of the CSA were eluted with $CaCO_3$ solutions following irreversible attachment, except for CSA-100 in 1.3 mM IS (10 % saturation) $CaCO_3$ solution where ~ 85 % of the CSA were eluted. Retention within the column was likely caused by aggregation of the NP and attachment to the collector grains. Inverse one-dimensional transport simulations conducted using the CXTFIT component in STANMOD indicated minimal retardation. With α values > 2.5 observed for $CaCO_3$ solutions, mechanisms not included within the colloidal filtration theory, such as ripening, straining, and wedging, are likely a factor as CFT limits α to 0-1. Transport distances calculated from column tests in $CaCO_3$ solutions are similar to transport distances observed in field injections of coated nZVI. Only small proportions of CSA were detached when removing $CaCO_3$ ions from the

column at an increasing flow rate. In a parallel column experiment with a $CaCl_2$ input solution, full detachment was observed when the input solution was changed to ultrapure water. Different attachment mechanisms were likely for $CaCl_2$ and $CaCO_3$ solutions. Pd-NP were fully mobile using all solutions tested.

Transport of CSA in $CaCO_3$ and $CaCl_2$ solutions differed, suggesting that, in addition to ionic strength, ion charge, and flow rate, pH affects transport because the surface charge of the porous media and the surface charge of the organic coating on the NP are pH dependent. Column tests results suggest the potential for injection followed by recovery of CSA through pumping with appropriate well geometry in groundwater systems containing limited concentrations of dissolved monovalent ions and no other ions, which may not apply to contaminated sites. However, modifications will be required to allow transport in carbonate-bearing aquifers, particularly under high pH conditions. Pd-NP recovery is likely high, regardless of the geochemistry. The consideration of specific groundwater composition of injection sites is vital to any potential successful remediation approach.

Full transport of nZVI has not been documented for field injections. However, for CSA during remediation applications in a pumped system attachment may be preventable and full recovery may be achievable with a low ionic strength solution and high flow rates. In cases where the NP cannot be recovered and reused, the NP may remain in place, resulting in the development of an *in situ* barrier, which is the current result of nZVI injections. This situation would likely arise in $CaCO_3$-rich environments. Field system designs could include components to promote temporary NP attachment followed by detachment, for example, a $CaCl_2$-rich groundwater could be used to promote attachment and subsequent injection of low ionic strength water would promote NP detachment, providing an opportunity for subsequent NP recovery. In this study, mobility has been shown to be dependant on the composition of the aqueous solution, but is only one factor for field-scale injections. Direct testing in the field is suggested prior to large scale implementation.

Toxicity of NP is important, especially from a drinking water perspective. At NP concentrations well below those used in remediation, some nanomaterials have been found to be toxic. In applications where potentially toxic NP are used for remediation

purposes, NP properties and mobility must be well defined, and containment of NP may be required to prevent release to the environment.

Synchrotron-based microtomography was used for quantifying Pd-NP transport through silica sand columns. Using beamline specific software and ImageJ, tomographic images collected at energies above and below Pd absorption-edge were processed to determine porosity, aqueous phase greyscale values, and silica greyscale values. Porosity varied between slices based on the grain packing and can be used to indicate consistency in alignment between images. With constant silica phase attenuation values from image to image, aqueous phase greyscale values showed an increase when NP were present and a decrease when NP were not present. Thus, Pd-NP were detected and traced through the column during mobility tests. The use of silica grains, a more complex matrix than what was used in the past, can provide images of sufficient quality for segmentation and analysis. Further analysis is needed to quantify the transport beyond relative quantification values determined in this study.

This thesis reported on initial experimentation of transport of CSA and Pd-NP and provided additional understanding relating to NP transport and tomography studies. Further research is needed to expand on the foundation for the use of CSA and Pd-NP for groundwater remediation applications. Such research includes:

- Use more complex solution chemistry containing more solutes, typical of field sites, as only common, isolated solutes have been studied. The compounded effect of multiple cations and multiple anions may not correspond to cumulative ionic strength.
- Investigate the effect of porous media on NP transport both using conventional and novel tomography experiments. Uniform homogenous coarse sand was used in the column experiments. However, in finer and more heterogeneous mediums, the NP behaviour will likely differ. Additionally, the porous media mineralogy also should be examined to determine the effects of mineral-surface charges.
- Evaluate a charged polymer on the CSA, such as PAA, rather than the neutral PAM examined in this study, to determine whether enhanced particle stability could be achieved, similar to the stability observed during the Pd-NP experiments.

- Optimization of NP reactivity through a comparison of pure Pd-NP, uncoated CSA, CSA@Pd, and commonly used ZVI to assess possible enhancements to catalytic and reactive properties. These studies are essential to determine the system needed for increased remediation reactions due to the presence of Pd.
- Conduct tomography column experiments under more favorable deposition conditions to provide helpful information related to retention behaviour.
- Include more rigorous analysis of tomography data by incorporating Beer's Law (Molnar et al., 2014) to adjust the attenuation values to elemental concentrations; obtain raw data from well-characterized standards to calibrate experimental images to actual concentrations; and create a macro to enable automation of operations needed to process the reconstructed volumes.
- Redesign experimental conditions to eliminate experimental and processing difficulties to improve data quality. Improvements to the method would be to increase the now-limited detection of NP and increase the contrast in phases, and to reproduce column alignment between images. These modifications include: increase water contrast with an iodide salt, increase NP concentration for better detection, and improve the column holder design.

Through the use of suspension tests, column experiments, and microtomographic images, this study provided a better understanding of the stability and transport of nanoparticles, characteristics that are of critical importance to successful in situ groundwater remediation applications. Transport is dependent on specific NP properties, such as size, surface coating, and surface charge, as well as on the aqueous solution.

References

Alaskar, M., Ames, M., Connor, S., Liu, C., Cui, Y., Li, K., Horne, R., 2011. Nanoparticle and microparticle flow in porous and fractured media: An experimental study. SPE Annual Technical Conference and Exhibition, Denver, CO, October 30-November 2, 2011. SPE (Society of Petroleum Engineers) 146752.

Ben-Moshe, T., Dror, I., Berkowitz, B., 2010. Transport of metal oxide nanoparticles in saturated porous media. Chemosphere 81, 387-393. 10.1016/j.chemosphere.2010.07.007.

Benn, T., Cavanagh, B., Hristovski, K., Posner, J. D., Westerhoff, P., 2010. The release of nanosilver from consumer products used in the home. J. Environ. Qual. 39, 6, 1875-1882. 10.2134/jeq2009.0363.

Bennett, P., He, F., Zhao, D., Aiken, B., Feldman, L., 2010. In situ testing of metallic iron nanoparticle mobility and reactivity in a shallow granular aquifer. J. Contam. Hydrol. 116, 35-46. 10.1016/j.jconhyd.2010.05.006.

Bergendahl, J.A., Grasso, D., 2003. Mechanistic basis for particle detachment from granular media. Environ. Sci. Technol. 37, 2317-2322. 10.1021/es0209316.

Blowes, D.W., Ptacek, C.J., Benner, S.G., McRae, C.W.T., Bennett, T.A., Puls, R.W., 2000. Treatment of inorganic contaminants using permeable reactive barriers. J. Contam. Hydrol. 45, 1-2, 123-137.

Bradford, S.A., Yates, S.R., Bettahar, M., Simunek, J., 2002. Physical factors affecting the transport and fate of colloids in saturated porous media. Water Resour. Res. 38, 12, 631-6312.

Busch, J., Meißner, T., Potthoff, A., Oswald, S.E., 2014. Transport of carbon colloid supported nanoscale zero-valent iron in saturated porous media. J. Contam. Hydrol., 164, 25-34. 10.1016/j.jconhyd.2014.05.006.

Chan, T., Gu, F., 2013. Development of a colorimetric, superparamagnetic biosensor for the capture and detection of biomolecules. Biosens. Bioelectron. 42, 12-16. 10.1016/j.bios.2012.10.008.

Chaplin, B.P., Reinhard, M., Schneider, W.F., Schüth, C., Shapley, J.R., Strathmann, T.J., Werth, C.J., 2012. Critical review of Pd-based catalytic treatment of priority contaminants in water. Environ. Sci. Technol. 46, 3655-3670. 10.1021/es204087q.

Chen, K.L., Elimelech, M., 2006. Aggregation and deposition kinetics of fullerene (C60) nanoparticles. Langmuir 22, 26, 10994-11001.

Cheng, W., Tang, K., Qi, Y., Sheng, J., Liu, Z., 2010. One-step synthesis of superparamagnetic monodisperse porous Fe_3O_4 hollow and core-shell spheres. J. Mater. Chem. 20, 9. 1799-1805. 10.1039/B919164J

Choy, C. C., Wazne, M., Meng, X., 2008. Application of an empirical transport model to simulate retention of nanocrystalline titanium dioxide in sand columns. Chemosphere 71, 9, 1794–1801.

Cirtiu, C.M., Raychoudhury, T., Ghoshal, S., Moores, A., 2011. Systematic comparison of the size, surface characteristics and colloidal stability of zero valent iron nanoparticles pre- and post-grafted with common polymers. Colloid. Surface. A., 390, 1-3, 95-104.

Comba, S., Sethi, R., 2009. Stabilization of highly concentrated suspensions of iron nanoparticles using shear-thinning gels of xanthan gum. Water Res. 43, 3717-3726. 10.1016/j.watres.2009.05.046.

Cornelis, G., Pang, L., Doolette, C., Kirby, J.K., McLaughlin, M.J., 2013. Transport of silver nanoparticles in saturated columns of natural soils. Sci. Total Environ. 463-464, 120-130.

Culligan, K.A., Wildenschild, D., Christensen, B.S.B., Gray, W.G., Rivers, M.L., 2006. Pore-scale characteristics of multiphase flow in porous media: A comparison of air–water and oil–water experiments. Adv. Water Resour. 29, 227-238.

EPA (United States Environmental Protection Agency), 2008. Nanotechnology for Site Remediation Fact Sheet. Accessed September 28, 2014., from http://nepis.epa.gov/Exe/ZyNET.exe/P1001JIB.TXT?ZyActionD=ZyDocument&Client=EPA&Index=2006+Thru+2010&Docs=&Query=&Time=&EndTime=&SearchMethod=1&TocRestrict=n&Toc=&TocEntry=&QField=&QFieldYear=&QFieldMonth=&QFieldDay=&IntQFieldOp=0&ExtQFieldOp=0&XmlQuery=&F.

Esfahani, A.R., Firouzia, A.F., Sayyad, G., Kiasat, A.R., 2014. Transport and retention of polymer-stabilized zero-valent iron nanoparticles in saturated porous media: Effects of initial particle concentration and ionic strength. J. Ind. Eng. Chem. 20, 2671-2679. 10.1016/j.jiec.2013.10.054.

Fang, J., Shan, X., Wen, B., Lin, J., Owens, G., 2009. Stability of titania nanoparticles in soil suspensions and transport in saturated homogeneous soil columns. Environ. Pollut. 157, 4, 1101–1109.

Freeze, R. A., Cherry, J. A., 1979. Groundwater. Englewood Cliffs, New Jersey.

Grieger, K.D., Fjordbøge, A., Hartmann, N.B., Eriksson, E., Bjerg, P.L., Baun, A., 2010. Environmental benefits and risks of zero-valent iron nanoparticles (nZVI) for in situ remediation: Risk mitigation or trade-off? J. Contam. Hydrol. 118, 165–183. 10.1016/j.jconhyd.2010.07.011.

Gupta, A.J., Gupta, M., 2005. Synthesis and surface engineering of iron oxide nanoparticles for biomedical applications. Biomaterials 26, 3995-4021.

Hahn, M.W., Abadzic, D., O'Melia,C.R., 2004. Aquasols: on the role of secondary minima. Environ. Sci. Technol. 38, 22, 5915-5924.

He, F., Zhao, D., 2005. Preparation and characterization of a new class of starch-stabilized bimetallic nanoparticles for degradation of chlorinated hydrocarbons in water. Environ. Sci. Technol. 39, 3314-3320.

He, Y.T., Wan, J., Tokunaga, T., 2008. Kinetic stability of hematite nanoparticles: the effect of particle size. J. Nanopart. Res. 10, 2, 321-332.

He, F., Zhang, M., Qian, T., Zhao, D., 2009a. Transport of carboxymethyl cellulose stabilized iron nanoparticles in porous media: column experiments and modeling. J. Colloid. Interf. Sci. 334, 96-102. 10.1016/j.jcis.2009.02.058.

He, F., Zhao, D., Roberts, C., 2009b. Stabilization of zero-valent iron nanoparticles for enhanced in situ destruction of chlorinated solvents in soils and groundwater, in: Savage, N., Diallo, M., Duncan, J., Street, A., Sustich, R. (Eds.), *Nanotechnology Applications for Clean Water*. William Andrew, Norwich, NY, Chapter 20, 281-291.

He, F., Zhao, D., Paul, C., 2010. Field assessment of carboxymethyl cellulose stabilized iron nanoparticles for the in situ destruction of chlorinated solvents in source zones. Water Res. 44, 2360-2370.

Health Canada, 2010. Guidelines for Canadian drinking water quality. December. Accessed November 20, 2011, from http://www.hc-sc.gc.ca/ewh-semt/pubs/water-eau/2010-sum_guide-res_recom/index-eng.php.

Hemansson, M., 1999. The DLVO theory in microbial adhesion. Colloid Surface. B. Biointerfaces, 14, 105-119.

Horák, D., Babič, M., Macková, H., Beneš, M.J., 2007. Preparation and properties of magnetic nano- and microsized particles for biological and environmental separations. J. Sep. Sci. 30, 1751-1772. 10.1002/jssc.200700088.

Hosseini, S.M., Tosco, T., 2013. Transport and retention of high concentrated nano-Fe/Cu particles through highly flow-rated packed sand column. Water Res., 47, 1, 326-338.

Hotze, E., Phenrat, T., Lowry, G., 2010. Nanoparticle aggregation: challenges to understanding transport and reactivity in the environment. J. Environ. Qual. 39, 1909-1924.

Iltis, G.C., Armstrong, R.T., Jansik, D.P., Wood, B.D., Wildenschild, D., 2011. Imaging biofilm architecture within porous media using synchrotron-based X-ray computed microtomography. Water Resour. Res. 47, W02601. 10.1029/2010WR009410.

Jaisi, D.P., Saleh, N.B., Blake, R.E., Elimelech, M., 2008. Transport of single-walled carbon nanotubes in porous media: filtration mechanisms and reversibility. Environ. Sci. Technol. 42, 8317-8323.

Jiang, X., Wang, X., Tong, M., Kim, H., 2013. Initial transport and retention behaviors of ZnO nanoparticles in quartz sand porous media coated with *Escherichia coli* biofilm. Environ. Pollut. 174, 38-49.

Jiemvarangkul, P., Zhang, W., Lien, H., 2011. Enhanced transport of polyelectrolyte stabilized nanoscale zero-valent iron (nZVI) in porous media. Chem. Eng. J. 170, 482-491. 10.1016/j.cej.2011.02.065.

Johnson, R.L., Nurmi, J.T., O'Brien Johnson, G.S., Fan, D., O'Brien Johnson, R.L., Shi, Z., Salter-Blanc, A.J., Tratnyek, P.G., Lowry, G.V., 2013. Field-scale transport and transformation of carboxymethylcellulose- stabilized nano zero-valent iron. Environ. Sci. Technol. 47, 3, 1573-1580. 10.1021/es304564q.

Jones, E.H., Su., C., 2014. Transport and retention of zinc oxide nanoparticles in porous media: Effects of natural organic matter versus natural organic ligands at circumneutral pH. J. Hazard. Mater. 275, 79-88.

Kim, S.A., Kamala-Kannan, S., Lee., K.J., Park., Y.J., Shea, P.J., Lee, W.H., Kim, H.M, Oh, B.T., 2013. Removal of Pb(II) from aqueous solution by a zeolite–nanoscale zero-valent iron composite. Chem. Eng. J. 217, 54-60.

Klaine, S.J., Alvarez, P.J.J., Batley, G.E., Fernandes, T.F., Handy, R.D., Lyon, D.Y., Mahendra, S., McLaughlin, M.J., Lead, J.R., 2008. Nanomaterials in the environment: Behavior, fate, bioavailability, and effects. Environ. Toxic. Chem. 27, 9, 1825-1851. 10.1897/08-090.1.

Kocur, C.M., Chowdhury, A.I., Sakulchaicharoen, N., Boparai, H.K., Weber, K.P., Sharma, P., Krol, M.M., Austrins, L., Peace, C., Sleep, B.E., O'Carroll, D.M., 2014. Characterization of nZVI mobility in a field scale test. Environ. Sci. Technol. 48, 5, 2862-2869. 10.1021/es4044209.

Kong, L., Lu, X., Bian, X., Zhang, W., Wang, C., 2011. Constructing carbon-coated Fe_3O_4 microspheres as antiacid and magnetic support for palladium nanoparticles for catalytic applications. ACS Appl. Mater. Interfaces *3*, 1, 35–42.

Kosmulski, M., 2004.pH-dependent surface chargin and points of zero charge II. Update. J. Colloid Interf. Sci. 275, 214-224. 10.1016/j.jcis.2004.02.029.

Laumann, S., Mici, V., Lowry, G.V., Hofmann, T., 2013. Carbonate minerals in porous media decrease mobility of polyacrylic acid modified zero-valent iron nanoparticles used for groundwater remediation. Environ. Pollut. 179, 53-60. 10.1016/j.envpol.2013.04.004.

Laumann, S., Mici, V., Hofmann, T., 2014. Mobility enhancement of nanoscale zero-valent iron in carbonate porous media through coinjection of polyelectrolytes. Water Res. 50, 70-79. 10.1016/j.watres.2013.11.040.

Leshuk, T., Krishnakumar H., Gu, F., 2013. Size-tunable Fe_3O_4 spherical nanoclusters

through a one-pot hydrothermal synthesis. J. Nanosci. Nanotech. 13, 4, 3127-32.

Li, Z., Sahle-Demessie, E., Hassan, A.A., Sorial, G.A., 2011. Transport and deposition of CeO_2 nanoparticles in water-saturated porous media. Water Res. 45, 15, 4409-4418. 10.1016/j.watres.2011.05.025.

Lien, H.L., Zhang, W.X., 2007. Nanoscale Pd/Fe bimetallic particles: catalytic effects of palladium on hydrodechlorination. Appl. Catal. B – Environ. 77, 110–116.

Lin, D., Tian, X., Wu, F., Xing, B., 2010. Fate and transport of engineered nanomaterials in the environment. J. Environ. Qual. 39, 1896-1908. 10.2134/jeq2009.0423.

Linley, S., Liu, Y., Ptacek, C.J., Blowes, D.W., Gu, F.X., 2014. Recyclable graphene oxide-supported titanium dioxide photocatalysts with tunable properties. Appl. Mater. Interfaces 6, 4658-4668. 10.1021/am4039272.

Liu, J., Zhao, Z., Jiang, G., 2008. Coating Fe_3O_4 magnetic nanoparticles with humic acid for high efficient removal of heavy metals in water. Environ. Sci. Technol. 42, 6949-6954. 10.1021/es800924c.

Liu, W., Qian, T., Jiang, H., 2014. Bimetallic Fe nanoparticles: Recent advances in synthesis and application in catalytic elimination of environmental pollutants. Chem. Eng. J. 236, 448–463. 10.1016/j.cej.2013.10.062.

Lowry, G.V., Reinhard, M., 1999. Hydrodehalogenation of 1- to 3-carbon halogenated organic compounds in water using a palladium catalyst and hydrogen gas. Environ. Sci. Technol. 33, 11, 1905-1910. 10.1021/es980963m.

Matlochová, A., Plachá, D., Rapantová, N., 2013. The application of nanoscale materials in groundwater remediation. Pol. J. Environ. Stud. 22, 5, 1401-1410.

McGechan, M.B., Lewis, D.R., 2002. Transport of Particulate and Colloid-sorbed Contaminants through Soil, Part 1 General Principles. Biosystems Eng. 83, 3, 255-273.

Mitzel, M.R., Tufenkji, N., 2014. Transport of industrial PVP-stabilized silver nanoparticles in saturated quartz sand coated with *Pseudomonas aeruginosa* PAO1 biofilm of variable age. Environ. Sci. Technol. 48, 5, 2715-2723. 10.1021/es404598v.

Molnar, I.L., Willson, C.S., O'Carroll, D.M., Rivers, M.L., Gerhard, G.I., 2014. Method for obtaining silver nanoparticle concentrations within a porous medium via

synchrotron X-ray computed microtomography. Environ. Sci. Technol. 48, 2, 1114-1122. 10.1021/es403381s.

Mystrioti, C., Xenidis, A., Papassiopi, N., 2014. Reduction of hexavalent chromium with polyphenol-coated nano zero-valent iron: column studies. Desalination and Water Treatment. In press. 10.1080/19443994.2014.941298.

Nassar, N.N., 2012. Kinetics, equilibrium and thermodynamic studies on the adsorptive removal of nickel, cadmium and cobalt from wastewater by superparamagnetic iron oxide nanoadsorbents. Can. J. Chem. Eng. 90, 1231-1238. 10.1002/cjce.20613.

Oberdorster, E., 2004. Manufactured nanomaterial (fullerenes, C_{60}) produce oxidative stress in the brain of juvenile largemouth bass. Environ. Health Persp. 112, 10, 1058-1062.

O'Carroll, D.M., Liu, X., Mattison, N.T., Petersen, E.J., 2013a. Impact of diameter on carbon nanotube transport in sand. J. Colloid. Interf. Sci. 390, 96-104. 10.1016/j.jcis.2012.09.034.

O'Carroll, D., Sleep, B., Krol, M., Boparai, H., Kocur C., 2013b. Nanoscale zero valent iron and bimetallic particles for contaminated site remediation. Adv. Wat. Resour. 51, 104-122.

Omole, M.A., K'Owina, I.O., Sadik, O.A., 2007. Palladium nanoparticles for catalytic reduction of Cr(VI) using formic acid. Appl. Catal. B-Environ.76, 158-167. 10.1016/j.apcatb.2007.05.018.

Pang, Y., Zeng, G., Tang, L., Zhang, Y., Liu, Y., Lei, X., Li, Z., Zhang, J., Liu, Z., Xiong, Y., 2011. Preparation and application of stability enhanced magnetic nanoparticles for rapid removal of Cr(VI). Chem. Eng. J. 175, 222-227. 10.1016/j.cej.2011.09.098.

Petosa, A.R., Jaisi, D., Quevedo, I., Elimelech, M., Tufenkji, N., 2010. Aggregation and deposition of engineered nanomaterials in aquatic environments: role of physiochemical interactions. Environ. Sci. Technol. 44, 6532-6549.

Petosa, A.R., Brennan, S.J., Rajput, F., Tufenkji, N., 2012. Transport of two metal oxide nanoparticles in saturated granular porous media: Role of water chemistry and particle coating. Water Res. 46, 1273-1285.

Petosa, A.R., Öhl, C., Rajput, F., Tufenkji, N., 2013. Mobility of nanosized cerium dioxide and polymeric capsules in quartz and loamy sands saturated with model and natural groundwaters. Water Res. 47, 5889-5900.

Phenrat, T. Lowry, G.V., 2009. Physicochemistry of polyelectrolyte coatings that increase stability, mobility, and contaminant specificity of reactive nanoparticles used for groundwater remediation, in: Savage, N., Diallo, M., Duncan, J., Street, A., Sustich, R. (Eds.), *Nanotechnology Applications for Clean Water*. William Andrew, Norwich, NY, Chapter 18, 249-267.

Piccinno, F., Gottschalk, F., Seeger, S., Nowack, B., 2012. Industrial production quantities and uses of ten engineered nanomaterials in Europe and the world. J. Nanopart. Res. 14, 1109-1119. 10.1007/s11051-012-1109-9.

Ponder, S.M., Darab, J.G., Mallouk, T.E., 2000. Remediation of Cr(VI) and Pb(II) aqueous solutions using supported, nanoscale zero-valent iron. Environ. Sci. Technol. 32, 12, 2564-2569.

Quevedo, I. R., Tufenkji, N., 2009. Influence of solution chemistry on the deposition and detachment kinetics of a CdTe quantum dot examined using a quartz crystal microbalance. Environ. Sci. Technol. 43, 9, 3176–3182.

Quinn, J., Geiger, C., Clausen, C., Brooks, K., Coon, C., O'Hara, S., Krug, T., Major, D., Yoon, W.S., Gavaskar, A., Holdsworth, T., 2005. Field demonstration of DNAPL dehalogenation using emulsified zero-valent iron. Environ. Sci. Technol. 39, 1309-1318.

Ramanan, B., Holmes, W.M., Sloan, W.T., Phoenix, V.R., 2012. Investigation of nanoparticle transport inside coarse-grained geological media using magnetic resonance imaging. Environ. Sci. Technol. 46, 1, 360-366. 10.1021/es2012726.

Raychoudhury, T., Tufenkji, N., Ghoshal, S., 2014. Straining of polyelectrolyte-stabilized nanoscale zero valent iron particles during transport through granular porous media. Water Res. 50, 80-89. 10.1016/j.watres.2013.11.038.

Rivers, M. L., 2014. GSECARS Tomography Processing Software. http://cars9.uchicago.edu/software/idl/tomography.html (accessed Aug. 29, 2014).

Rivers, M.L., Gualda, G.A.R., 2009. 'tomo_display' and 'vol_tools': IDL VM packages for tomography data reconstruction, processing, and visualization. *Eos Transactions AGU* 90(22), Joint Assembly Supplement, Abstract V13A-06.

Rosen, J.E., Chan, L., Shieh, D., Gu, F., 2012. Iron oxide nanoparticles for targeted cancer imaging and diagnostics. Nanomed.: Nanotechnol. Biol. Med. 8, 275-290.

Ryan, J.N., Elimelech, M., 1996. Colloid mobilization and transport in groundwater. Colloid. Surface A 107, 1-56.

Sagee, O., Dror, I., Berkowitz, B., 2012. Transport of silver nanoparticles (AgNPs) in soil. Chemosphere 88, 670-675. 10.1016/j.chemosphere.2012.03.055.

Sakthivadivel, R., 1969. Clogging of a granular porous medium by sediment. Tech Report HEL 15-7, 106.

Sakulchaicharoen, N., O'Carroll, D.M., Herrera, J.E., 2010. Enhanced stability and dechlorination activity of pre-synthesis stabilized nanoscale FePd particles. J. Contam. Hydrol. 118, 117–127. 10.1016/j.jconhyd.2010.09.004.

Saleh, N., Sirk, K., Liu, Y., Phenrat, T., Dufour, B., Matyjaszewski, K., Tilton, R.D., Lowry, G.V., 2007. Surface modifications enhance nanoiron transport and NAPL targeting in saturated porous media. Environ. Eng. Sci. 24, 1:45-57.

Schrick, B., Hydutsky, B.W., Blough, J.L., Mallouk, T.E., 2004. Delivery vehicles for zerovalent metal nanoparticles in soil and groundwater. Chem. Mater. 16, 2187-2193. 10.1021/cm0218108.

Shen, C., Lazouskaya, V., Jin, Y., Li, B., Ma, Z., Zheng, W., Huang, Y., 2012. Coupled factors influencing detachment of nano- and micro-sized particles from primary minima. J. Contam. Hydrol. 134-135, 1-11. 10.1016/j.jconhyd.2012.04.003.

Singh, S., Barick, K.C., Bahadur, D., 2011. Surface engineered magnetic nanoparticles for removal of toxic metal ions and bacterial pathogens. J. Hazard. Mater. 192, 1539-1547. 10.1016/j.jhazmat.2011.06.074.

Stimson, J., Ph.D., University of Waterloo, 2008. Colloid transport through basic oxygen furnace slag as permeable treatment media for pathogen removal.

Sun, Y., Gao, B., Bradford, S.A., Wu, L., Chen, H., Shi, X., Wu, J., 2015. Transport, retention, and size perturbation of graphene oxide in saturated porous media: Effects of input concentration and grain size. Water Res. 68, 24-33.

Tang, S.C.N., Lo, I.M.C., 2013. Magnetic nanoparticles: Essential factors for sustainable environmental applications. Water Res. 47, 2613-2632.

Teranishi, T., Miyake, M., 1998. Size control of palladium nanoparticles and their crystal structures. Chem. Mater. 10, 594–600.

Tiraferri, A., Sethi, R., 2009. Enhanced transport of zerovalent iron nanoparticles in saturated porous media by guar gum. J. Nanopart. Res. 11, 3, 635-645.

Tiraferri, A., Chen, K.L., Sethi, R., Elimelech, M., 2008. Reduced aggregation and sedimentation of zerovalent iron nanoparticles in the presence of guar gum. J. Colloid Interf. Sci. 324, 71-79.

Toride, N., Leij, F.J., Van Genuchten, M.T., 1999. *The CXTFIT Code for Estimating Transport Parameters from Laboratory or Field, Version 2.1*., USDA Department of Agriculture, Riverside, CA.

Tosco, T., Bosch, J., Meckenstock, R.U., Sethi, R., 2012. Transport of ferrihydrite nanoparticles in saturated porous media: role of ionic strength and flow rate. Environ. Sci. Technol. 46, 4008-4015.

Tratnyek, P.G., Johnson, R.L., 2006. Nanotechnologies for environmental cleanup. Nano Today 1, 2, 44-48.

Tufenkji, N., Elimelech, M., 2004. Correlation equation for predicting single-collector efficiency in physicochemical filtration in saturated porous media. Environ. Sci. Technol. 38, 529-536.

Vecchia, E.D., Luna, M., Sethi, R., 2009. Transport in porous media of highly concentrated iron micro- and nanoparticles in the presence of xanthan gum. Environ. Sci. Technol. 43, 8942-8947. 10.1021/es901897d.

Wang, C. B., Zhang, W. X., 1997. Synthesizing nanoscale iron particles for rapid and complete dechlorination of TCE and PCBs. Environ. Sci. Technol. 31, 7, 2154-

Wang, P., Shi, Q.H., Liang, H.J., Steuerman, D.W., Stucky, G.D., Keller, A.A., 2008a. Enhanced environmental mobility of carbon nanotubes in the presence of humic acid and their removal from aqueous solution. Small 4, 12, 2166–2170.

Wang, Y., Li, Y., Pennell, K.D., 2008b. Influence of electrolyte species and concentration on the aggregation and transport of fullerene nanoparticles in quartz sands. Environ. Toxic. Chem. 27, 9, 1860-1867.

Wei, Y.T., Wu, S.C., Chou, C.M., Che, C.H., Tsai, S.M., L, H.L., 2011. Influence of nanoscale zero-valent iron on geochemical properties of groundwater and vinyl chloride degradation: a field case study. Water Research 44, 131-140.

Wildenschild, D., Hopmans, J.W., Vaz, C.M.P., Rivers, M.L., Rikard, D., Christensen, B.S.B., 2002. Using X-ray computed tomography in hydrology: Systems, resolutions, and limitations. J. Hydrol. 267, 285–297.

Wildenschild, D., Hopmans, J.W., Rivers, M.L., Kent J.R., 2005. Quantitative analysis of flow processes in a sand using synchrotron-based X-ray microtomography. Vadose Zone J. 4, 112-126.

Willson, C.S., Lu, N., Likos, W.J., 2012. Quantification of grain, pore, and fluid microstructure of unsaturated sand from X-ray computed tomography images. Geotech. Test. J. 35, 6, 1-13. 10.1520/GTJ20120075.

Woodrow, J.E., Seiber, J.N., Miller, G.C., 2008. Acrylamide release resulting from sunlight irradiation of aqueous polyacrylamide/iron mixtures. J. Agric. Food Chem. 56, 8, 2773–2779. 10.1021/jf703677v.

Xiang, A., Yan, W., Koel, B., Jaffé, P., 2013. Poly(acrylic acid) coating induced 2-line ferrihydrite nanoparticle transport in saturated porous media. J. Nanopart. Res. 15, 7, 1-9. 10.1007/s11051-013-1705-3.

Xue, Z., Foster, E., Wang, Y., Nayak, S., Cheng, V., Ngo, V.W., Pennell, K.D., Bielawski, C.W., Johnston, K.P., 2014. Effect of grafted copolymer composition on iron oxide nanoparticle stability and transport in porous media at high salinity. Energy Fuels 28, 6, 3655-3665. 10.1021/ef500340h

Yahya, N., Kashif, M., Shafie, A., Solemani, H., Zaid, H.M., Latiff, N.R.A., 2014. Improved oil recovery by high magnetic flux density subjected to iron oxide nanofluids. J. Nano Res. 26, 88-99. 10.4028/www.scientific.net/JNanoR.26.89

Yan, W., Herzing, A.A., Li, X., Kiely, C.J., Zhang, W., 2010. Structural Evolution of Pd-Doped Nanoscale Zero-Valent Iron (nZVI) in Aqueous Media and Implications for Particle Aging and Reactivity. Environ. Sci. Technol. 44, 11, 4288-4294.

Yan, W., Lien, H.L., Koel, B.E., Zhang, W.X., 2013. Iron nanoparticles for environmental clean-up: Recent developments and future outlook. Environ. Sci. Processes Impacts 15, 1, 63-77.

Yang, C., Telmer, K., Veizer, J., 1996. Chemical dynamics of the "St. Lawrence" riverine system: δD_{H2O}, $\delta^{18}O_{H2O}$, $\delta^{13}C_{DIC}$, $\delta 34S_{sulfate}$, and dissolved $^{87}Sr/^{86}Sr$. Geochim. Cosmoschim. Ac. 60, 5, 851-866. 10.1016/0016-7037(95)00445-9.

Yang, W.Y., Qian, J.W., Shen, Z.Q., 2004. A novel flocculant of $Al(OH)_3$-polyacrylamide ionic hybrid. J. Colloid Interf. Sci. 273, 2, 400-405.

Yao, K., Habibian, M.T., O'Melia, C.R., 1971. Water and waste water filtration: concepts and applications. Current Research, 5, 11, 1105-1112.

Yao, Z., Wang, M., Sun, S., Jia, R., Li, H., 2014. High performance photocatalysts based on N-doped graphene-P25 for photocatalytic reduction of carbon tetrachloride. J Inorg. Organomet. Polym. 24, 315-320.

Yoffe, S., Leshuk, T., Everett, P., Gu, F., 2013. Superparamagnetic iron oxide nanoparticles (SPIONS): Synthesis and surface modification techniques for use with MRI and other biomedical applications. Curr. Pharm. Design 19, 3, 493-509.

Zhang, W.X., Elliot, D.W., 2006. Applications of iron nanoparticles for groundwater remediation. Remediation 16, 2, 7-21.

Zhang, Y., Chen, Y., Westerhoff, P., Crittenden, J., 2009. Impact of natural organic matter and divalent cations on the stability of aqueous nanoparticles. Water Res. 43, 4249-4257. 10.1016/j.watres.2009.06.005.

Zhang, X., Lin, S., Chen, Z., Megharaj, M., Naidu, R. 2011. Kaolinite-supported nanoscale zero-valent iron for removal of Pb2D from aqueous solution: Reactivity, characterization and mechanism. Water Res. 45, 348-3488.

Zhou, C., Wu, Z., Zhang, W., Xia, M., Dai, G., Zeng, G., Zou, B., Zhang, P., 2011. Facile synthesis of humic acid-coated iron oxide nanoparticles and their applications in wastewater treatment. Funct. Mater. Letters 4, 4, 373-376.

Zhuang, J., Qi, J., Jin, Y., 2005. Retention and transport of amphiphilic colloids under unsaturated flow conditions: effect of particle size and surface property. Environ. Sci. Technol. 39, 7853-7859. 10.1021/es050265j.

Appendices

Appendix A
Dynamic Light Scattering Results for Determination of Standardized Method for Particle Aggregation State

An investigation was conducted to determine a standardized procedure to implement to obtain a standard degree of nanoparticle (NP) aggregation prior to experimentation to minimize the effect of NP agglomeration over time. A solution of 1 g L^{-1} NP was divided into three vials: 1) undisturbed (UN), 2) bath sonicated (BS) for 10 min, and 3) probe sonicated (PS) for 10 min. Immediately after sonification, a dynamic light scattering (DLS) measurement was made for each sample (Table A.1.). Probe sonification significantly decreased the effective diameter of the NP relative to the initial size and resulted in decreased polydispersity. The BS resulted in less alteration of the NP size compared to PS and minimally changed the polydispersity. For the experimental work, 10 min of PS was selected as the standard procedure. Visual observations show that PS best breaks up aggregated NP and allows the NP to remain suspended overnight, while the other methods result in complete settling. Mixing with magnetic stir bars is not an option here as the NP have magnetic properties. Further, results show better de-aggregation from sonification compared to stirring (Tso et al., 2010).

Table A.1. Dynamic light scattering results for experimental pre-treatment of nanoparticles.

Sample	Effective Diameter (nm)	Polydispersity
NP UN	667	0.25
NP BS	596	0.23
NP PS	449	0.07

Reference:

Tso, C.P., Zhug, C.M., Shih, Y.H., Tseng, Y.M., Wu, S.C., Doong, R.A., 2010. Stability of metal oxide nanoparticles in aqueous solutions. Water Sci. Technol. 61, 1, 127-133.

Appendix B

DLS Characterization of CSA Batches

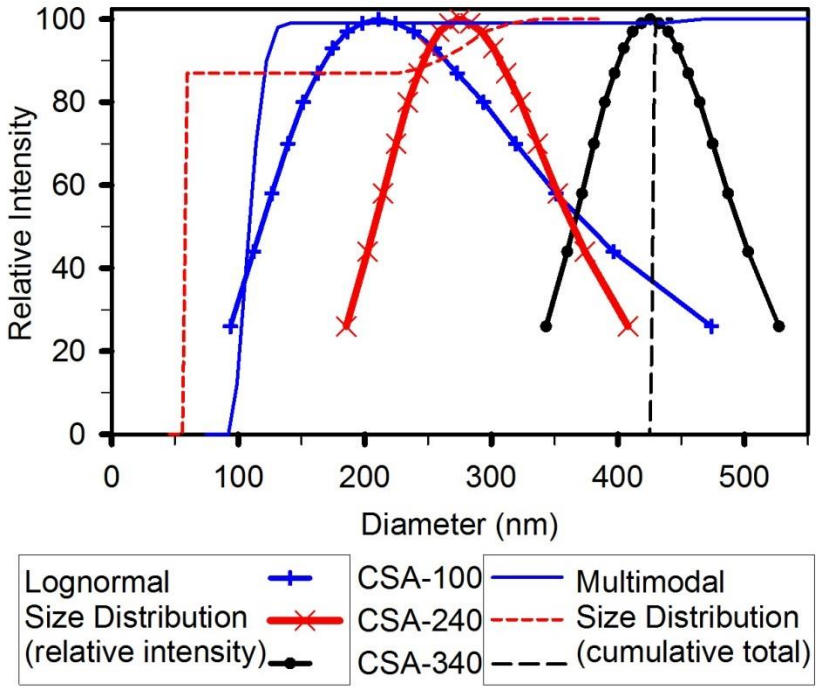

Figure A.1. Dynamic light scattering NP characterization data of CSA-100, CSA-240, and CSA-340 using lognormal and multimodal size distributions.

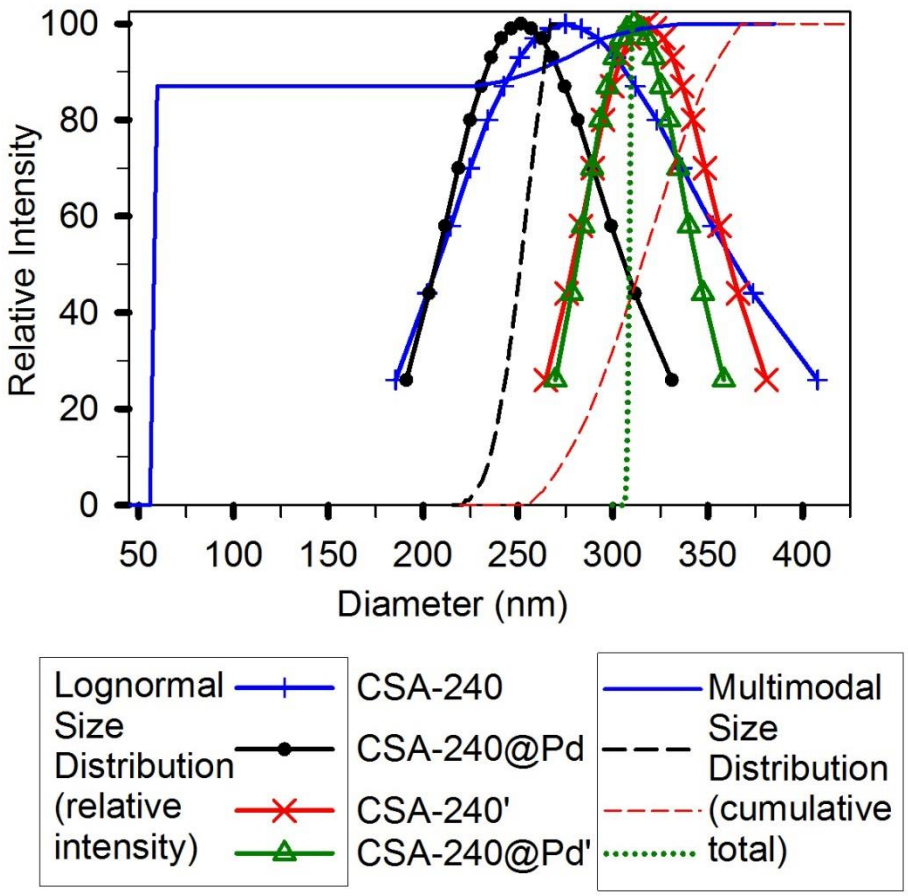

Figure A.2. Dynamic light scattering NP characterization of CSA-240 and CSA-240@Pd (and duplicate batches, denoted by ‘). Log normal and multimodal size distributions are used.

Table A.2. Dynamic light scattering NP characterization data of CSA using lognormal and multimodal size distributions (MSD).

NP	Effective Diameter (nm)	Polydispersity	MSD Results		MSD Mean
			Primary peak	Secondary peak	
CSA-100	211	0.274	105-120 (>99 %)	430-500 (<1 %)	116
CSA-240	275	0.059	59-61 (>95 %)	260-310 (<5 %)	89.5
CSA-240@Pd	252	0.028	245-265 (>95 %)	n/a	251
CSA-240'	318	0.012	311-348 (>75 %)	n/a	329
CSA-240@Pd'	311	0.008	307-310 (>95 %)	n/a	309
CSA-340	425	0.017	427-430 (100 %)	n/a	428
Pd-NP	108	0.301	89-93 (100 %)	n/a	91.0

Appendix C
Dynamic Light Scattering Results from E-ST Samplings of CSA-100

Various samples of CSA-100 were collected. Dynamic light scattering (DLS) measurements were conducted (Figure A.3) immediately after synthesis and probe sonification (fresh sample). A second DLS measurement was made following the partial settling of the sample (suspended sample). Select samples were collected from the top and bottom of various CSA-100 episodic suspension tests and DLS measurements were conducted. DLS lognormal data (Figure A.3) and multimodal size distributions (Table A.3) are shown.

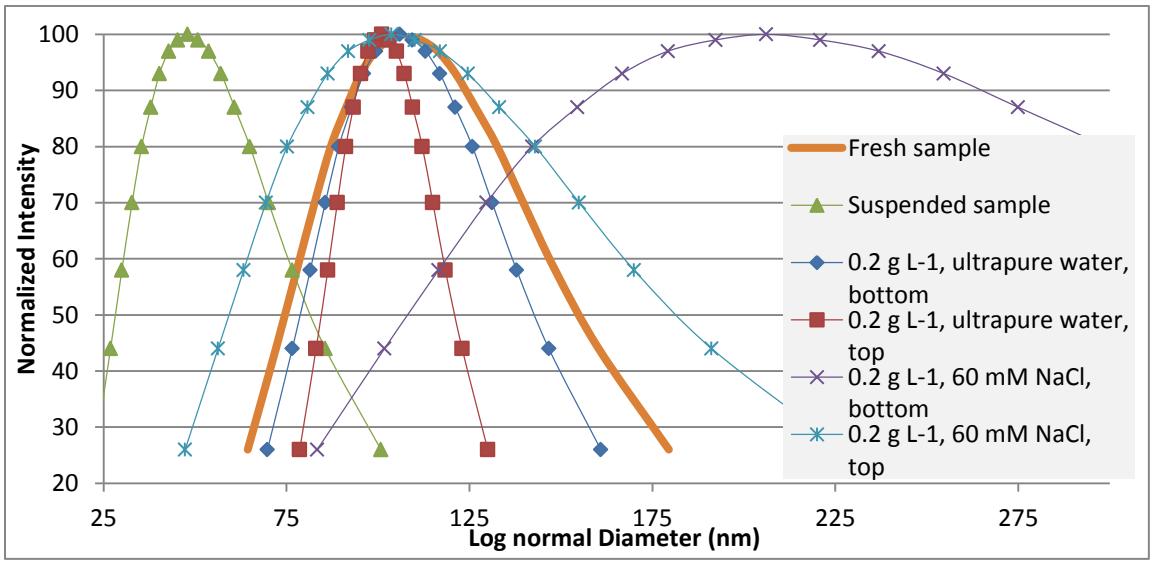

Figure A.3. Dynamic light scattering data of CSA-100 samples. The normalized intensity versus log normal hydrodynamic diameter (nm) are given. Samples are following synthesis, time on the bench, and samples of episodic suspension tests.

The fresh sample was considered the representative size and distribution. The presence of salt increased the size and the range of sizes of NP. Smaller NP are found higher in the water column, remaining suspended for longer periods of time. For the NP in ultrapure water, minimal aggregation was observed as the sizes of DLS samples of the

top and bottom layers did not differ. The only mode of separation in ultrapure water was gravity settling, whereas in ionic solutions, gravity settling and settling due to aggregation of particles occurred simultaneously. The effective diameters and polydispersivity (Table A.3) show the same trends as observed in Figure A.3.

Table A.3. DLS multimodal size distribution (MSD) data for CSA-100 measurements

	MSD major peak	**MSD secondary peak**	**Effective Diameter (nm)**	**Polydispersivity**
Fresh sample	58.2	158	137.2	0.11
Fine sample	46	n/a	79.8	0.246
0.2 g L^{-1}, ultrapure water, bottom	47.5	136	128.2	0.086
0.2 g L^{-1}, ultrapure water, top	109	n/a	108.2	0.067
0.2 g L^{-1} 60 mM IS NaCl, bottom	119	n/a	432.2	0.438
0.2 g L^{-1} 60 mM IS NaCl, top	99	45	185.5	0.265

Appendix D

Episodic Suspension Test Photographs

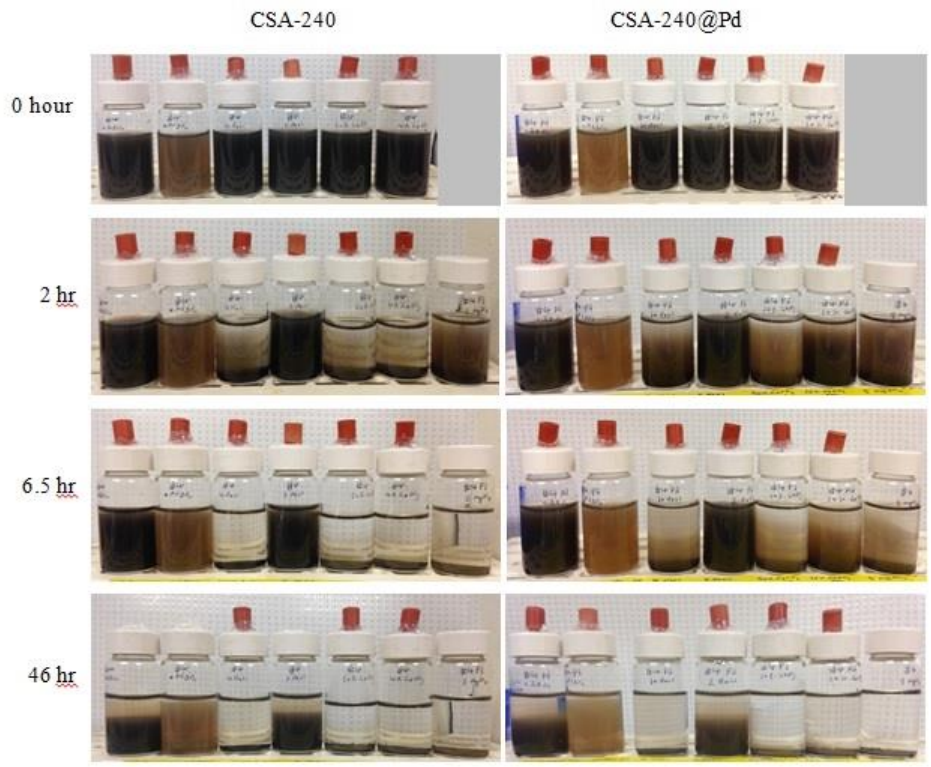

Figure A.4. E-ST photograph set of CSA-240 and CSA-240@Pd. Rows of 0 hr, 2 hr, 6.5 hr, and 46 hr photographs are shown top to bottom, respectively, with CSA-240 (left) and CSA-240@Pd (right). The vials left to right in each photograph are: 0.2 g L^{-1} and 0.04 g L^{-1} ultrapure suspensions, 10 and 2 mM IS NaCl (230 mg L^{-1} Na and 355 mg L^{-1} Cl, and 46 mg L^{-1} Na and 70.9 mg L^{-1} Cl, respectively), 5.1 and 1.3 mM IS $CaCO_3$ (50 % saturation and 96 mg L^{-1} Ca, and 10 % saturation, 19 mg L^{-1} Ca, respectively) and 4.4 mM IS $MgSO_4$ (30.4 mg L^{-1} Mg, 120 mg L^{-1} SO_4^{2-}). Note: $MgSO_4$ vial not shown at 0 hr, but was started at 0 hr, and thus has been included in remaining photos. Septa in lids provide seals to prevent evaporation but allow for easy sampling.

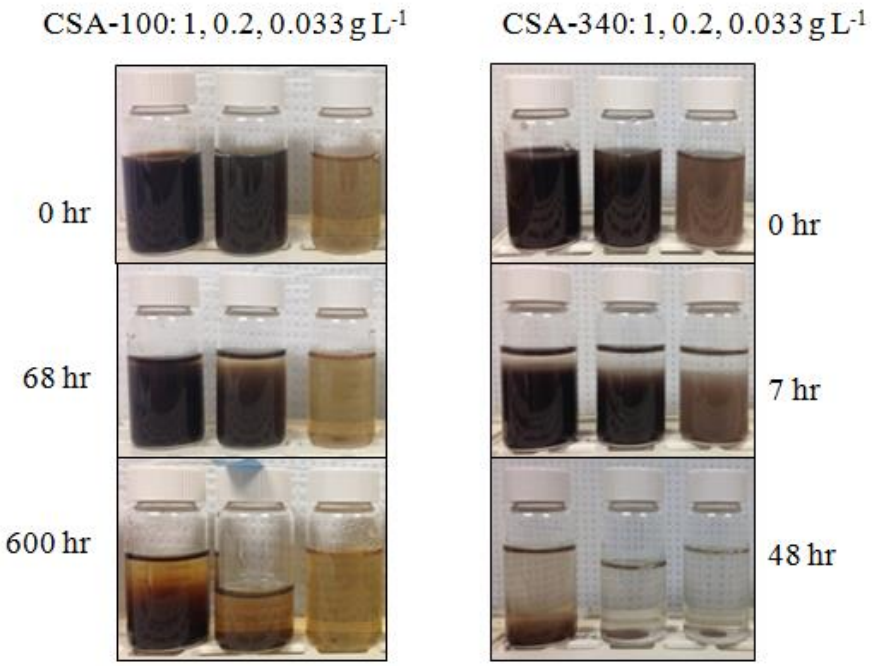

Figure A.5. Episodic suspension test (E-ST) for CSA-100 (left) and CSA-340 (right) in ultrapure water with varying NP concentration (left to right): 1, 0.2, and 0.033 or 0.05 g L^{-1}. The rows of photographs were taken at 0 hr, 68, and 600 hr for CSA-100 and 0, 7, and 48 hr for CSA-340 (note the magnitude difference. Note: the 0.2 g L^{-1} vials were sampled between the second and third set of pictures for DLS measurements.

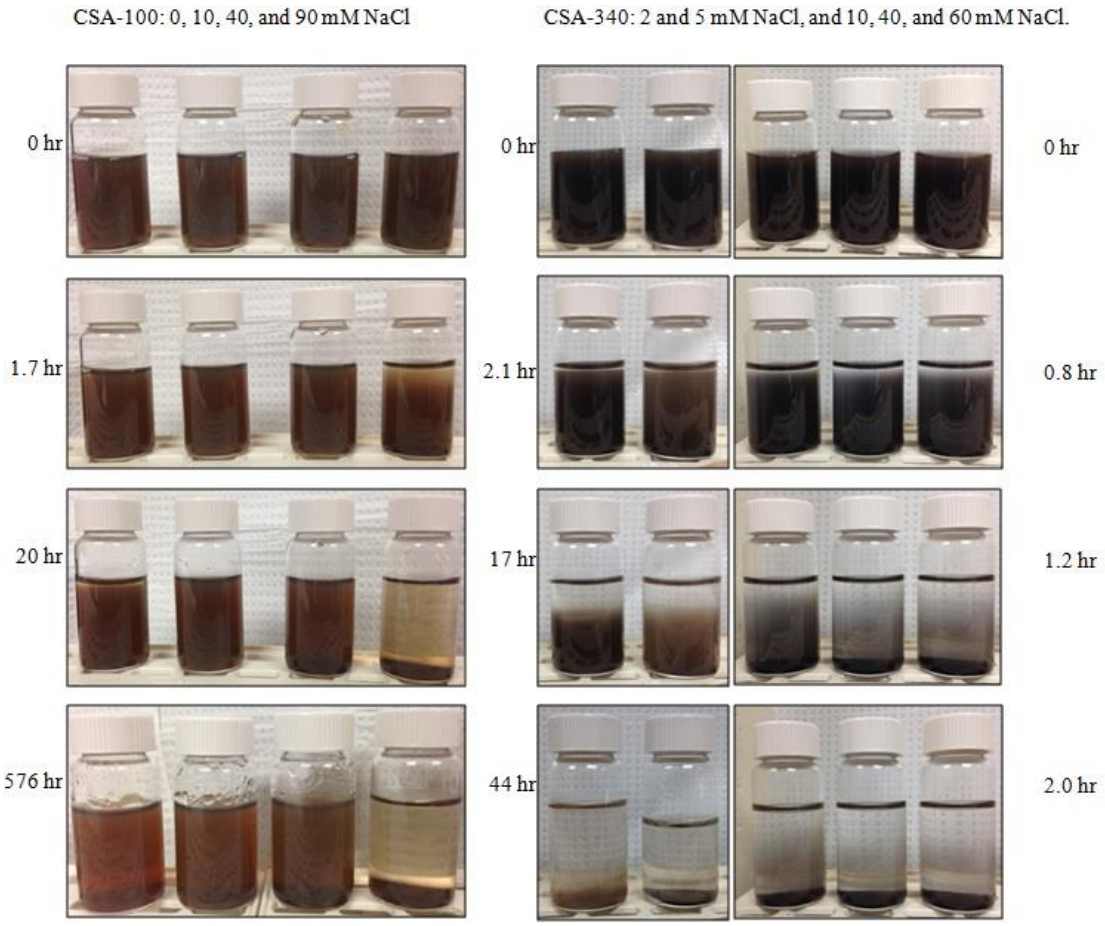

Figure A.6. E-ST of 0.02 g L^{-1} CSA-100 and CSA-340 with monovalent ions, NaCl. Left to right: 0.2 g/L CSA-100 in 0, 10, 40, 90 mM ionic strength NaCl, and CSA-340 in 2, 5, 10, 40, and 60 mM IS NaCl. See the corresponding times left of CSA-100 and 2 and 5 mM IS NaCl with CSA-340 and right of 10, 40, and60 mM IS NaCl in CSA-340 photographs. Note: CSA-100 in 90 mM IS NaCl was sampled between 17 and 44 hours.

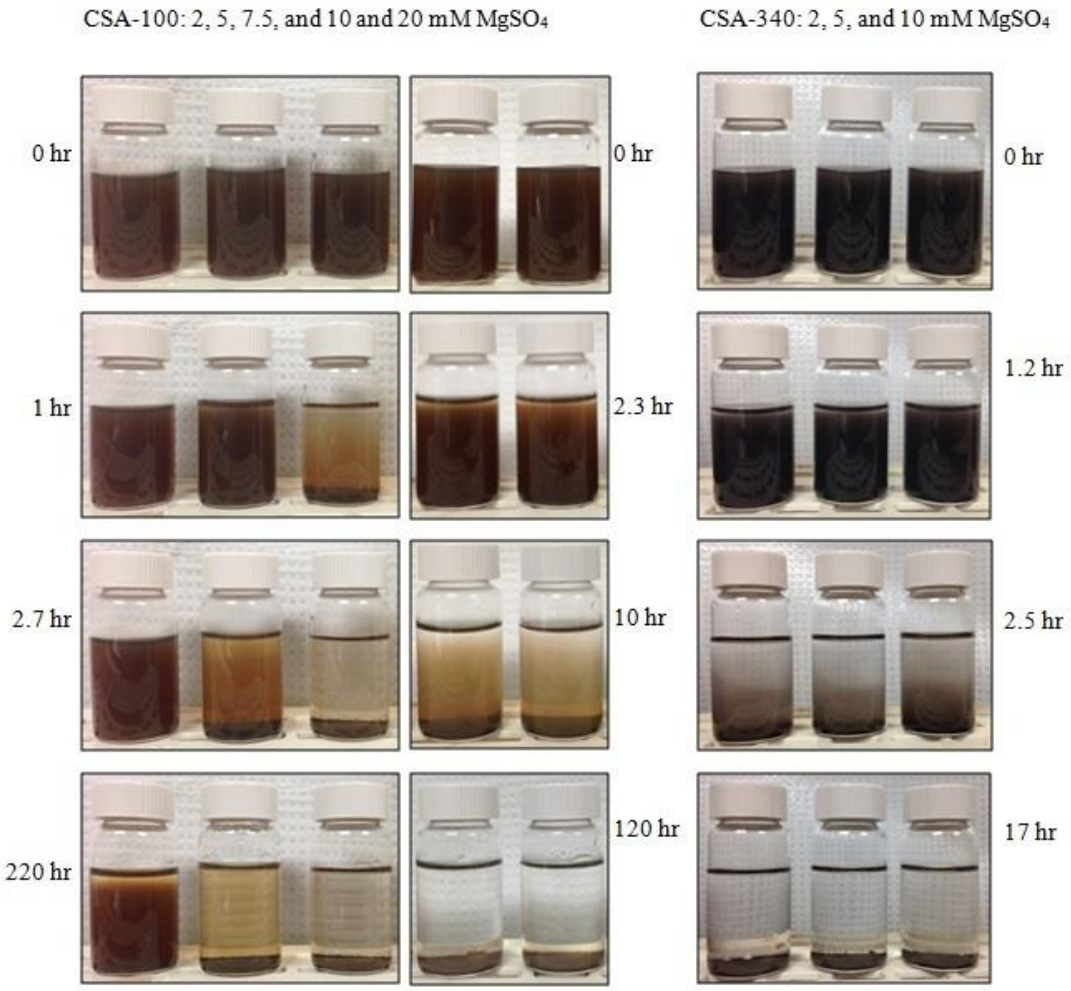

Figure A.7. E-ST in $MgSO_4$ divalent environments with 0.02 g L^{-1} CSA-100 and CSA-340. Photographs (left to right) are CSA-100 in 2, 5, 7.5, and 10 and 20 mM ionic strength (IS) $MgSO_4$, followed by CSA-340 in 2, 5, and 10 mM IS $MgSO_4$. PHREEQCi simulated $MgSO_4$ ionic strengths are 1.9, 4.4, 6.3, 8.1, and 15.0 for 2, 5, 7.5, 10 and 20 mM calculated IS. See the corresponding times left of CSA-100 first set and right of CSA-100 second set and CSA-340.

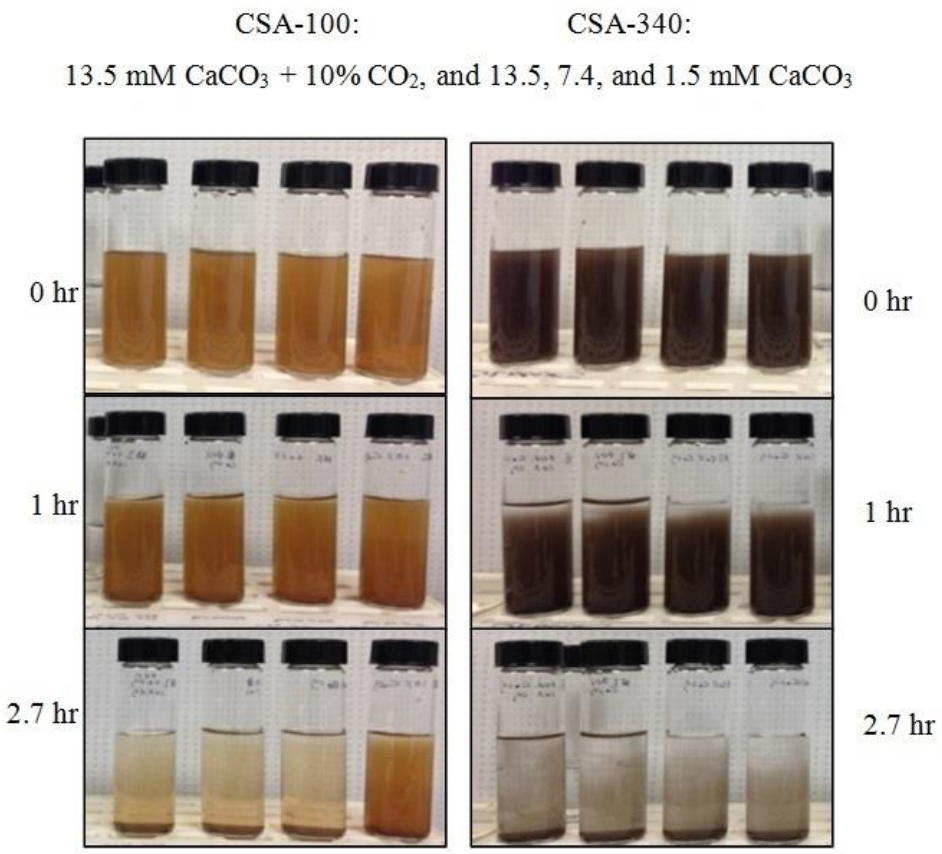

Figure A.8. E-ST Photographs for 0.02 g L^{-1} CSA-100 and CSA-340 in $CaCO_3$ environments. The rows of photographs correspond to 0, 1, and 2.7 hours. The aqueous solutions (left to right) contain 13.5 mM IS $CaCO_3$ saturated with 10 % CO_2, and 13.5, 7.4, and 1.5 mM IS $CaCO_3$. PHREEQCi simulated $CaCO_3$ ionic strengths are 1.3, 5.1, and 11.7 for 1.5, 7.4, 13.5 mM calculated IS. Note: the only NP suspended at 2.7 hr are CSA-100 in 1.3 mM IS $CaCO_3$. Note: septum vials are used to seal the gaseous environment in the vials.

Appendix E

Spectrophotometer Calibration Curves

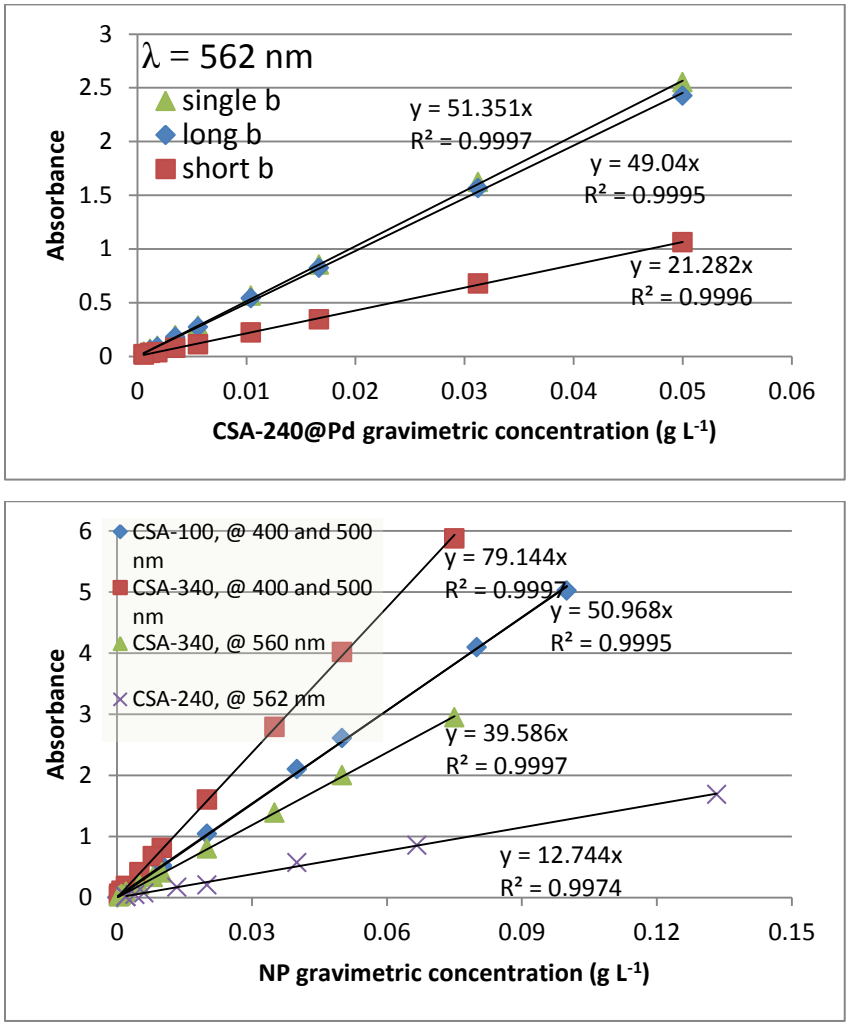

Figure A.9. Calibration curves from spectrophotometers HACH 2400 (min. 0.5 mL sample required, column test samples) and HACH 2800 (10 mL samples, C-ST samples). CSA-100 and CSA-340 curves were completed at wavelengths (λ) 400 and 500 nm, CSA-340 single wavelength was completed at 560 nm, and CSA-240 at 562 nm in a cuvette with a short path length with HACH 2400. The λ used in the 2400 and 2800 are in the same range and produce similar absorbances. The linear calibration curve is only valid under 0.15 g L^{-1} CSA.

Appendix F

ICP-OES Iron *versus* Nanoparticle Gravimetric Concentration Calibration Curve

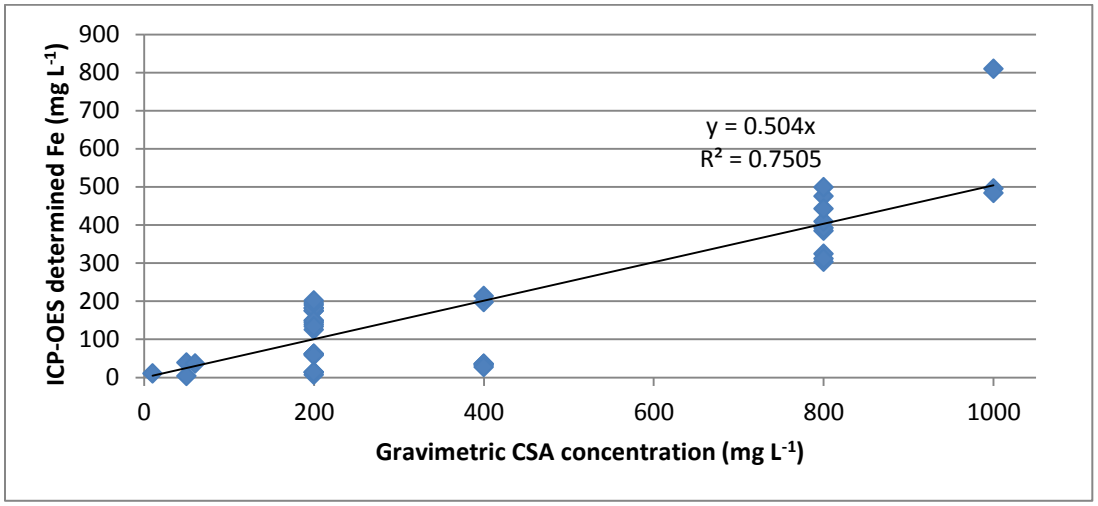

Figure A.10. Calibration Curve for Fe determined by ICP-OES analysis *versus* CSA concentration.

Appendix G

Durability of Pd-coating on Pd-coated CSA Test Results and Discussion

Chapter 2 describes the methods and qualitative results of a test designed to assess the stability of Pd on the surface of CSA. CSA-240' and CSA-240@Pd' were used. Results and a discussion are presented here. After adjusting for experimentally introduced changes, in 11 sampling events covering 120 days, Na concentrations were 96-120 % and Ca concentrations decreased by 20-30 % (Table A.4). However, Ca was undetected in settled samples at later times, suggesting the loss of Ca mass and the potential partition of Ca to the NP due to complexes.

Table A.4. Salt concentrations from blanks and as indicators of dilution or evaporation.

	0 day	**2 day**	**10 day**	**18 day**	**18 day**	**31 day**	**81 day**	**81 day**	**120 day**	**120 day**
NP state	Suspended	Settled	Sett.	Sett.	Susp.	Sett.	Sett.	Susp.	Sett.	Susp.
Salt Blank (Ca)	8.47	8.49	9.58	9.51	0.00	9.50	0	0	0	0
CaCO3 1	8.67	6.21	6.10	5.56	12.52	5.15	0	7.02	0	6.87
CaCO3 2	8.78	7.14	7.15	7.18	11.29	7.31	0	0	0	6.20
CaCO3 3	12.96	7.10	7.00	6.84	11.68	6.35	0	0	0	0
Salt Blank (Na)	212.0	218.6	237.6	236.8	0.0	237.8	335.8	0.0	281.3	0.0
10 mM IS NaCl 1	223.1	233.0	226.4	235.2	232.8	231.6	269.0	269.3	226.8	232.3
10 mM IS NaCl 2	225.6	217.1	228.8	227.2	229.6	229.5	252.5	255.3	228.5	229.7

As indicated in Chapter 2, no Pd was detected in the settled samples at 18, 81 and 120 days in 10 mM IS NaCl, $CaCO_3$ solutions, and under magnetic fields (Table A.5). The detection limit corresponds to 10-20 % of the total Pd in each sample. Undetected Pd indicates that maximum 20 % of the Pd could have come off the NP. From 0 to 120 days, a 3 % decrease of the Pd:Fe ratio occurred in the averages with standard deviations < 5 % of the averages (Figure A.11). This decreased Pd relative to Fe indicates that < 5 % of the Pd may have been sampled in the settled samples, much less than the maximum solely based on detection limit.

Table A.5. Pd concentrations (adjusted to initial conditions) of settled sampling events. Zeroes are values below detection limit (1.9 ug L^{-1}).

Sample	**1 day**	**2 day**	**5.5 day**	**10 day**	**18 day**	**31 day**	**81 day**	**120 day**
Ultrapure water	0	0	0	0	0	0	0	0
Pd Ultrapure water	0.61	0.43	0	0	0	0	0	0
Pd Ultrapure water, magnet	0.15	0.093	0	0	0	0	0	0
Pd Ultrapure water, magnet dup.	0.23	0.028	0	0	0	0	0	0
Pd, 10 mM IS NaCl	0.11	0.20	0	0	0	1.68	0	0
Pd, 10 mM IS NaCl dup.	0.13	0.22	0	0	0	0.89	0	0
Pd $CaCO_3$	0	0.11	0	0	0	0	0	0
Pd $CaCO_3$ dup.	0.078	0	0	0	0	0	0	0
Pd $CaCO_3$ trip.	0	0.06	0	0	0	0	0	0

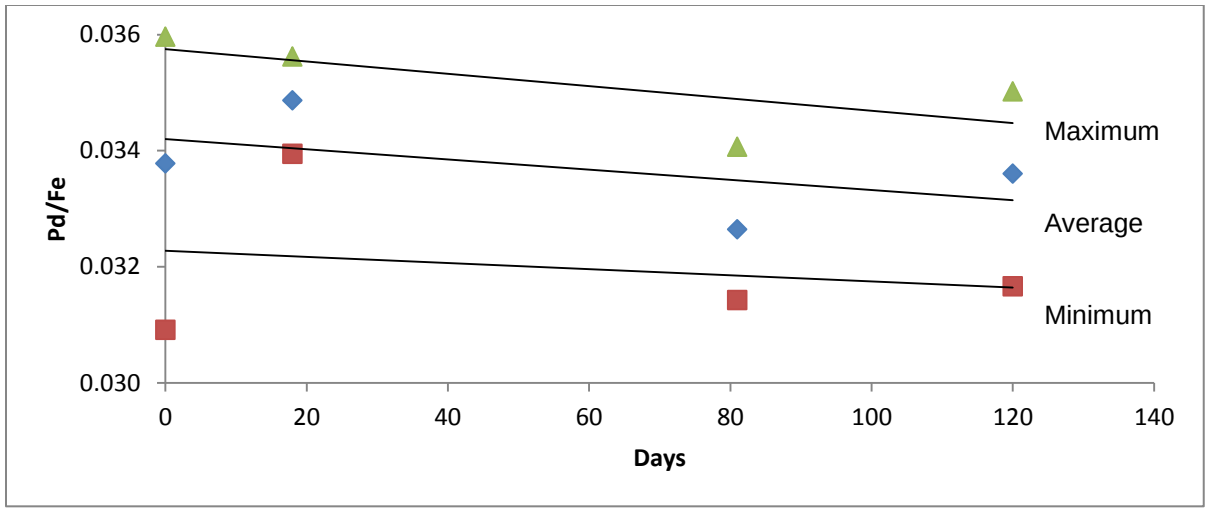

Figure A.11. Average Pd to Fe ratio of sampling events of the suspension at 0, 18, 81, and 120 days. Pd/Fe was averaged for all sampling events in NaCl, $CaCO_3$, or under the influence of a magnet.

Appendix H

Photographic Recordings of Column Tests

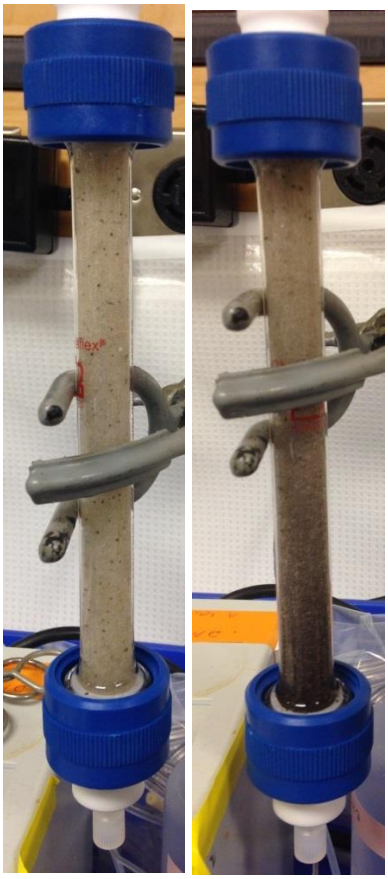

Figure A.12. Before and after (0 and 20 pore volumes) photographs from CSA-340 in 5.1 mM IS $CaCO_3$ column test showing the retention of 5 PV of nanoparticle input.

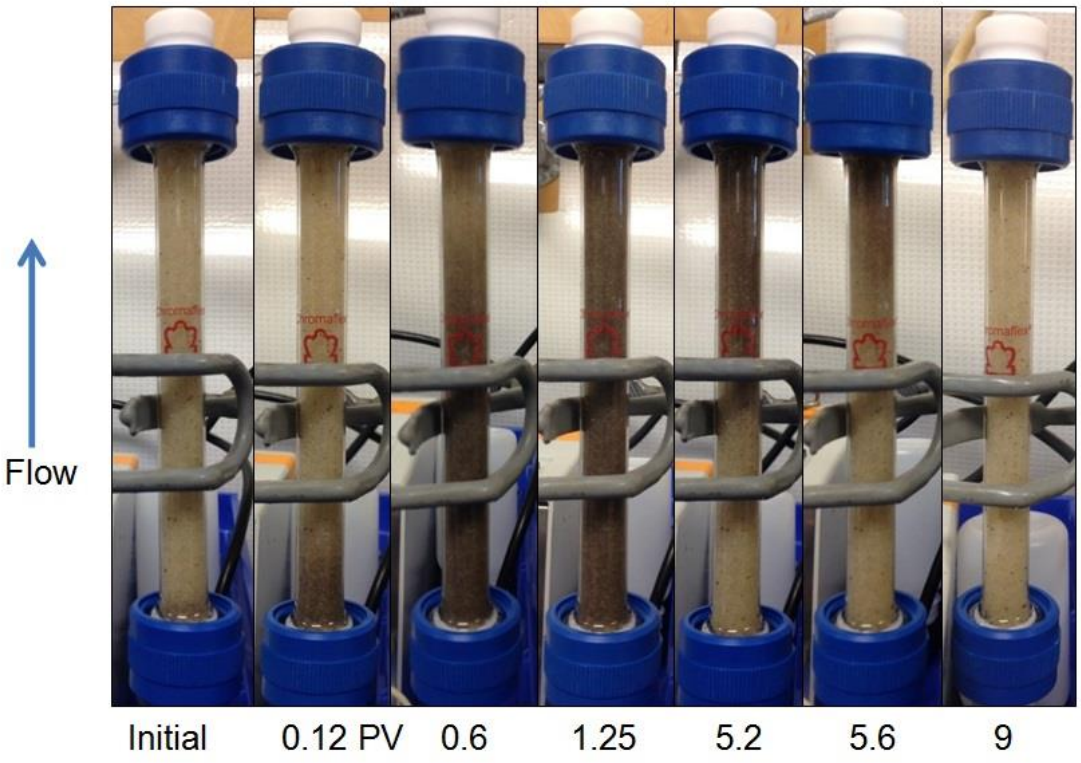

Figure A.13. Sequential photographs of the CSA-340 in ultrapure water column test. NP input occurred from 0-5 PV and was followed by ultrapure water only from 5-10 PV.

Appendix I
Column Profile Sampling

Although it is visually obvious where the NP were retained within a column following low transport (Figure A.12), quantitative profiles of NP retention were also obtained. These profiles were obtained by sampling column material following NP breakthrough tests and the digestion of the Fe-based NP.

Once the column material was sampled, each sample had 0.5 mL HCl added and was then agitated overnight on an orbital shaker. Samples were then diluted with 10 mL Milli-Q water and rotated on an orbital for 2 additional hours. Samples were filtered and analyzed using ICP-OES. The remaining sand was oven dried (110 °C overnight) and weighed. Blanks from clean Ottawa sand and standards from known concentrations of NP suspensions were prepared similarly to the column samples (Table A.6).

The column profile samples were blank-corrected and adjusted for dilutions due to the digestion method. The profiles compared the Fe (indicative of NP) concentration relative to the input Fe concentration determined from the standards (Figure A.14). Most retention was early in the column and decreased along the column. Accumulation of NP was present at the top of the column, which showed that some NP made it to the top of the column and probably subsequently out of the column.

Table A.6. Column profile blanks and standards data.

Sample Name		Fe (init.) mg L^{-1}	Fe blk. Corr. mg L^{-1}
AA	O.S. Blank	99.4	-
BB	O.S. Blank	136.8	-
CC	O.S. Blank	134.6	-
DD	O.S. Blank	211.2	-
EE	O.S. Blank	122.4	-
FF	O.S. Blank	235.9	-
	Average	156.7	-
	Standard Deviation	54.0	-
OS K	CSA digestion Std.	493.5	336.82
OS L	CSA digestion Std.	907.1	750.42
OS M	CSA digestion Std.	308.7	151.97
OS N	CSA digestion Std.	600.2	443.46
	Average	577.4	420.67
	Standard Deviation	250.7	250.66

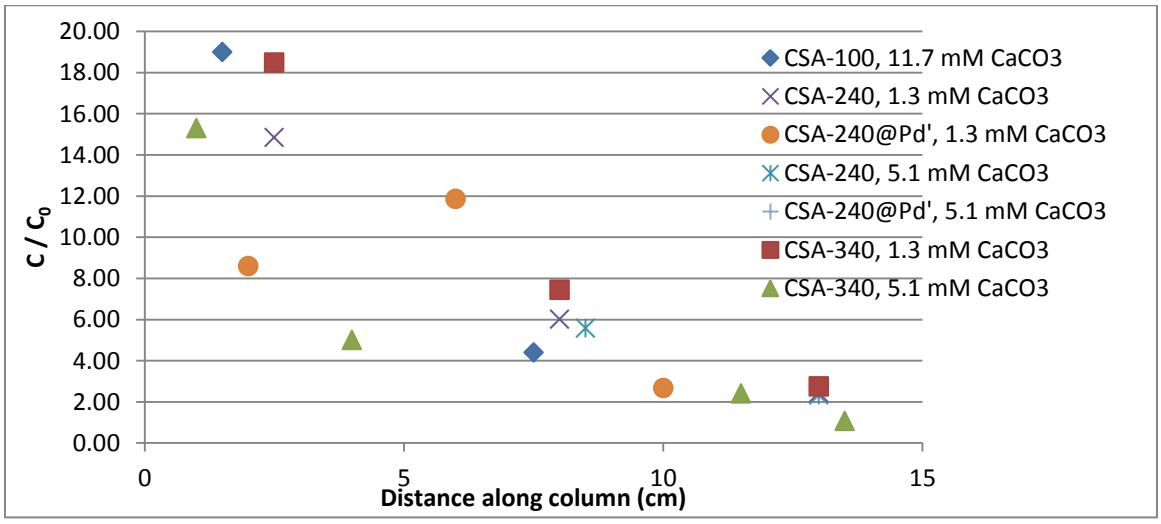

Figure A.14. Column profiles of Fe relative to Fe in input suspensions (C/C_0). 0 cm is the inlet of the column.